University of New Hampshire
University of New Hampshire Scholars' Repository

Doctoral Dissertations | Student Scholarship

Spring 1992

Solar flares: The onset of magnetic reconnection and the structure of radiative slow-mode shocks

Peng Xu
University of New Hampshire, Durham

Follow this and additional works at: https://scholars.unh.edu/dissertation

Recommended Citation
Xu, Peng, "Solar flares: The onset of magnetic reconnection and the structure of radiative slow-mode shocks" (1992). *Doctoral Dissertations*. 1693.
https://scholars.unh.edu/dissertation/1693

This Dissertation is brought to you for free and open access by the Student Scholarship at University of New Hampshire Scholars' Repository. It has been accepted for inclusion in Doctoral Dissertations by an authorized administrator of University of New Hampshire Scholars' Repository. For more information, please contact nicole.hentz@unh.edu.

INFORMATION TO USERS

This manuscript has been reproduced from the microfilm master. UMI films the text directly from the original or copy submitted. Thus, some thesis and dissertation copies are in typewriter face, while others may be from any type of computer printer.

The quality of this reproduction is dependent upon the quality of the copy submitted. Broken or indistinct print, colored or poor quality illustrations and photographs, print bleedthrough, substandard margins, and improper alignment can adversely affect reproduction.

In the unlikely event that the author did not send UMI a complete manuscript and there are missing pages, these will be noted. Also, if unauthorized copyright material had to be removed, a note will indicate the deletion.

Oversize materials (e.g., maps, drawings, charts) are reproduced by sectioning the original, beginning at the upper left-hand corner and continuing from left to right in equal sections with small overlaps. Each original is also photographed in one exposure and is included in reduced form at the back of the book.

Photographs included in the original manuscript have been reproduced xerographically in this copy. Higher quality 6" x 9" black and white photographic prints are available for any photographs or illustrations appearing in this copy for an additional charge. Contact UMI directly to order.

University Microfilms International
A Bell & Howell Information Company
300 North Zeeb Road, Ann Arbor, MI 48106-1346 USA
313/761-4700 800/521-0600

Order Number 9225268

Solar flares: The onset of magnetic reconnection and the structure of radiative slow-mode shocks

Xu, Peng, Ph.D.

University of New Hampshire, 1992

U·M·I
300 N. Zeeb Rd.
Ann Arbor, MI 48106

SOLAR FLARES: THE ONSET OF MAGNETIC RECONNECTION AND THE STRUCTURE OF RADIATIVE SLOW-MODE SHOCKS

BY

PENG XU

B. S., China University of Science and Technology, 1982

M. S., China University of Science and Technology, 1984

DISSERTATION

Submitted to the University of New Hampshire

in Partial Fulfillment of

the Requirement for the Degree of

Doctor of Philosophy

in

Physics

MAY, 1992

This dissertation has been examined and approved.

Dissertation director, Terry. G. Forbes
Research Professor of Physics

Joseph V. Hollweg
Director, Solar-Terrestrial Theory Group
Professor of Physics

Harvey Shepard
Professor of Physics

Richard L. Kaufmann
Professor of Physics

Dawn C. Meredith
Assistant Professor of Phisics

April 23, 1992
Date

To my parents and my wife

ACKNOWLEDGMENTS

The work for this dissertation has been supported by the NSF Grant ATM-8916303 and NSF Grant ATM-8711089. I am grateful to many colleagues and friends who have assisted me in various ways during the years of my graduate studies. I thank Professors Joe Hollweg, Martin Lee, Phil Isenberg, Richard Kaufmann, Harvey Shepard, and Dawn Meredith for many discussions and suggestions which are very helpful to my studies. I am grateful to Kathy Theall, who has given me reliable assistance in many instances. I thank Dot Kittredge for handling much of the paper work associated with my studies. I am very grateful to my wife, Yumei Yin, who has supported me throughout these years in many ways. Most of my gratitude, however, is reserved for my research advisor, Professor Terry Forbes. He has given me not only the guidance and suggestions to this dissertation, but also the ways and ideas to do physical research. His encouragement and patience have helped me overcome many difficulties in physics, English language, and computer programming.

Table of Contents

List of Tables

List of Figures

ABSTRACT

SOLAR FLARES: THE ONSET OF MAGNETIC RECONNECTION AND THE STRUCTURE OF RADIATIVE SLOW-MODE SHOCKS

by

Peng Xu
University of New Hampshire, May, 1992

This is a theoretical study of magnetohydrodynamic (MHD) processes associated with magnetic reconnection in large solar flares and other related eruptive phenomena. Magnetic reconnection is a basic process by which magnetic energy is converted into heat and kinetic energy, and it is thought to provide the necessary energy source for solar flares. Both analytical and numerical methods are used in the thesis to model two principal processes associated with reconnection in flares, namely: (1) the effect of magnetic reconnection on the evolution and loss of magnetic equilibrium before and during the flare; and (2) the structure of the radiative slow-mode shocks that are theoretically predicted to be produced by magnetic reconnection during flares.

The first process, which is the subject of Part I of the thesis, determines the effect of magnetic reconnection in the corona upon the loss of equilibrium triggered by the slow evolution of the field lines mapping to the region in the photosphere where the flare occurs. The quasi-static MHD equations are solved for a magnetic field configuration which satisfies line-tied boundary conditions during the eruption of the flare. The line-tied boundary conditions mean that the photospheric foot points of field lines cannot move during the course of the flare. Such boundary conditions occur because the inertial mass of the photosphere plasma is much greater than that of the corona. The effect of magnetic reconnection upon the equilibrium of the field is investigated by assuming three distinct characteristic time scales for three different physical

processes, namely the convective time scale τ_p (days) for motion in the photosphere, the reconnection time scale τ_r (hours) for reconnection in the corona, and the Alfvén time scale τ_A (minutes) for wave propagation in the corona. Magnetic energy can be gradually stored in the corona in a time period of τ_p as the system evolves through a series of equilibria until it reaches a point where no nearby equilibria are available. In the vicinity of this point a small perturbation is sufficient to disrupt the equilibrium of the system.

The second process, which is discussed in Part II of the thesis, is the magnetic energy conversion occurring in slow-mode MHD shocks in a plasma where both radiation and thermal conduction are important. In the MHD theory of reconnection, standing slow shocks occur in the vicinity of a magnetic x-line, and it is these shocks which actually convert magnetic energy into heat and kinetic energy. In a radiative and conducting plasma a slow shock has a complex structure because it dissociates into an extended foreshock, an isothermal subshock, and a downstream radiative cooling region. The analysis here considers the slow shock in the limit that it becomes what is known as a switch-off shock. Two paired sets of such shocks are generated when magnetic reconnection occurs in a plasma where the magnetic pressure is very much stronger than the gas pressure. The research reported here shows that for typical flare conditions, about 2/3 of the magnetic energy conversion in the slow shocks occurs in the subshock while the remaining 1/3 occurs in the foreshock. It is also shown that no stable, steady-state solutions exist for radiative slow shocks in a coronal like environment unless the temperature in the radiative region downstream of the subshock falls below 10^5 K.

INTRODUCTION

During last 50 years it has become clear to solar scientists that solar phenomena, such as sunspots, solar flares, prominence disruptions and coronal mass ejections (CME's), are due to the interactions of the plasma which makes up the solar atmosphere with the magnetic field produced in the interior of the Sun. Among these phenomena, large solar flares are of peculiar importance because they can eject material into interplanetary space while releasing an enormous amount of energy—$\gtrsim 10^{32}$ ergs; greater than any other explosive phenomenon in the solar system. Furthermore, flare effects can have a significant impact on the terrestrial environment.

This thesis deals with large solar flares and related eruptive phenomena. Because the interactions of solar magnetic field with the plasma (i.e., solar atmosphere) are very complicated, we use the well known approximation of magnetohydrodynamics (MHD), which treats the plasma as a magnetized fluid. MHD provides an effective and powerful tool for understanding many plasma phenomena and it has been successfully used to explain and predict many phenomena in space physics and astrophysics. Although the MHD equations are approximate (see Krall and Trivelpiece, 1973), they still constitute a set of highly nonlinear equations which are very difficult to solve. Thus for this thesis, we have used both analytical and numerical methods to obtain rigorous solutions of these equations .

The thesis consists of two parts, corresponding to two aspects of the MHD model for large solar flares. The first part deals with the effect of magnetic reconnection on the evolution of magnetic field configurations, which can undergo sudden transition from stable to unstable equilibria. Magnetic reconnection is a basic MHD process by which the magnetic field is dissipated and magnetic energy is converted into heat and kinetic

energy. The second part focuses on the generation of the flare loops by magnetic reconnection. These loops, often referred to as 'post-flare loops' because they are seen after flare onset, are a consequence of heating by magnetic reconnection in the corona. In the MHD theory of reconnection, the heating is produced by slow-mode MHD shocks which have the special ability to convert magnetic energy into heat and kinetic energy no matter how small the electrical resistivity of the plasma is.

This thesis presents the first analysis of the effect of reconnection on a loss of magnetic equilibrium which occurs even when reconnection is absent, i.e., a loss of equilibrium due to an ideal-MHD process. The analysis considers a loss of equilibrium with three distinct characteristic time scales for the different physical processes in the flare eruption. Unlike previous models of eruptive flares which assumed either that reconnection occurs freely in the corona or that no reconnection occurs in the corona, we consider the more realistic intermediate case where reconnection is possible but constrained.

The study of the effect of radiation on the slow-mode MHD shocks in flare loops is also new. Previous studies have considered radiative gasdynamic shocks, radiative fast-mode MHD shocks, and slow-mode MHD shocks with no radiation. But little analytical work has been done so far on radiative slow-mode shocks. This is perhaps surprising because such shocks are almost certain to arise in any process involving magnetic reconnection in the corona.

Before proceeding further into details, a brief overview of the Sun will be given in this *Introduction*, followed by an outline of the general description and current understanding of solar flares and the related eruptive phenomena. Some general studies of the Sun and its physics are found in Priest (1982a), Zirin (1988), Stix (1989) and Foukal (1990). For more specific work on solar flare and related energetic

phenomena, see Sturrock (1980), Priest (1981), Tandberg-Hanssen & Emslie (1988) and Kundu, Woodgate & Schmahl (1989).

All quantities in this thesis are in general measured in rationalized mks units. However, some other commonly used units such as 'erg' (energy) and 'G' (magnetic field strength) may also appear in the text.

The Sun and Its Interior

The radiation output of the Sun is 3.86×10^{26} W, widely distributed in a range from radio waves to X-rays. The pressure, density and temperature inside the Sun are so high that it is in general impossible to observe photons originating below the surface which is called the photosphere. Therefore, until the recent development of solar seismology and solar neutrino telescope, the understanding of the interior structure of the Sun could be deduced only from observations of the photosphere and the overlying atmosphere.

All solar phenomena observed may in general be divided into two groups: *quiet* and *active*. The quiet Sun is viewed as a static spherically symmetric ball of plasma whose magnetic field is negligible. By contrast, the active Sun consists of transient phenomena, such as sunspots, prominences and flares, which are superimposed on the quiet atmosphere, and most of which owe their existence to the magnetic field (e.g., Priest, 1982a).

A schematic diagram of solar structure is displayed in Figure 1. In general, the interior of the Sun can be divided into three regions: the *core*, *radiative zone* and *convection zone*. As a consequence of the great gravitational attraction of the Sun's large mass, the extremely high temperature ($\sim 1.6 \times 10^7$ K) and density ($\sim 1.6 \times 10^5$ kgm^{-3})

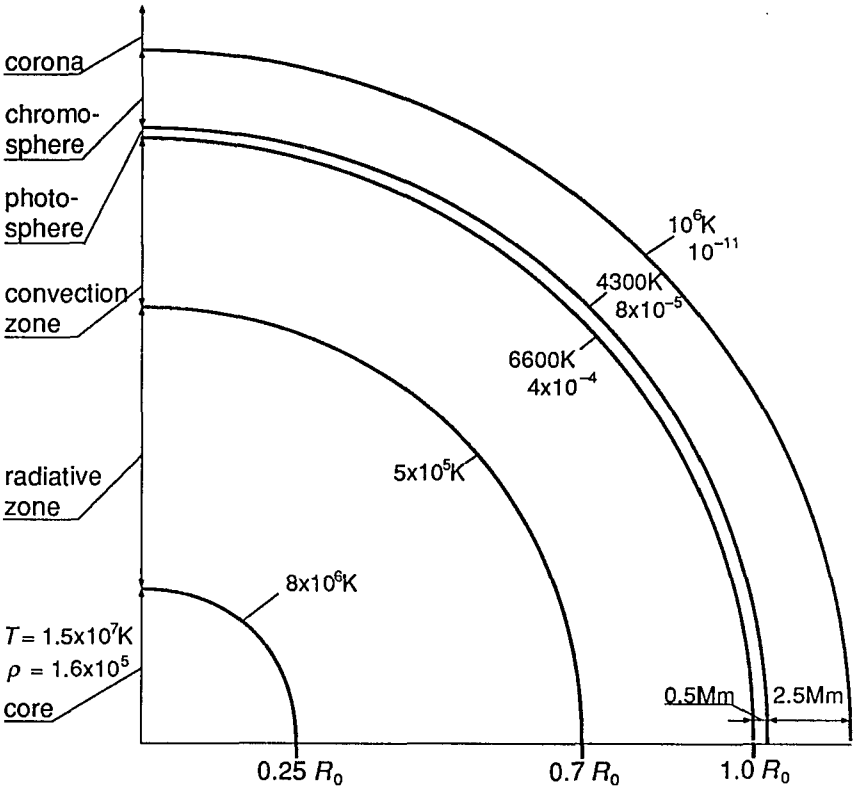

Fig. 1. A schematic diagram of solar structure, showing a quarter of equatorial cross-section. The size of the various regions and their temperatures are indicated. The thicknesses of the atmospheres (photosphere and chromosphere) are not proportional to scale.

are reached in the core (from the center to about 0.25 R_0), enough for H to be fused to form He through thermonuclear reactions. The energy generated by thermonuclear fusion in the core is the source of radiant energy of the Sun. The core contains about half the mass of the Sun and generates 99% of the energy, in the form of photon and energetic particles. The region immediately outside of the core is the radiative zone, where the energy produced in the core is slowly transferred outward by radiative diffusion—the photons are randomly absorbed and re-emitted many times by surrounding material. The solar interior is so opaque that it takes about 10^7 years for photons to reach the surface, instead of about 2 seconds, the time needed for light travels from the center to the surface. From the radiative zone outward is the convection zone (from about 0.7 R_0 to 1.0 R_0). Because the temperature and density decrease with distance from the solar center very rapidly, their gradients are too great in the convection zone for the material to remain in static equilibrium, and convective instability takes place. In the convection zone the energy is transported primarily via convection, i.e., mass motions which are seen evidently through the granulation and supergranulation on the surface. It is also generally believed that the Sun's magnetic field is generated in the convection zone by the magnetic dynamo mechanism (see, e.g., Roberts, 1967; Priest, 1982a)

Solar Atmosphere: the Quiet Sun

The visible solar atmosphere is divided into three principal layers according to different physical properties, namely, the *photosphere*, *chromosphere* and *corona*. None of these layers is sharply bounded; instead, they merge into one another. Figure 2 shows the variation of the temperature with height in the solar atmosphere. Here the height refers to the distance above the surface.

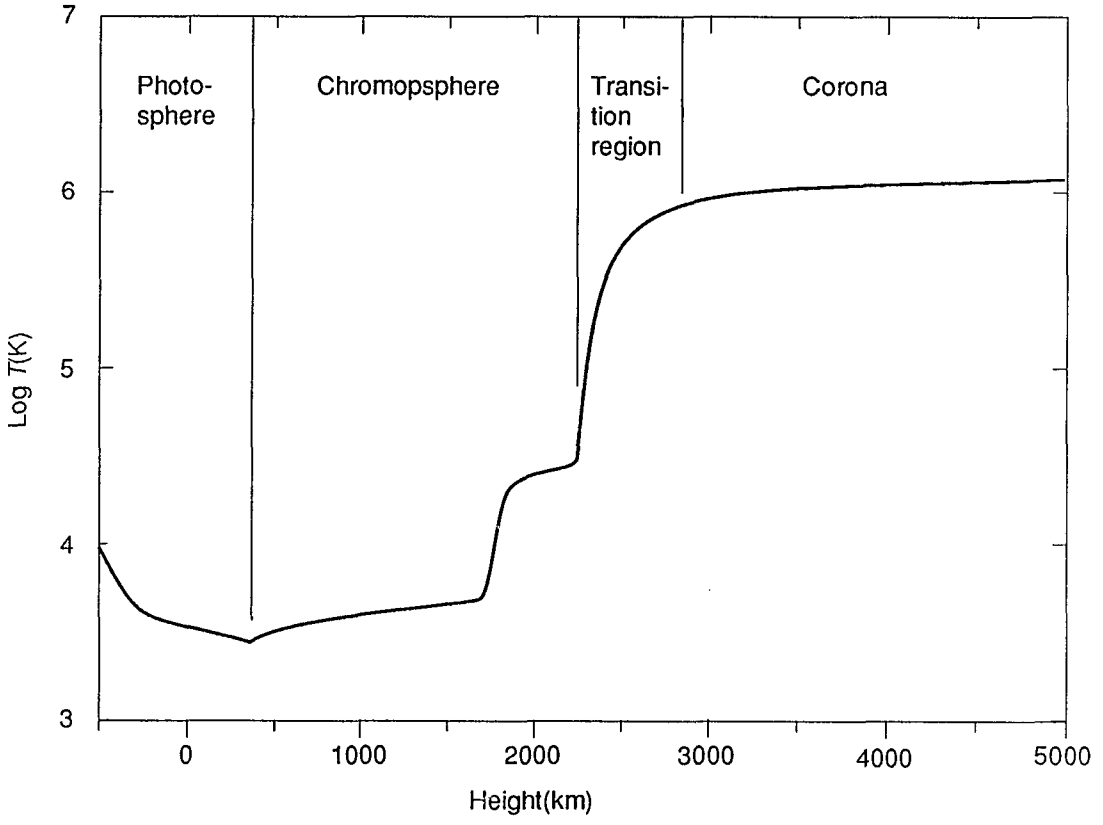

Fig. 2. The variation of the temperature with height in the solar atmosphere, based on Athay's model (Athay, 1976)

The photosphere ('light sphere') is the visible surface of the Sun. It is so named because most of the solar radiation is emitted from this layer of solar atmosphere. As the temperature and density continue to drop through the convection zone, it finally reaches a point where the photons from the interior are free from the absorption or scattering by surrounding media. Above it, the gases are almost entirely transparent, and below it they are opaque. The photosphere is a very thin layer (about 500 km thick) in which the temperature continues to decline from about 6600 K at the base to a minimum value of some 4300K at the top.

The photosphere is easier to study than the unseen regions below and transparent layers above. Radiation of all wavelengths from the photosphere enables us to obtain detailed observations of the Sun and its surface structure, which is crucial for the understanding of the solar interior and physics inside the Sun. The photosphere observation is also very important for studying and understanding the phenomena occurring at the upper solar atmosphere because these phenomena, such as solar flares and other eruptive phenomena are actually rooted in the photosphere. The most obvious feature of the photosphere is *solar granulation* (see, e.g., Stix, 1989, Fig. 3.4; Zirin, 1988, Fig. 6.8), a universal pattern composed of bright granules of complex polygonal shape, separated by narrow dark lanes. Other granule-like features of larger scales, such as the *mesogranulation* and *supergranulation* have also been observed (see, e.g., Stix, 1989, Fig. 6.15). These features are very important because mass motions of different scales in the convection zone just below the photosphere are manifested in the granulations. The bright granules are upwards-moving, hot parcels of plasma, while the dark intergranular lanes represent downwards-moving, cooler material. Some observed properties of these features are given in Table 5-1 of Foukal (1989).

The layer just above the photosphere is called the chromosphere ('color sphere') because of its reddish color, which can be seen around the limb (the Sun's edge) when the

photosphere is hidden during a total eclipse. This color is primarily due to the Hα line emission (the n=3 to n=2 transition in atomic hydrogen) occurring at the chromosphere temperature. As shown in Figure 2, the temperature rises monotonically through the chromosphere, from the minimum to roughly 10^4 K at some 2000 km height, and then jumps rapidly to several times 10^5 K in the transition region between the chromosphere and corona.

The chromosphere is highly non-uniform, as indicated in Figure 9-5 of Foukal (1990). The obvious features seen at the limb (e.g., Zirin, 1988, Fig . 7.5) are *spicules*. Similar features known as *mottles* (bright and dark) and *fibrils* are visible on the disk. Also visible is the *chromospheric network* which coincides the supergranulation boundaries. The magnetic field above supergranule boundaries continues to spread out with height and this causes the network to thicken with increasing temperature till it ceases to exist at coronal height.

The corona ('crown') is the outermost major layer of the solar atmosphere. It is a faint halo of very low density and high temperature, and only visible during total eclipses. However, the using of coronographs, which create artificial eclipse, makes it possible to observe the corona while no eclipse occurs. In addition to the white light seen, the corona may also be viewed directly by observing its emissions which are prominently in X-rays and UV due to its high temperature. However, this is usually done on board satellites and rockets to avoid the strong absorption of the Earth's atmosphere in these wavelengths. A large body of X-ray and UV coronal data has been collected by the Skylab and other spacecrafts since early 1970's. These observations provided insight for understanding the structure and dynamics of the corona.

The average electron density in the low corona is about several times 10^{14} m^{-3}, and this is usually enhanced by factors of 5 ~ 20 in many of the structures. The density

rapidly falls off with distance from the solar surface and eventually becomes less than 10^{10} m^{-3} at $10R_0$. By contrast, the temperature of the corona is very high (1 ~ 3 x 10^6 K) and it falls off slowly in the outer corona, which is expanding outwards as the solar wind, to about 10^5 K at 1 AU. The mechanism of the coronal heating has long been a major issue in solar physics. However, it is well recognized that the magnetic field is responsible for transporting mechanical energy from the photosphere and /or the convection zone to the corona and converting it into thermal energy.

The most prominent structures of the corona are the large *streamers* extending roughly radial, as seen in Figure 9-10 of Foukal (1990). Other important structures are bright *coronal loops* of dense plasma, and large dark regions known as coronal holes (e.g., Zirin, 1988, Fig. 8.3); where the plasma is flowing out to give the solar wind. Figure 8. 2 of Zirin (1988) shows clearly how the coronal structure is shaped by magnetic field, implying that the coronal loops represent regions where the magnetic fields are mainly closed whereas the coronal holes appear where the fields are predominantly open.

In open-field regions, the solar corona is not in hydrostatic equilibrium, but is continuously expanding outwards as the solar wind, and escapes along open field lines from coronal holes. The flow speed increases from very low value to super-Alfvénic (400 ~800 kms^{-1}). It takes about 5 days for the solar wind to reach the Earth's orbit. Beyond the Earth, the solar wind is believed to extend out to interstellar space at 50 or 100 AU. The solar wind is far from uniform, some typical values of its properties at 1AU are given in Table 1. 1 of Priest(1982a).

The Active Sun: Transient Features

The active Sun exhibits rich and varied dynamical structures superimposed on the quite atmosphere. For example, a composite photograph of the Sun (Priest, 1982a, Fig.

1. 19) shows many of the important features. They include *active regions* (*plages*), *sunspots*, *quite* (*active*) *prominences* (*filaments*) and *solar flares*. These features appear at different levels in the atmosphere, and represent different ways in which the solar plasma is responding to the underlying magnetic field movement and development.

The active regions are the extended areas where spots, faculae, plages, filaments, and sometimes flares, occur together. They are most prominent when seen in soft X-ray imagings of the Sun (e.g., Zirin, 1988, Fig. 8. 3). The active regions are developed from emerging flux regions where new magnetic flux emerges from below the photosphere, and flux prefers to appear in the equatorial belt within $\pm 30^{\circ}$ of the equator. New active regions have a tendency to develop near existing or remnant active regions. The mean field strength in active regions is enhanced to 100 G due to the flux concentrations. It in general takes 3 to 4 days for a well-developed active region (about 200,000 km across) to form: a sunspot group surrounded by photospheric faculae at lower level, and an X-ray enhancement at upper portion. The region continues to grow and reaches its maximum activity in 10 to 15 days, and then decays in a much slower manner. Most of the active regions are bipolar with the flux well-ordered into two islands of opposite polarity. Eventually, exhibited in the active regions are a rich variety of loop systems, including *arch-filament system*, *active-region prominence* (*sunspot-loop*), *cool prominence*, etc.; the later is often stretched out by differential rotation to become a huge quiescent prominence migrating towards the nearest pole. The dynamic nature of these loops and their motions is an active aspect of solar physics study.

Sometimes several active regions may appear simultaneously on the disk. These active regions, as indicated by Skylab data, are usually connected by arch or loop structures, which outline magnetic field configuration and provide channels for different types of disturbances to travel from one active-region to another.

Although most of transient solar phenomena occur in the active regions, some of them, such as quiescent prominence eruptions, may occur in regions far away from the active regions.

In contrast to the active regions, the sunspots are the most obvious features seen on white light photographs of the photosphere. These dark spots represent the most intense concentrations of magnetic flux in the active regions with central field of 2000 ~ 3000 G (may reach as much as 4000 G). As shown in Figure 1. 24 of Priest (1982a), a typical sunspot consists of a central dark area called the *umbra* (diameter: 10,000-20,000 km, about 0.4 times the total spot diameter) surrounded by a less dark but more structured region called the *penumbra*. Sunspots are developed from the *pores*, usually grown in the flux concentration areas—junctions of three supergranule cells. Pores are darker than the surrounding photosphere and have no penumbrae (field ~ 1500 G). In general the sunspots are growing in a period between 3 and 10 days, and most of them disappear within a few days of forming, except some large ones (usually leaders) which may last over a few months. Typically, the sunspots are formed in pairs of opposite polarity, with loops connected in between. However, spots of unipolar and other complex polarity are also present. The darkness of the sunspots is due to their coolness. For example, the typical effective temperature of a spot umbra is about 3700 K, some 2000 K cooler than that of the surrounding photosphere. The reason for the coolness seems to lie in the blocking of horizontal convection by intense vertical magnetic fields (Foukal, 1990).

The sunspot activity (the number of sunspots and sunspot groups visible on the disk) exhibits a periodical behavior which represents the solar cycle. It becomes the index of solar activity because it reflects the variation of solar magnetic field activity correlated with all important solar phenomena.

Prominences are observationally defined as any Hα emitting plasma which occurs in the corona. Prominences appear bright at the limb (in eclipse) but dark on the disk in Hα photographs (see, e.g., Priest, 1982a, Figs. 1. 31& 1. 33). They are often referred to as filaments when seen on the disk. The fact that prominences are seen in Hα indicates that they are composed of cool plasma (5,000-10,000 K) and are much cooler than the surrounding corona ($2x10^6$ K). Despite of several different ways of classification, they can be divided into two basic types, i.e., the *static prominences* and the *dynamic* (i.e. active) *prominences* . The former includes *quiescent* and *active-region prominences.*

Quiescent prominences are extremely stable and huge structures which typically occur in the weak magnetic field region outside the active regions. Quiescent prominences may continue to growing for many months up to 1,000,000 km in length, while migrating slowly at the same time towards the nearest pole. Comparing with their surrounding corona, the quiescents are much cooler (~ 7000 K) and denser (~ 10^{17} m^{-3}). The typical values for thickness, height, length and field strength are 5000 km, 50,000 km, 200,000 km and 5 ~ 10 G, respectively. On the other hand, active-region prominences always occur inside the active regions and are typically a factor of three to four smaller than the quiescent prominences, and they have stronger field (50 ~ 100 G) and lower height (at most 20,000km), with magnetic field aligned approximately.

By contrast, dynamic prominences are dynamic structures with violent motions, often associated with solar flares, and last for minutes or hours. They are located in active regions and have higher field strengths (about 100 G), higher density ($\geq 10^{17}$ m^{-3}) and much higher temperature ($> 10^5$ K). They have various types, such as *surges*, *sprays*, and *loop prominences*, all resulting from flares. In general dynamic prominences are much smaller than the quiescents.

Sometimes an active-region prominence or a quiescent prominence may become unstable and erupt; it ascends as an erupting prominence and eventually disappears; some of the material escapes from the Sun with solar wind while some descends back to the chromosphere. The active-region prominence eruptions are fast (10 ~ 30 min) and a large flare (often two-ribbon) occurs; while quiescent prominences erupt slowly (hours) and only a little brightening occurs. Often the prominences reform in the same place after eruptions.

Solar Flares

The solar flare is one of the most impressive solar phenomena, and large solar flares are the most powerful transient phenomena in the solar system. Most flares are associated with violent plasma motions —prominence eruptions and coronal mass ejections. The ejected plasma often carries a significant amount of energy and makes up an important part of the flare phenomenon. A rich variety of magnetic field activities combined with various dynamic structures and violent motions also make flares the most complex and exciting solar phenomena to observe and study.

Brief Description

Solar flares can be specifically defined as "intense, abrupt releases of energy which occur in areas where the magnetic field is changing because of flux emergence or sunspot motion deriving from flux emergence" (Zirin, 1988). A rapid brightening in Hα, which is most often observed, associated simultaneously with bursts in all different wavelengths across the electromagnetic spectrum, high-energy particle ejections and sometimes the coronal mass ejections gives a tremendous energy output, varying from 10^{22} J in a subflare to 3×10^{25} J (3×10^{32} erg) in the largest ones.

The optical flare observed in Hα has two basic stages: the *flash phase* in which the intensity and area of the emission rapidly increase, and the *main (gradual) phase* in which the intensity declines slowly. However, the observations in other wavelengths suggest that the flare is probably initiated and the energy released in a high-temperature regions above the cool Hα flare. This overlying region of coronal loops may be heated up to several times 10^7 K, and manifests itself by showing two more distinct phases in addition to the coincidence with the flash and gradual phases. As seen in Figure 3, a *preflare phase* due to an enhanced thermal emission from the coronal plasma appears in the soft X-ray emission (< 10 keV) several minutes before the flare onset, and an *impulsive phase* caused by highly accelerated elections is sometimes present at the start of the flare, as indicated in the microwave and hard X-ray emissions. The events with no impulsive phase are known as thermal flares which tend to occur in less complex regions and have a slower rise to flare maximum. There is a great variation in the duration and complexity of the various phases. In a large event the preflare phase lasts typically 10 minutes (but up to an hour), the impulsive phase a minute, the flash phase 5 minutes (but sometimes an hour), and the main phase about an hour (sometimes as much as a day).

The flares also manifest themselves with a rich variety of dynamic structures. The smallest ones may appear in Hα or X-rays as small as unresolvable bright points which simply brighten and fade, without moving of changing their shapes; whereas the largest ones always exhibit complex structure and movements of both the ribbons and flare loop systems.

The energy source of a solar flare is the energy associated with stressed magnetic field. The stress is built up when the magnetic field in photosphere is changing because of flux emergence, while the lines of force in corona can not adjust themselves promptly in response to these changes because of 'frozen in' effect. This occurs most frequently at

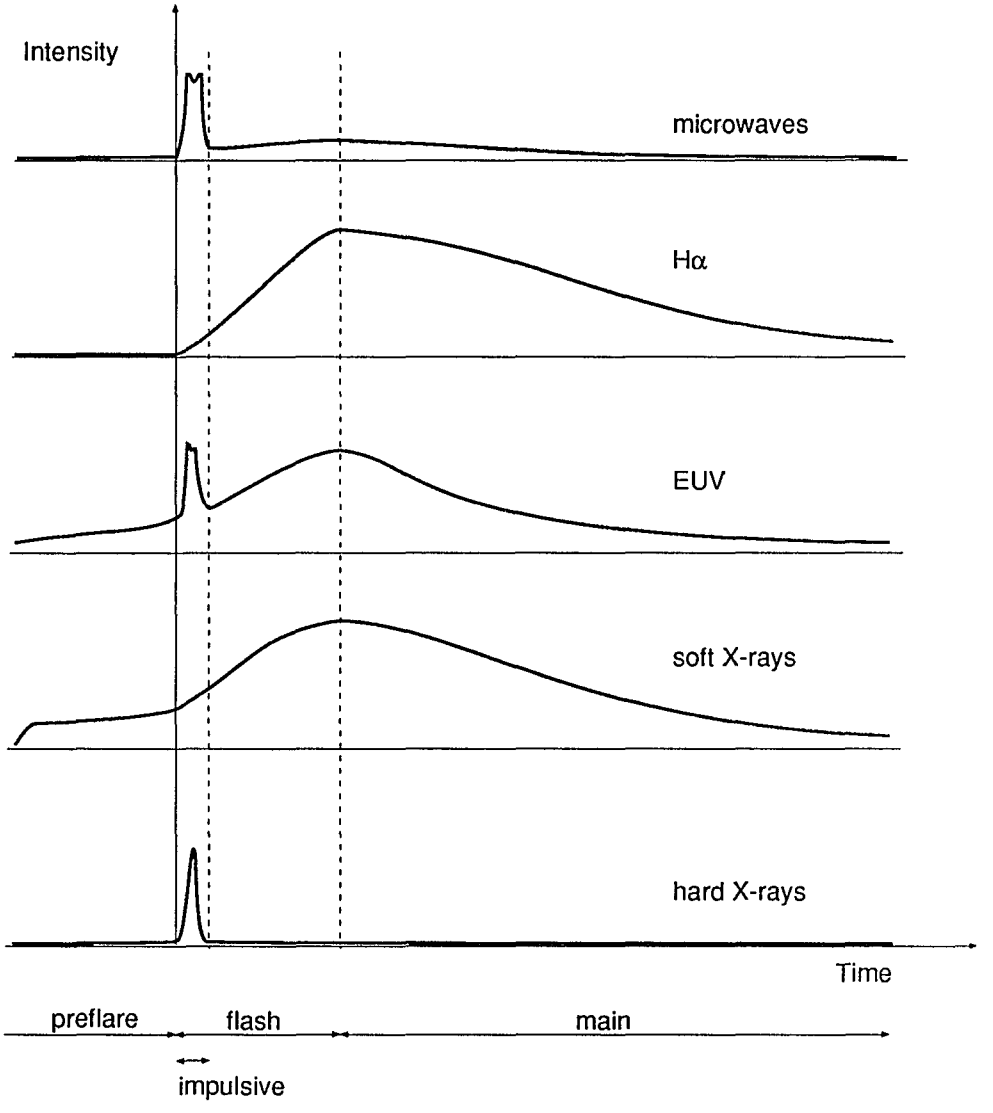

Fig. 3. A schematic profile of the flare intensity in several wavelengths (after Priest, 1981).

the *magnetic neutral lines* where a prominence is supported by horizontal sheared field lines. Therefore, when the stress build up (i.e., the stored energy) exceeds certain critical value, the configuration becomes unstable and erupts outwards, the associated energy release usually produces a flare. Sometimes the prominence eruption is so violent that the matter of overlying corona can be ejected to the outer corona or interplanetary space, and a coronal mass ejection is also observed.

Flare Classification and Two-ribbon Flares

The solar flares are so complex that they have been classified in many different ways according to certain different observables; and each classification is expected to provide with some specific physical insight into the flare phenomenon.

Soft X-ray flare classification is probably the simplest classification which is based on the global output of soft X-ray during a flare: a flare is classified according to the measured X-ray flux in the 1 - 8 Å ranger of the spectrum (see, e.g., Tandberg-Hanssen, 1988, Table 1. 1). Hard X-ray flares have been classified by Tanaka (1983) according to their sizes and altitudes of occurrence.

Since all flare classifications prior to the 1960's have relied on observations in the visible part of the spectrum, visual light classifications are also important. *Hα flare classification*, a dual form for importance classification (see, Tandberg-Hanssen, 1988, Table 1. 2), is based on the area covered by a flare on pictures of the disk, combined with an index letter which indicates whether the intensity of the flare area is faint (f), normal (n), or brilliant (b). In this classification, flares smaller than about 3×10^8 km^2 have generally been referred to as subflares. There are some other classifications based on the radio flux of the flares. For most flares, a good correlation exists between Soft X-ray classification and Hα classification. However, some flares rate as very important

in X-ray domain, while their visual output would classify them as minor events-and vice versa for other flares.

Despite of so many classifications, flares are roughly divided into two main groups, i.e., small, compact (or simple-loop) flares and large, two-ribbon flares. This division is mainly for practical purposes—it is not the distinction between compact, in the sense of small, versus two ribbons that is important from a physical point of view, but rather whether the flare is confined or not (Švestka, 1986). A compact flare may occur in a large-scale unipolar region or near a simple sunspot. Such a flare consists of a small loop (or collection of loops) in the lower corona, and the flare emission is largely confined to the plasma in the loop. Eventually the emission dies away, without moving or changing shape. By contrast, a two-ribbon flare is always associated with an eruptive prominence. The flare emission occurs in an arcade of the flare loops along the prominence with the loops gradually aligned more normal to the axis of the prominence during the evolution of the flare. During the flash phase two chromospheric ribbons of Hα emission form on either side of the prominence, and throughout the gradual phase the ribbons move apart, gradually slowing from 50 kms^{-1} to 1 kms^{-1} or so. As the ribbon move apart larger and higher loops continuing to bridge the distance between them.

The flare loops are the most spectacular and persistent features associated with large two-ribbon flares. During the main phase they are observed to rise upward slowly into the corona. The velocity of ascent decreases with height from about 50 kms^{-1} at the beginning to about 0.5 kms^{-1} when they finally reach their maximum heights. In fact, the system does not consist of single loops rising upwards, but rather of newly formed or activated stationary loops appearing at successively higher levels. The Hα ribbons are identified by observations as the footpoints of the flare loops. The heights of the loops depend strongly upon what type of emission is observed. The lowest loops

are seen in Hα and can rise to heights of some 60,000 km. However, the highest loops can be observed in soft X-rays at heights of over 100,000km (MacCombie and Rust, 1979). The flare loops may last for 10-20 hours or even longer. As soon as a loop is seen in Hα, material is observed to be flowing downward along the legs of the loop. It is estimated that during its lifetime the amount of material that drains down the legs of the flare loops exceeds the mass of the entire corona.

A two-ribbon flare usually takes place near an active-region prominence which is lying along the axis of an arcade of sheared magnetic loops. However, it may occasionally appear in a region completely devoid of sunspots when a quiescent prominence erupts, and it may only give rise to X-ray emission with no Hα brightening, due to the weak magnetic field.

Observations and Properties

The first solar flare ever observed was seen in white light by two independent observers, R. C. Carrington and R. Hodgson, on 1 September 1859. Since then, flare observations have for over a century almost been uniquely carried out photographically in Hα line because of its strong enhancement during flares. With the advent of spacecraft observations from about 1960s onward, the observational data on solar flares in overall wavelengths of the electromagnetic spectrum has increased tremendously. The data from the Orbiting Solar Observatory (OSO) series of satellites, Skylab, and Solar Maximum Mission (SMM) allow us to study in detail the characteristics of flares at wavelengths inaccessible to ground-based observations. The recent improvement of spatial resolution in photography and magnetic field measurements (up to less than 1") and high-resolution imaging (up to 1") of EUV and X-ray emission of the flares has led to a much more detailed and broader description of the flare phenomenon.

Some important properties of the flare have been drawn from observations. For example, almost all flares occur in active regions with sunspots, and the more complex the magnetic signature in the region, the higher the frequency of flares occurrence (e.g., Dodson-Prince and Hedeman, 1970; Priest, 1982a). This clearly indicates that magnetic field is an important ingredient in the flare process. However, the fact that the flares are normally not found above the spot umbrae where the field is strongest shows evidently that aspects other than strength of the field configuration are important. Other interesting properties are the 'sympathy' and 'homology' of some flares. In the first place, a flare may be triggered by occurrence of another flare, even though the two are widely separated. In the second, flares are often observed to occur repeatedly in the same place and with very similar characteristics. This implies that there is a rebuilding of the stressed magnetic field after each successive flare, and no large-scale changes occur in the photosphere beneath a flare. Both sympathetic and homologous behavior emphasizes again the importance of magnetic fields in the flare phenomenon, and suggests that the form of the magnetic field configuration is a determining factor in the process that lead to a flare. This idea is supported by the observed sheared structure of the magnetic field in the region where the flare occurred. Solar physicists now suspect that certain plasma motions that lead to sheared magnetic field structure play a major role in flare production.

Research on Solar Flares

Nearly all models of solar flares are based on the conversion of magnetic energy into heat and kinetic energy since no other source exists in the solar atmosphere which has necessary energy. Basically, to understand why solar flares occurs, one needs to understand several fundamental points, such as:

1) What kind of the stable magnetic configurations can store enough magnetic energy (to supply the flare) before the onset of the flare?
2) What mechanism can convert the stored magnetic energy into heat, kinetic energy and fast particle energy sufficiently rapidly?
3) How does the preflare evolution proceed and eventually trigger a flare?
4) Why and how does a flare evolve through different processes?
4) What is the mechanism for producing and supporting the flare loops; where the material flowing down the legs of flare loops comes from?

Observation and theoretical studies all suggest that magnetic reconnection plays a crucial role in both the process of energy build up and energy release. Accordingly, the basic idea of a magnetic reconnection model of the flare is as follows. The magnetic field is acquiring energy by getting sheared and stressed in response to photospheric plasma motions; and the energy is probably stored in the corona in the form of coronal currents. As the configuration evolves, a prominence eruption is triggered either because of an instability or a loss of magnetic equilibrium. Eventually the energy stored in the currents is released through rapid magnetic reconnection in the flash phase. The prominence eruption leads the closed magnetic field configuration to become open, or at least, partially open. In the main phase, the open field configuration evolves to a closed configuration via magnetic reconnection, and the flare loops are formed. The slow-mode MHD shocks produced by the reconnection convert the released magnetic energy into the thermal and kinetic energy. Finally the heat is conducted along the field lines to the ribbons where the chromospheric plasma is evaporated, and the evaporated plasma flows upwards along the field lines and supplies the material necessary to form the loops.

In principle, a global MHD model for the flare phenomenon can incorporate many different aspects, but in practice it is necessary to focus on specific aspects of the flare

phenomenon in order to solve the MHD equations. Each aspect is important for understanding and developing the whole theory. However, it is impossible to study all such aspects in only one paper. Therefore, the forthcoming chapters of this dissertation will focus on some of the key problems, while at meantime show appropriate concern for consistence with the overview of the total phenomenon.

PART ONE

THE EFFECT OF MAGNETIC RECONNECTION ON THE CATASTROPHIC LOSS OF MAGNETIC EQUILIBRIUM IN FLARES

CHAPTER 1

OVERVIEW

Many large solar flares are associated with the ejection of the overlying plasma and magnetic flux into interplanetary space. Such an ejection is known as a coronal mass ejection (CME), and it can carry a significant amount of energy, magnetic flux and mass into interplanetary space. Thus any model for large eruptive flares must explain not only the formation and evolution of the flare ribbons and loops, but also the ejection of the magnetic flux and plasma into interplanetary space.

In this part of the thesis, a study of a catastrophe mechanism for eruptive flares and related phenomena within the framework of MHD theory will be presented. CME's and prominence eruptions are solar phenomena of the same nature as flares. Like flares, both CME's and prominence eruptions are responses to a disruption of the magnetic field in the corona. In what follows, we will use the term CME to refer to the ejection process, but the readers should keep in mind that the term is used generally to refer to any eruptive process. In order to get some basic ideas about the whole problem, a brief overview of recent study of CME's and related driven models will be necessary.

Driving Mechanism for CME's

Since the early observation of CME's by OSO 7 & Skylab (Tousey, 1973; Gosling et al., 1974), the driving mechanism for CME's has been extensively investigated. Three driving forces which have been proposed are the magnetic force due to coronal currents (Anzer, 1978; Mouschovias and Poland, 1978), the pressure force due to thermal energy generated by flares (Wu et al., 1978; Steinolfson et al., 1978; Steinolfson, 1988), and the

gravitational force due to buoyancy of a pre-existing structure (Low, 1981). However, the pressure mechanism is unpopular because most CME's are associated with prominence eruptions rather than flares (Kahler, 1978). Observations also indicate that the kinetic energy associated with the ejection exceeds the thermal energy released in the flare (Canfield et al., 1980; Webb et al., 1980; Linker et al., 1990), and a flare associated with a CME usually begins several minutes after CME has started (Wagner et al., 1981; Wagner, 1982; Simnett and Harrison, 1985); thus the flare is actually a response to the overall magnetic disruption caused by the ejection (Simnett and Harrison, 1985). As to the gravitational force, it can not be the main driving mechanism for CME's because the gravitational potential energy of the pre-existing structure is estimated to be much less than the energy (10^{25} W) needed for a large CME (Wagner et al., 1981; Yeh, 1982 &1985).

Most of flare researchers favor the ideas that the magnetic force is the major driving force of CME's, though some of them insist that the pressure and gravity must play a role in CME's (Aly, 1991), since the evolution of force-free fields (i.e., the fields in which Lorentz force $\mathbf{J} \times \mathbf{B} = 0$ everywhere) to the fully open state is prohibited. Others think that the mass ejection phenomena cannot be strictly magnetically driven (Yeh and Dryer, 1981; Low, 1984), since the force-free approximation is valid only in the lower corona, in the upper regions, both plasma pressure and gravity are important (Low, 1981; Wolfson, 1982, Wolfson and Gould, 1985).

One major concern with magnetically driven models is how the free magnetic energy is built up. A basic mechanism has been proposed by Gold (1964) according to the 'frozen-in' effect (see discussion in Chapter 2): the footpoints of magnetic field lines are rooted in the dense photosphere where plasma pressure dominates so that the motions of photospheric plasma driven by convection carry with them the footpoints, higher in corona the plasma is tenuous and magnetic pressure dominates, the field in the quiescent state must rearrange itself to new equilibria in response to the change of the

footpoints; currents are therefore induced in the corona by plasma motions (Wolfson and Low, 1992). In this way magnetic energy is stored in the coronal currents and can be released through magnetic reconnection. This possibility has been studied by many authors (Low, 1977 & 1982; Jockers, 1978; Wolfson and Gould, 1985; Wolfson, 1989; Klimchuk and Sturrock, 1989 & 1992; Aly, 1990; Finn and Chen, 1990; Klimchuk, 1990; Lisa, Klimchuk, and Sturrock, 1992).

Since distribution of currents and fields in the corona prior to a CME are not well known, a rich variety of magnetic field configurations have been investigated in modelling the magnetically driven CME's. They include twisted magnetic loops (Hood and Priest, 1979; Van Hoven, 1981), sheared arcades (Birn and Schindler, 1981; Aly, 1985; Zwingmann, 1987; Mikic et al., 1988; Biskamp and Welter, 1989), line currents (Van Tend and Kuperus, 1978; Van Tend, 1979; Sturrock, 1987; Démoulin and Priest, 1988; Steele and Priest, 1990; Forbes, 1990), plasmoids (Pneuman, 1984; Linker et al., 1990), and various arrangement of current sheets (Forbes, 1988; Shibata et al., 1989).

Eruptions and Magnetic Reconnection

CME's are always observed in association with eruptions of solar prominences. The system is thought to evolve through a series of equilibria over a time period of several days before the eruptions; and enough energy is stored in the corona in the form of coronal currents. The transition from quasi-static evolution to dynamic activity may possibly be caused by the evolution of the field configuration to a point where no nearby equilibrium state is available (Low, 1990), and the system loses equilibrium either because of an instability (resistive or ideal) or a catastrophic loss (Moore,1988), as shown in Figure 4.

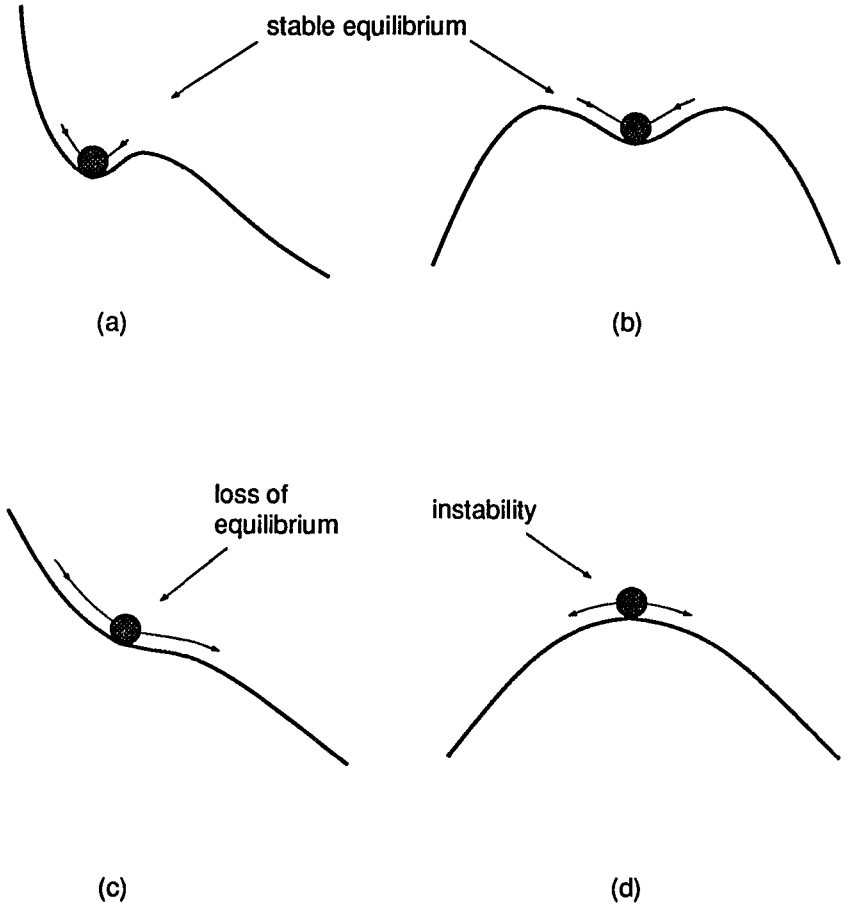

Fig. 4. Schematic diagram of the system evolving from a stable equilibrium state (a, b) to a non-equilibrium state (c) or an unstable state (d).

As mentioned above, eruptions of solar prominences are thought to be caused by an instability or lack of equilibrium in a magnetic arcade, this may occur when the magnetic field is twisted or sheared too much or the prominence altitude becomes too high or the feet become too far apart (Van Tend and Kuperus, 1978; Sturrock, 1980; Hood and Priest, 1980; Zwingmann, 1985; Browning and Priest, 1986; Démoulin and Priest, 1988; Amari and Aly, 1989). During the eruptions, significant magnetic reconnection can occur within a few Alfvén scale times (Priest and Forbes, 1986; Forbes and Isenberg, 1991), releasing energy rapidly. Thus the eruption is expected to drive reconnection and heating in a current sheet that forms about an *x*-type neutral point below the rising prominence (Priest, 1981 & 1985a; Steele and Priest, 1989).

Observations of flare ribbons and loops moving through the chromosphere and corona during the main phase show evidently the occurrence of magnetic reconnection in solar flares. Doppler-shift measurements indicate clearly that the motions of flare ribbons and loops are not due to mass motions of the solar plasma, but rather due to the upward propagation of an energy source in the corona (Schmieder et al., 1987). In MHD model of flares, this propagating energy source is a magnetic *x*-line accompanied by slow-mode shocks.

MHD Models

Although it is well recognized that magnetic force is the major driving force for CME's and eruptive flares, there is little agreement as to what MHD model is appropriate to describe flare phenomenon. Three models which have been extensively investigated are the emerging-flux model (Heyvaerts and Priest, 1976), the magnetic-flux-rope model (Sturrock, 1989), and the sheared-arcade model (Aly, 1990). All of the models are capable to store and release magnetic energy efficiently, provided that the

reconnection occurs. However, only the magnetic-flux-rope model provides a mechanism for ejecting magnetic flux into interplanetary space.

Opening of Magnetic Field

One of the major difficulties in developing an MHD model for CME's and eruptive flares is to understand how a closed magnetic field configuration can evolve to an open configuration. The magnetically driven model requires a mechanism which can eject magnetic flux and plasma by decreasing the total magnetic energy stored in the corona. This means to open the field without increasing field energy. However, for a simply connected force-free field, an open field configuration is the highest magnetic energy state possible (Aly, 1984; 1985; 1990). In other words, the open-field energy represents the least upper bound on the energy of a closed-field state (Yang, Sturrock & Antiochos, 1986; Aly, 1991). Thus the evolution of simply connected force-free fields from closed states to the fully open state is prohibited. However, there are several ways to avoid this prohibition. For instance, the field configuration might have preexisting structures such as current sheets or filament currents in the corona, and therefore, it is not force-free. Or even if the field is force-free, it might not be simply connected but contain '*x*' and/or '*o*' type points. Or the eruption might only extend the field to a large, but finite extent, without actually opening the field lines to infinity—at high altitude (higher than two solar radii) other mechanisms such as the solar wind might act to carry the ejected mass into interplanetary space, thereby opening the field (Sturrock, 1989). It has also been suggested that the transition from a closed-field state to a partially open configuration is energetically possible (Low, 1986 & 1990; Wolfson and Low, 1992), and although the force-free field can not acquire enough energy to open the field fully on its own, it might initiate the disruption (Wolfson and Low, 1992).

Catastrophe Mechanism for Loss of Equilibrium

A simple catastrophe model proposed by Van Tend and Kuperus (1978) suggests that a coronal current filament (also referred to as flux-rope which is treated as massless and different from the surrounding mass prominence) will lose equilibrium when its current exceeds a critical value and then be ejected upwards by magnetic force. The basic mechanism for driving the current filament upwards in the model of Van Tend and Kuperus is shown in Figure 5. A current filament (i.e., flux rope) is supported above the photosphere by the field lines which are tied to the photosphere. When the current in the filament is weak, it is in stable equilibrium, as indicated in the energy diagram on the right side of Figure 5a. As the photospheric convection increases the filament current by reconnecting field lines in the photosphere, the equilibrium position is displaced upwards (Figure 5b), while the potential well becomes shallow. Eventually the filament equilibrium will move upward towards infinity (Figure 5c). The transition from 5a to 5c can occur either continuously or discontinuously, depending crucially on the distribution of the vertical photospheric magnetic field. Catastrophic behavior, i.e., a discontinuous transition, can occur only if the background field falls off with height faster than $1/y$ (Van Tend, 1979).

The model of Van Tend and Kuperus treats the current filament simply as a wire suspended in vacuum by magnetic field lines which are not 'frozen in' the plasma as in ideal MHD. This allows magnetic reconnection to occur freely at the x-line. However, according to MHD theory, such a free reconnection is inhibited in astrophysical plasmas such as the corona because of the high conductivity there. When reconnection is inhibited, a current sheet develops at the x-line below the filament due to the 'frozen-in' condition. However, if reconnection occurs in the current sheet, then the current sheet is weakened, magnetic energy is released, and the filament escapes upwards. Some detailed numerical experiments of reconnection in such a current sheet have been

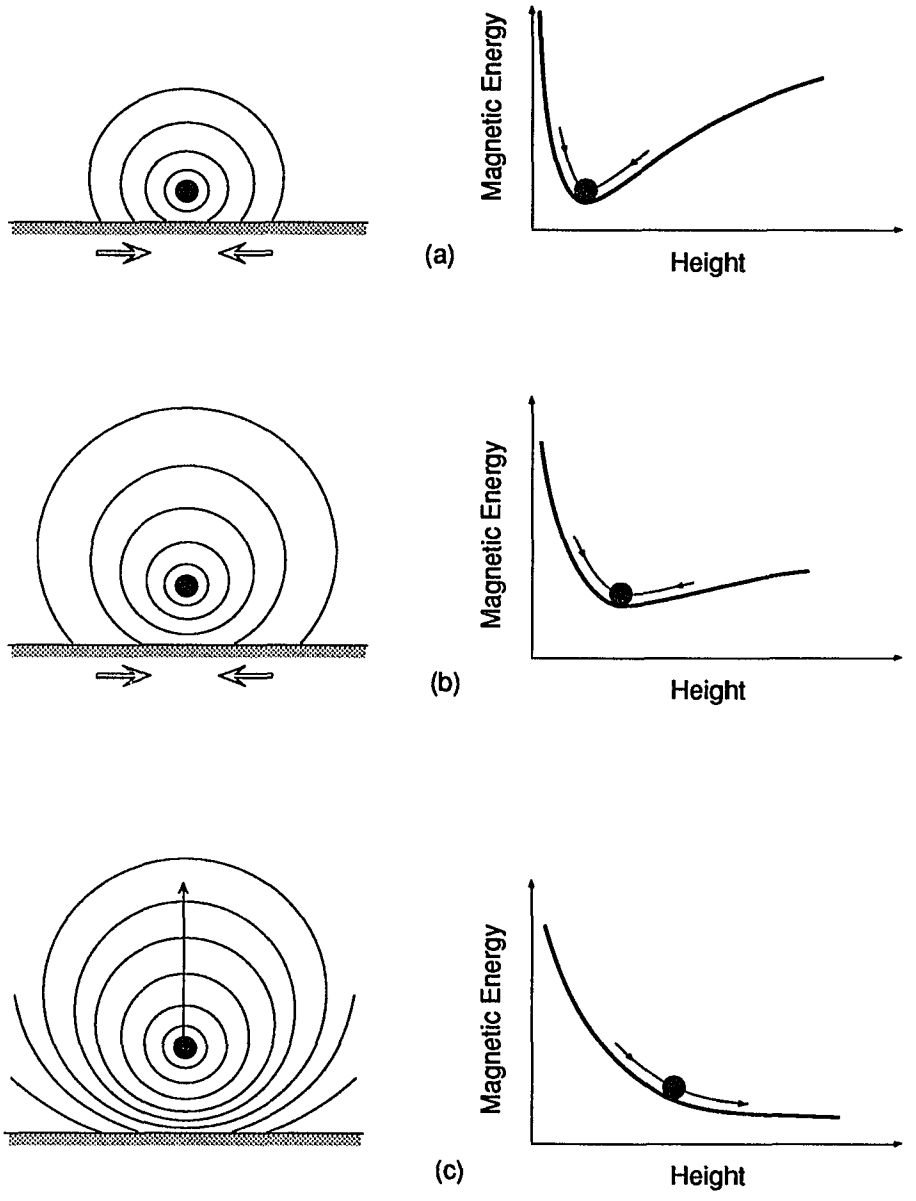

Fig. 5. A schematic diagram of the driving mechanism in the models of the Van Tend and Kuperus type. The dark shaded circle designates the current filament, and solid arrows indicate filament motions. Hollow arrows show the photosphjeric convection which increases the filament current by reconnecting field lines in the photosphere (light shaded region) (after Forbes and Isenberg, 1991).

investigated (Forbes and Priest, 1983; Robertson and Priest, 1987). Several authors have extended the model of Van Tend and Kuperus by adding current sheets which are approximated by line currents (Kaastra, 1985; Molodenskii & Filippov, 1987; Martens and Kuin, 1989). Other authors have developed related model using MHD theory instead (Démoulin and Priest, 1988; Amari and Aly, 1989; van Ballegooijen and Martens, 1989; Anzer and Ballester, 1990; Priest and Forbes, 1990).

The formation of a current sheet generally increases the total magnetic energy, but the magnetic energy has to decrease in order to drive a CME magnetically. Thus an understanding of how such a current sheet develops in a CME while decreasing the total magnetic energy of the system becomes critical. Several studies have been completed in dealing with this open question (Sturrock, 1987; Mikic et al., 1988; van Ballegooijen & Martens, 1989; Biskamp and Welter, 1989).

Another important concern with catastrophe mechanisms is whether a purely force-free field can ever exhibit an MHD catastrophe. The possibility has been questioned by Klimchuk and Sturrock (1989, 1992). They found that the catastrophe-like behavior occurs in a force-free configuration used by Low (1977) was actually an artifact of the solution method. This led Sturrock (1989) to speculate that only non-force-free systems can exhibit catastrophic-type behavior. However, recent work by Isenberg, et al. (1992) shows that for two-dimensional system, this conclusion is not correct. The corresponding model is discussed in the next section.

Model of Forbes and Isenberg

Forbes and Isenberg (1991) constructed a two-dimensional ideal MHD version of Van Tend and Kuperus model, in which a catastrophic behavior does occur under certain conditions. Their work shows that it is indeed energetically possible to create

an eruption by eliminating the requirement that the field be magnetically opened to infinity during the ideal MHD transition (Démoulin and Priest, 1988; Forbes and Isenberg, 1991).

In their model a current sheet, which is always attached to the photosphere, develops below the filament during the evolution of the field configuration. The field is assumed to be force-free everywhere except possibly inside of the filament and current sheet. The evolution is basically a two-stage process. The first stage is a storage phase in which the magnetic energy is slowly stored in corona through photospheric reconnection which transfers the flux from the photosphere to the corona. This stage occurs quasi-statically over a time period of several days, so that the system evolves through a series of equilibria. The second stage is the eruptive phase which occurs when equilibrium is lost. By using an energy analysis, Forbes and Isenberg (1991) have been able to show that when the filament radius is less than a specific value, a catastrophic eruption is energetically possible. This ideal MHD eruption does not open the field to infinity but simply extends it.

CHAPTER 2

A RECONNECTION MODEL WITH A DETACHED CURRENT SHEET

A limitation of the Forbes and Isenberg (1991) model is the assumption that no reconnection occurs in the corona and that the plasma there is perfectly conducting (i.e., ideal). This artificial condition has been imposed in their model because it is mathematically convenient. Specifically, this assumption causes the current sheet which forms to stay always attached to the boundary. This allows the field to be determined by solving Poisson's equation with Dirichlet boundary conditions.

In reality, the coronal plasma is not perfectly conducting and reconnection will cause the current sheet to become detached from the boundary. By allowing a detached current sheet to form at the x-line below the filament, we can analyze the effect of magnetic reconnection in the corona. A study of such a process helps us to get a better understanding of the effect of reconnection on prominence equilibrium and eruption.

A detached current sheet problem is much more difficult to solve mathematically because of its mixed boundary conditions, and it is probably the main reason why this problem has so far not been dealt with rigorously. As we will see in the forthcoming chapters, the problem of determining the equilibria reduces to solving Poisson's equation with mixed Dirichlet and Neumann boundary conditions. Then the mixed boundary value problem is transformed to a singular integral equation which can be solved by the approach introduced by Muskhelishvili (1953). In general, the solution of this integral equation may not exist in a closed analytical form, but, as will be shown in Chapter 3, closed solutions do exist for our problem.

In the sections that follow, an MHD version of the catastrophe model of Van Tend and Kuperus (Van Tend and Kuperus, 1978; Van Tend, 1979) will be developed which allows magnetic reconnection to be incorporated. The new model lies between the extremes of uninhibited reconnection assumed in the circuit models (e.g., Martens and Kuin, 1989) and no reconnection assumed by Forbes and Isenberg (1991). In Chapter 3 a mixed boundary value problem for Poisson's equation will be solved to give the magnetic vector potential for a field configuration containing a detached current sheet and satisfying line-tied boundary conditions in the photosphere. In Chapter 4 the solution of the mixed boundary value problem is used to determine the effect of magnetic reconnection upon the equilibria previously found by Forbes and Isenberg (1991).

Basic Equations and Considerations

Although this thesis consists of two parts, the two parts share some common physical considerations which are fundamental to the flare phenomenon, such as the 'frozen-flux' condition and the magnetic reconnection process. These processes will be discussed briefly after the specification of the basic MHD equations.

The basic magnetohydrodynamic equations used throughout this dissertation are given by Priest (1982a):

$$\partial \mathbf{B}/\partial t = \nabla \times (\mathbf{v} \times \mathbf{B}) + \eta \nabla^2 \mathbf{B}, \tag{2-1a}$$

$$D\rho/Dt + \rho \nabla \cdot \mathbf{v} = 0, \tag{2-1b}$$

$$\rho (D\mathbf{v}/Dt) + \nabla p = \mathbf{j} \times \mathbf{B} + \mathbf{F}, \tag{2-1c}$$

$$\rho^{\gamma} (D/Dt)(p\rho^{-\gamma}) = (\gamma - 1)(-\nabla \cdot \mathbf{q} - L_r + j^2/\sigma + H), \tag{2-1d}$$

$$p\rho^{-\gamma} = \text{constant}, \tag{2-1e}$$

where

$$D/Dt \equiv \partial/\partial t + \mathbf{v}\cdot\nabla$$

is the material derivative for time variations following the motion. The quantities $\mathbf{v}$, $\mathbf{B}$, $\mathbf{j}$, ρ, p and T are the coronal plasma velocity, the magnetic field, the current density, the mass density, the pressure, and the temperature, respectively. The force $\mathbf{F} = \mathbf{F}_g + \mathbf{F}_v$ is the sum of the gravitational force and the viscous force, and η is the magnetic diffusivity, γ the ratio of specific heats, $\mathbf{q}$ the heat flux, L_r the net radiation, j^2/σ the ohmic heating, H the sum of all the other heating sources.

The five equations above are the induction equation, the conservation equations for mass, momentum and energy, and the adiabatic equation of state, respectively. The current density $\mathbf{j}$ is given by Ampere's law:

$$\mathbf{j} = \nabla \mathrm{x} \mathbf{B}/\mu, \tag{2-2}$$

where μ is the magnetic permeability (for the solar plasma, $\mu \approx \mu_0 = 4\pi \mathrm{x}\ 10^{-7}\ \mathrm{Hm}^{-1}$), while $\mathbf{B}$ satisfies

$$\nabla\cdot\mathbf{B} = 0. \tag{2-3}$$

The 'frozen-flux' effect is a fundamental consideration in ideal MHD theory. It was proposed by H. Alfvén and can be summarized in words as follows: "In a perfectly conducting plasma, magnetic field lines behave as if they move with the plasma." In other words, the magnetic flux through a surface moving with the plasma is conserved. Here the perfectly conducting plasma is the plasma in which large magnetic Reynolds number limit (i.e., ideal MHD condition) holds. A brief argument is as follows.

The magnetic Reynolds number is an important parameter of plasma defined by

$$R_m = L_0 V_0/\eta. \tag{2-4}$$

where V_0 and L_0 are the typical plasma speed and length-scale under consideration (e.g., Priest, 1982a). The magnetic Reynolds number R_m represents the ratio of the convective to diffusive terms in the induction equation (2-1a), i.e.,

$$|\nabla \times (\mathbf{v} \times \mathbf{B})| / |\eta \nabla^2 \mathbf{B}| \sim L_0 V_0/\eta.$$

When $R_m >> 1$, Equation (2-1a) becomes approximately

$$\partial \mathbf{B}/\partial t = \nabla \times (\mathbf{v} \times \mathbf{B}). \tag{2-5}$$

Now consider a surface S bounded by a closed curve C moving with the plasma. The magnetic flux through S is $F = \iint \mathbf{B} \cdot d\mathbf{s}$, and its rate of change (DF/Dt) consists of two parts: changes in the magnetic field with time and changes due to the motion of the boundary, i.e.,

$$\frac{DF}{Dt} = \int\int_S \frac{\partial \mathbf{B}}{\partial t} \cdot d\mathbf{s} - \oint_C (\mathbf{v} \times \mathbf{B}) \cdot d\mathbf{l},$$

where $d\mathbf{s}$ is the area element of S, $d\mathbf{l}$ the length element of C. Via Stoke's theorem, the above equation becomes

$$\frac{DF}{Dt} = \int\int_S [\frac{\partial \mathbf{B}}{\partial t} - \nabla \times (\mathbf{v} \times \mathbf{B})] \cdot d\mathbf{s},$$

which vanishes by Equation (2-5).

For most solar atmospheric phenomena R_m has a value much larger than unity so that the ideal MHD condition holds. For instance, for typical flare loops, $V_0 \approx 10^4$ ms^{-1}, $L_0 \approx 10^7$ m, $\eta \approx 10^4$ m^{2}s^{-1}, which gives an R_m of order 10^7! Thus for flare loops, the magnetic field lines are frozen into the plasma so that either the field lines are carried by plasma motions or the plasma is dragged by magnetic field movement. The magnetic energy build up through plasma motions is an example of this 'frozen-flux' effect.

The huge value of R_m in most solar phenomena comes mainly from the great spatial size of these phenomena. However, for some very small-scale phenomena in the solar atmosphere, such as current sheets of 1 km or less in thickness, R_m may be of order of unity, and the ideal MHD condition no longer holds. Under these circumstances, the magnetic field lines can slip through the plasma so that magnetic reconnection occurs.

In response to an applied photospheric motions, a current sheet may develop when the region near an x-type neutral point collapses, when topologically separated parts of a magnetic configuration are pushed together, or when a magnetohydrostatic equilibrium becomes unstable. In the absence of flow, a current sheet diffuses away at a speed η/l where l is the thickness of the sheet (see Equation (2-1a)). The dimensions of the current sheet depend on the field strength and photospheric speed. If the plasma and magnetic flux are brought towards the sheet from the sides at speed v_l, then the sheet expands when $v_l < \eta/l$, while it becomes thinner when $\eta/l < v_l$. Eventually a steady state is maintained when $v_l = \eta/l$.

One effect of the current sheet is to reconnect the field lines. Magnetic reconnection may be generated spontaneously by a resistive instability, such as the tearing mode, but the reconnection may also be driven by an outside flow carrying oppositely directed field lines towards the sheet. According to a recent analysis by Forbes and Priest (1987), driven reconnection is limited only by the Alfvén speed and the rate at which the flows are pushed together. By contrast, spontaneous reconnection is limited by the magnetic diffusivity (see also Yeh and Axford, 1970).

The best known theory for driven reconnection is Petschek's (1964). In Petschek's theory, pairs of slow-mode shock waves propagate from the ends of the current sheet and remain as standing waves in a steady flow. These slow-mode shocks can convert magnetic energy into heat and flow energy sufficiently effectively (Petschek, 1964).

Figure 6 shows a schematic diagram for Petschek-like reconnection. In Petschek's theory the reconnection rate depends only on the log of the magnetic diffusivity, and for typical coronal values it implies that the reconnection flow can be driven at about o.1 times the Alfvén speed.

Basic Assumptions

When considering the model for CME's, a basic assumption is the characteristic time scales for different physical processes. For our model, we will assume that there are three distinctive time scales, namely the photospheric convective time scale τ_p, the reconnection time scale τ_r, and the Alfvén time scale τ_A. The photospheric evolution prior to the eruption lasts typically several days during which the magnetic energy is built up gradually in the corona, therefore τ_p ~ days. The release of the magnetic energy through reconnection in a solar flare usually lasts over a time-scale of an hour or so, which suggests that τ_r ~ hour. The Alfvén time scale for flares is about a minute, and thus τ_A ~ minute.

Here we are going to assume that $\tau_p >> \tau_r >> \tau_A$, and that the overall evolution of the eruption is modelled as a three-stage process. The first stage is the storage phase in which the magnetic energy is slowly stored in the corona as a result of the convective motions in the photosphere. During this storage phase, the kinetic energy of the convective motion is converted to magnetic energy and magnetic flux is transferred from the photosphere to the corona. The evolution is quasi-static in a time period of τ_p, as the system evolves through a series of equilibria until it reaches a point where no nearby equilibria are available. The second stage is the eruptive phase which occurs when equilibrium is lost due to the further evolution of the system beyond the critical point. As soon as the equilibrium is lost, the evolution of the system becomes very rapid so that the eruptive phase lasts only a few minutes (i.e., a few Alfvén time scales).

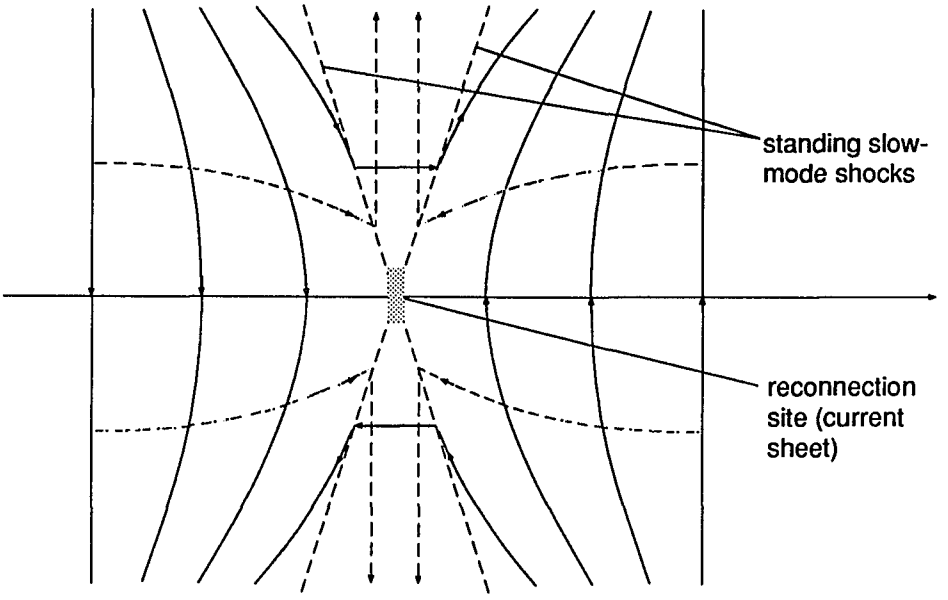

Fig. 6. A schematic diagram showing magnetic field lines (solid) and streamlines (dashed) for Petschek-like reconnection.

Compared to the rate at which the flux is transferred from the photosphere to the corona ($\sim 1/\tau_p$), the flux in the corona can be considered as constant during the eruptive phase. In other words, there is no energy input during the eruption. Finally, the third stage is the reconnection phase which occurs after the eruptive phase. During this phase the system evolves due to the destruction of the current sheet by reconnection, and again it is assumed that there is no energy input from the photosphere during this stage. We will arbitrarily assume that $\tau_r >> \tau_A$, but it should be kept in mind that τ_r could be almost as small as τ_A.

Several other assumptions used in the model are as follows:

a) Two-dimensional model—the magnetic field is assumed to lie in the x-y plane with all quantities invariant in the z direction, so that the physical quantities such as force and energy are measured per unit length except as otherwise stated.

b) Strong magnetic field approximation—the pressure in the corona is assumed to be zero except where the current filament and sheet are located. In a two-dimensional (2-D) model with no magnetic field component perpendicular to the 2-D plane, a zero-pressure assumption will cause all currents (i.e., filament and sheet) to become concentrated into thin line currents or sheets (Syrovatskii, 1971; Forbes & Isenberg, 1991). Therefore the pressure inside the currents must be kept finite to prevent them from becoming infinitely thin and the corresponding magnetic energy from becoming infinitely large.

c) Incompressible approximation—the filament is assumed to be an incompressible cylinder ($\gamma \rightarrow \infty$ in the equation of state) of constant radius r during the evolution. Since the plasma is highly compressible outside the filament, this assumption implies there is an abrupt change in the state on the boundary of the filament.

d) No $\mathbf{F}_g$ and $\mathbf{F}_v$—the gravitational force and the viscous force are assumed not to be important.

e) Inertial line-tied boundary conditions—the line-tied boundary conditions are satisfied during the eruptive phase. This means that the photospheric foot points of magnetic field lines cannot move during the course of the flare. Such boundary conditions occur because the inertial mass of the photosphere plasma is very much greater than that of the corona.

Formulation of the MHD Model

During the storage phase, the evolution is quasi-static. By using the assumptions prescribed in the last section, the equations which determine the coronal magnetic field $\mathbf{B}$ and current density $\mathbf{j}$ can be deduced from Equations (2-1) ~ (2-3):

$$\mathbf{j} \times \mathbf{B} = \nabla p, \tag{2-6a}$$

$$\nabla \times \mathbf{B} = \mu \mathbf{j}, \tag{2-6b}$$

$$\nabla \cdot \mathbf{B} = 0. \tag{2-6c}$$

Let $\mathbf{j}_f$ denote the current density in the filament which is a cylinder of constant radius r, $\mathbf{B}_f$ and $\mathbf{B}_e$ denote the magnetic fields due to the internal current of the filament and the external currents outside the filament, respectively, then

$$\mathbf{B} = \mathbf{B}_f + \mathbf{B}_e, \tag{2-7}$$

and the condition for filament equilibria dissociates into two parts. From Equation (2-6a), the internal, local equilibrium inside the filament is given by

$$\mathbf{j}_f \times \mathbf{B}_f = \nabla p, \tag{2-8}$$

while the external, global condition is determined by

$$\mathbf{F} = \iint_S (\mathbf{j}_f \times \mathbf{B}_e)\, ds, \tag{2-9}$$

where $\mathbf{F}$ is the external force (per unit length) on the filament, and S represents the cross-section of the filament. The quantity ds is the area element of S. When the area of S is small enough to make the external field $\mathbf{B}_e$ effectively uniform within the filament, Equation (2-9) becomes

$$\mathbf{F} = I B_{e0}\, \hat{\mathbf{y}}, \tag{2-10}$$

where $B_{e\,0}$ is the external field evaluated at the filament, $\hat{\mathbf{y}}$ is the unit vector of force $\mathbf{F}$, and I is the filament current

$$I = \iint_S j_f\, ds. \tag{2-11}$$

The global filament equilibria condition is $\mathbf{F} = 0$, which is satisfied when

$$B_{e0} = 0. \tag{2-12}$$

The magnetic field configuration must be solved in order to determine the global equilibria for the filament, as prescribed by Equation (2-12). To specify the vector potential problem for the magnetic field a coordinate system is chosen as follows.

In the x-y plane, the upper half plane is the coronal region, the lower half plane is the photosphere, and the photospheric boundary coincides with the horizontal axis. The current filament is centered on the y-axis at height h, as shown in Figure 7a.

Poisson's equation for the magnitude of the vector potential A is obtain from Equations (2-6)

$$\nabla^2 A = -\mu j(x, y), \tag{2-13}$$

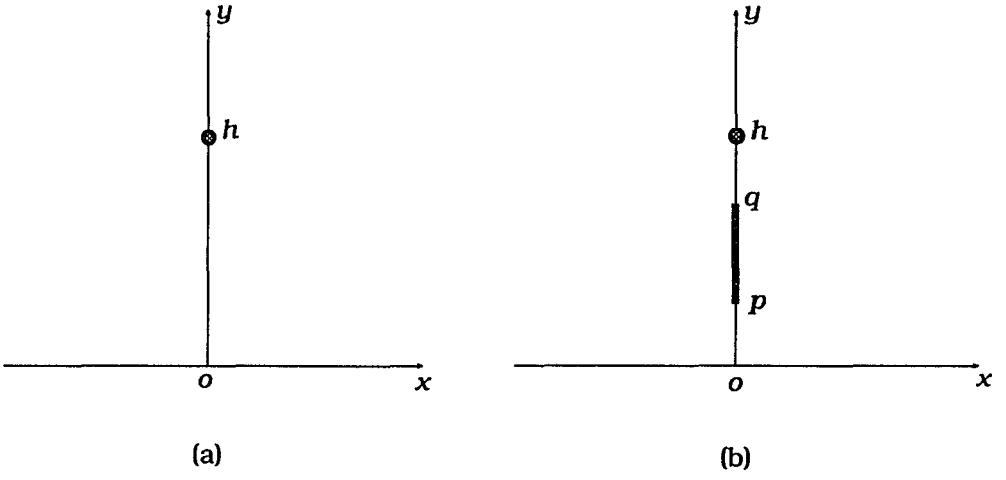

Fig. 7. Geometry of the field configuration: (a) with no current sheet; (b) with a detached current sheet.

where A is defined by $\mathbf{B} = \nabla A \times \hat{\mathbf{z}}$.

If I_l is the initial filament current, h_l is the initial filament height, and initial value of $j(x, y)$ is assumed to be uniform within the filament, then, at the start of quasi-static evolution,

$$j(x, y) = \frac{I}{\pi r^2}\{1 - \mathcal{H}[\sqrt{x^2 + (y - h)^2} - r]\}, \tag{2-14}$$

where $\mathcal{H}$ is the Heaviside step-function. As the system evolves, the current density within the filament is assumed to remain fixed, while a surface current is induced on the filament boundary.

As regards the photospheric boundary condition, a line dipole of strength m at a depth d below the photosphere is chosen to represent the boundary field so that

$$A(x, 0) = \frac{md}{x^2 + d^2} - \phi(t), \tag{2-15}$$

where $\phi(t)$ is a slowly varying function of time. In a multipole expansion of an arbitrary boundary field, the line dipole term is the first term which allows a catastrophe to occur (Van Tend, 1979; Démoulin & Priest, 1988; Forbes and Isenberg, 1991). Thus the above choice is the simplest one with catastrophe-like behavior.

We will assume that the same distribution of normal magnetic field at the photospheric boundary is maintained during the quasi-static evolution of MHD equilibria. Other choices are possible, but this one is convenient because it is the same one made previously by Forbes and Isenberg (1991). Thus, this choice will facilitate comparison. From $dA/dt = 0$ and the line-tied requirement, the tangential flow velocity at the photospheric boundary is

$$v_x(x, 0) = -\frac{(x^2 + d^2)^2}{2md} \frac{\mathrm{d}\phi}{\mathrm{d}t}, \tag{2-16}$$

by Equation (2-15). This flow pattern transports new field lines from $x = \pm\infty$. Although this flow pattern above is not especially realistic, it does show the basic picture for the quasi-static evolution caused by the gradual reconnection of the photospheric field. It is clear now that $(d\phi/dt)$ represents the rate at which the flux is transferred from the photosphere to the corona, and thus it gives a measure of the rate at which magnetic energy is stored in the corona.

CHAPTER 3

SOLUTION FOR THE VECTOR POTENTIAL

In the last chapter a vector potential problem for magnetic field configuration was formulated, which is so far the same as the problem considered by Forbes and Isenberg (1991). The evolution of the photospheric field via an increase in ϕ eventually causes a current sheet to form at the x-line (i.e., the neutral point in the x-y plane). Here, unlike Forbes and Isenberg (1991), we will consider that a current sheet does not form until a loss of equilibrium occurs. Such an assumption means that the x-line will no longer be at the photospheric surface when the current sheet forms and that the current sheet will be detached.

Generalized Vector Potential Problem

A field configuration which contains a detached current sheet is shown in Figure 7b. As before, the filament is centered on the y-axis at $y = h$, but a current sheet appears along the y-axis between points p and q. In principle, the vector potential can be solved when the current distribution in the sheet is specified. However, in order to solve the problem analytically, we assume that the radius of the filament is much smaller than the photospheric scale length such that the filament acts like a line-current at large distances.

As the system evolves, the current distribution within the filament changes, but since the filament radius r is small, the corresponding magnetic field is approximately the same as that produced by a line current of strength I_f at the location $y = h$. That is

$$j_f(x, y) = I_f\, \delta(x)\, \delta(y - h), \tag{3-1}$$

as long as $|\sqrt{x^2 + y^2} - h| >> r$. Here δ is the δ-function. As for the current sheet, a similar argument leads to

$$j_c(x, y) = I_c(y)\, \delta(x)\, [\mathcal{H}(y - p) - \mathcal{H}(y - q)], \tag{3-2}$$

as long as the distance from current sheet to the point of concern is much larger than the thickness of the sheet. Here $I_c(y)$ represents the current distribution in the sheet, and $\mathcal{H}$ is the Heaviside step-function.

Equations for the Vector Potential

The equations for the vector potential problem of the field configuration with a detached current sheet are derived from Equations (2-13), (2-15), (3-1), and (3-2). They are

$$\nabla^2 A(x, y) = -\mu\pi I_0 j(x, y), \quad y \geq 0, \tag{3-3a}$$

$$A(x, 0) = \frac{\mu I_0}{x^2 + 1} - \phi(t), \tag{3-3b}$$

$$j(x, y) = \delta(x)\, \{J\, \delta(y - h) + I(y)\, [\mathcal{H}(y - p) - \mathcal{H}(y - q)]\}, \tag{3-3c}$$

where $I_0 = m/(d\mu)$, $J = I_f/(I_0\pi)$, $I(y) = I_c(y)/(I_0\pi)$, and x, y, h, and r are normalized to the scale length d.

In general, the current distribution in the sheet, $I(y)$, is unknown therefore it needs to be solved according to the condition that there is no normal component of magnetic field on the current sheet, i.e.,

$$B_x(0, y) = (1/d)\, (\partial A/\partial y)|_{x = 0} = 0, \quad q \geq y \geq p. \tag{3-4}$$

Solution for the Vector Potential

General Form of the Solution

A general form of solution for Equation (3-3a) is obtained by using the method of Green's function

$$A(x, y) = \frac{\mu I_0}{4}\int_{-\infty}^{\infty}\int_{0}^{\infty} G(x, y; u, v)\, j(u, v)\, du\, dv + \frac{1}{4\pi}\int_{-\infty}^{\infty} A(u, 0)\left.\frac{\partial G}{\partial v}\right|_{x=0} du, \qquad (3\text{-}5)$$

where $G(x, y; u, v)$ is the 2-D Green's function for the Dirichlet problem

$$G(x, y; u, v) = \ln[(x-u)^2 + (y+v)^2] - \ln[(x-u)^2 + (y-v)^2]. \qquad (3\text{-}6)$$

Substitution of Equations (3-3*b*), (3-3*c*) and (3-6) into Equation (3-5) gives

$$A(x, y) = \frac{\mu I_0}{4}\left[J \ln\frac{x^2 + (y+h)^2}{x^2 + (y-h)^2} + \int_p^q \ln\frac{x^2 + (y+v)^2}{x^2 + (y-v)^2} I(v)\, dv + \right.$$
$$\left. + \frac{1}{\pi}\int_{-\infty}^{\infty} \frac{4y}{y^2 + (x-u)^2}\frac{du}{u^2+1}\right] - \phi(t). \qquad (3\text{-}7)$$

The magnetic field along the y-axis is

$$B_x(0, y) = \frac{\mu I_0}{d}\left[\frac{J}{2}\left(\frac{1}{h-y} + \frac{1}{h+y}\right) + \int_p^q \frac{I(v)\, v\, dv}{v^2 - y^2} + \frac{1}{\pi}\int_{-\infty}^{\infty} \frac{u^2 - y^2}{(y^2+u^2)^2}\frac{du}{u^2+1}\right], \qquad (3\text{-}8)$$

where the first two terms on the RHS of Equation (3-8) are due to the field produced by the filament current and its image, and the last two terms are due to the current sheet and boundary field, respectively. Therefore the fields B_f and B_e defined by Equation (2-7) are respectively

$$B_f(0, y) = \frac{\mu I_0}{2d} \frac{J}{h - y}, \tag{3-9a}$$

$$B_e(0, y) = \frac{\mu I_0}{d}\left[\frac{1}{2}\frac{J}{h + y} + \int_p^q \frac{I(v)\, v\, dv}{v^2 - y^2} + \frac{1}{\pi}\int_{-\infty}^{\infty} \frac{u^2 - y^2}{(y^2 + u^2)^2} \frac{du}{u^2 + 1}\right]. \tag{3-9b}$$

Solution with No Current Sheet

When there is no current sheet, $I(y) = 0$, the potential and the field along the y-axis are given by

$$A(x, y) = \frac{\mu I_0}{4}\left[J \ln \frac{x^2 + (y + h)^2}{x^2 + (y - h)^2} + \frac{4(y + 1)}{x^2 + (y + 1)^2}\right] - \phi(t), \tag{3-10}$$

$$B_x(0, y) = \frac{\mu I_0}{2d}\left[J\left(\frac{1}{h - y} + \frac{1}{h + y}\right) - \frac{2}{(y + 1)^2}\right], \tag{3-11}$$

and the reconnected flux between the filament and the photosphere can be obtained by integrating Equation (3-11) from $y = 0$ to $y = h - r$, i.e., $\phi = A(0, h - r) - A(0, 0)$. Therefore

$$\phi = (\mu I_0/2)\{J \ln [(2h/r) - 1] - 2(h - r)/(h - r + 1)\}, \quad h > r. \tag{3-12}$$

By solving equations (3-10) and (3-12) simultaneously, the potential A and the filament current J can be expressed as the functions of the filament height h and the reconnected flux ϕ.

Current Distribution $I(y)$

When there is a current sheet, the corresponding current distribution, $I(y)$, in the sheet must be determined before the potential is computed. Substitution of Equation (3-4) into Equation (3-8) gives

$$\int_p^q \frac{I(v)\, v\, dv}{y^2 - v^2} = \frac{J h}{h^2 - y^2} + \frac{1}{\pi}\int_{-\infty}^{\infty} \frac{u^2 - y^2}{(y^2 + u^2)^2}\frac{du}{u^2 + 1}, \quad \text{for } q > y > p. \tag{3-13}$$

Let $y^2 = t_0$, $v^2 = t$, then a singular integral equation can be derived from Equation (3-13)

$$f(t) = \frac{1}{t\pi}\int_L \frac{\varphi(t)\, dt}{t - t_0}, \qquad \text{on} L, \tag{3-14}$$

where L is a segment of the real axis of the complex plane (t, η), and the points t, t_0 are on L: $a < t, t_0 < b$. Here $a = p^2$ and $b = q^2$ are the two ends of L, and the functions $f(t)$ and $\varphi(t)$ are

$$f(t) = -\frac{J h}{h^2 - t} + \frac{2}{\pi}\int_{-\infty}^{\infty} \frac{u^2}{u^2 + t}\frac{du}{(u^2 + 1)^2}, \tag{3-15a}$$

$$\varphi(t) = i\pi I(t)/2, \tag{3-15b}$$

where the integral identity

$$\frac{1}{\pi}\int_{-\infty}^{\infty} \frac{y^2 - u^2}{(y^2 + u^2)^2}\frac{du}{u^2 + 1} = \frac{2}{\pi}\int_{-\infty}^{\infty} \frac{u^2}{u^2 + y^2}\frac{du}{(u^2 + 1)^2}, \tag{3-15c}$$

has been used.

The singular integral equation (3-14) can be solved by using the theory of complex variables (Muskhelishvili, 1953). In general, There are four different solutions—one is bounded at both ends of L, two are unbounded at either end of L, and one is unbounded at both ends of L (see Appendix A for the detailed derivation of the solution). However, when considering the symmetric properties of the two ends of the current sheet and the physical condition that the field vanishes at infinity, it is appropriate to choose the solution which is unbounded at both ends of L. That is

$$\varphi(t_0) = \frac{1}{i\pi}\int_L \frac{\sqrt{(t-p^2)(q^2-t)}}{\sqrt{(t_0-p^2)(q^2-t_0)}}\frac{f(t)\,dt}{t-t_0} + \frac{P(t_0)}{\sqrt{(t_0-p^2)(q^2-t_0)}}, \tag{3-16}$$

Substitution of Equations (3-15) and $v^2 = t_0$, $y^2 = t$ into Equation (3-16) gives

$$I(v) = \frac{4}{\pi^2}\int_p^q \left[\frac{Jh}{h^2-y^2} - \frac{2}{\pi}\int_{-\infty}^{\infty}\frac{u^2}{u^2+y^2}\frac{du}{(u^2+1)^2}\right]\frac{\sqrt{(y^2-p^2)(q^2-y^2)}}{\sqrt{(v^2-p^2)(q^2-v^2)}}\frac{y\,dy}{y^2-v^2} + \frac{P(v^2)}{\sqrt{(v^2-p^2)(q^2-v^2)}}, \tag{3-17}$$

where $P(v^2)$ is an arbitrary polynomial of v^2.

By using Equation (3-13) and evaluating the integrals on the RHS of Equation (3-17) (some integral results are shown in Appendix A), a final form of the current distribution, $I(v)$, is

$$I(v) = \frac{2}{\pi}\frac{\mathcal{F}(v)}{\sqrt{(v^2-p^2)(q^2-v^2)}}, \tag{3-18a}$$

where

$$\mathcal{F}(v) = A_0 - \frac{Jh\sqrt{(h^2-p^2)(h^2-q^2)}}{h^2-v^2} - \frac{2}{\pi}\int_{-\infty}^{\infty}\frac{\sqrt{(u^2+p^2)(u^2+q^2)}}{(u^2+v^2)(u^2+1)^2}u^2du, \tag{3-18b}$$

and A_0 is an arbitrary constant. The last term on the RHS of Equation (3-18*b*) can be evaluated by using the complete elliptic integrals (see also Appendix A):

$$\frac{2}{\pi}\int_{-\infty}^{\infty}\frac{\sqrt{(u^2+p^2)(u^2+q^2)}}{(u^2+y^2)(u^2+1)^2}u^2du = \frac{2}{\pi q}\left\{\frac{q^2}{y^2-1}\left[\frac{p^2-1}{q^2-1}K(k)-E(k)\right]+ \right.$$
$$\left. +2\frac{(y^2-p^2)y^2}{(y^2-1)^2}\Pi\left(\frac{y^2}{q^2}-1,k\right)+\frac{1}{(y^2-1)^2}\left[y^2(p^2-2)+\frac{y^2-1}{q^2-1}-p^2\frac{y^2-q^2}{q^2-1}\right]\Pi\left(\frac{1}{q^2}-1,k\right)\right\},$$

where $k^2 = 1 - p^2/q^2$, K, E, and Π are the complete elliptic integrals of the first, the second, and the third kind, respectively.

Solution with a Current Sheet

When there is a current sheet, the corresponding potential and the magnetic field along the y-axis can be calculated by substituting the current distribution, Equations (3-18), into the general form of the solution, Equations (3-7) and (3-8). The field along the y-axis is

$$B_x(0, y) = \frac{\mu I_0}{d}\left[\frac{Jh}{h^2 - y^2} + \int_p^q \frac{I(v)\, v\, dv}{v^2 - y^2} - \frac{1}{(y+1)^2}\right]$$

$$= \begin{cases} \dfrac{\mu I_0}{d} \dfrac{\mathcal{F}(y)}{\sqrt{(p^2 - y^2)(q^2 - y^2)}}, & 0 \le y < p, \\ 0, & p < y < q, \\ -\dfrac{\mu I_0}{d} \dfrac{\mathcal{F}(y)}{\sqrt{(y^2 - p^2)(y^2 - q^2)}}, & y > q, \end{cases} \tag{3-19}$$

In solving for the current distribution, $I(v)$, the solution which is unbounded at both ends of the current sheet has been chosen . This solution generally causes the magnetic field to be unbounded at both ends of the current sheet, as indicated in Equation (3-19). However, the singularities are actually removed by the 'Y-point' condition—the magnetic field vanishes at both ends of the current sheet (Bhattacharjee & Wang, 1991; Forbes & Isenberg, 1991). The Y-points originate from the neutral X-point—when the current develops, the X-point is pulled out to from two Y-points.

The conditions $B_x(0, p) = 0$ and $B_x(0, q) = 0$ lead to $\mathcal{F}(p) = 0$ and $\mathcal{F}(q) = 0$. That is

$$A_0 = Jh\sqrt{\frac{h^2 - q^2}{h^2 - p^2}} + \frac{2}{\pi}\int_{-\infty}^{\infty} \sqrt{\frac{u^2 + q^2}{u^2 + p^2}} \frac{u^2\, du}{(u^2+1)^2}, \tag{3-20a}$$

$$A_0 = Jh\sqrt{\frac{h^2 - p^2}{h^2 - q^2}} + \frac{2}{\pi}\int_{-\infty}^{\infty} \sqrt{\frac{u^2 + p^2}{u^2 + q^2}} \frac{u^2\, du}{(u^2+1)^2}. \tag{3-20b}$$

Elimination of A_0 gives

$$Jh = \frac{2}{\pi}\int_{-\infty}^{\infty} \frac{\sqrt{(h^2-p^2)\,(h^2-q^2)}}{\sqrt{(u^2+p^2)\,(u^2+q^2)}}\,\frac{u^2\,du}{(u^2+1)^2}, \tag{3-21a}$$

hence the constant A_0 is determined as

$$A_0 = \frac{2}{\pi}\int_{-\infty}^{\infty} \frac{h^2+u^2}{\sqrt{(u^2+p^2)\,(u^2+q^2)}}\,\frac{u^2\,du}{(u^2+1)^2}. \tag{3-21b}$$

The above results, Equations (3-20) and (3-21), are substituted into Equation (3-18*b*) to obtain

$$\mathcal{F}(v) = \frac{2}{\pi}\int_{-\infty}^{\infty} \frac{(q^2-v^2)\,(v^2-p^2)}{\sqrt{(u^2+p^2)\,(u^2+q^2)}}\left(\frac{1}{u^2+v^2}+\frac{1}{h^2-v^2}\right)\frac{u^2\,du}{(u^2+1)^2}. \tag{3-22}$$

After substitution of Equation (3-22) into Equations (3-18*a*) and (3-19), the corresponding current distribution and the field along the y-axis are respectively

$$I(v) = \frac{4}{\pi^2}\int_{-\infty}^{\infty} \frac{\sqrt{(q^2-v^2)\,(v^2-p^2)}}{\sqrt{(u^2+p^2)\,(u^2+q^2)}}\left(\frac{1}{u^2+v^2}+\frac{1}{h^2-v^2}\right)\frac{u^2\,du}{(u^2+1)^2}, \tag{3-23}$$

$$B_x(0, y) = \begin{cases} -\dfrac{2\mu I_0}{\pi d}\displaystyle\int_{-\infty}^{\infty} \frac{\sqrt{(q^2-y^2)(p^2-y^2)}}{\sqrt{(u^2+q^2)(u^2+p^2)}}\left(\frac{1}{u^2+y^2}+\frac{1}{h^2-y^2}\right)\frac{u^2\,du}{(u^2+1)^2}, & 0 \le y < p, \\ 0, & p < y < q, \\ \dfrac{2\mu I_0}{\pi d}\displaystyle\int_{-\infty}^{\infty} \frac{\sqrt{(y^2-q^2)(y^2-p^2)}}{\sqrt{(u^2+q^2)(u^2+p^2)}}\left(\frac{1}{u^2+y^2}+\frac{1}{h^2-y^2}\right)\frac{u^2\,du}{(u^2+1)^2}, & y > q, \end{cases} \tag{3-24}$$

and the potential along the y-axis is

$$A(0, y) = \frac{\mu I_0}{2}\left[J \ln\frac{y+h}{|h-y|} + \int_p^q \ln\frac{y+v}{|y-v|}\,I(v)\,dv + \frac{2}{y+1}\right] - \phi(t). \tag{3-25}$$

Now define ϕ_1 as the flux between the photosphere and the filament, and ϕ_2 as the flux between the photosphere and the current sheet, then

$$\phi_1 = \frac{\mu I_0}{2}\left[J \ln\left(\frac{2h}{r} - 1\right) + \int_p^q \ln\frac{h - r + v}{h - r - v} I(v)\, dv - \frac{2(h-r)}{h-r+1}\right], \tag{3-26a}$$

$$\phi_2 = \frac{\mu I_0}{2}\left[J \ln\frac{h+p}{h-p} + \int_p^q \ln\frac{v+p}{v-p} I(v)\, dv - \frac{2p}{p+1}\right]. \tag{3-26b}$$

In fact, ϕ_1 represents the total flux which is transferred from the photosphere into the corona through the reconnection of field lines in the photosphere, while ϕ_2 represents the flux dissipated due to the reconnection in the corona.

The above solutions of the potential and the field along the y-axis are derived under the assumption that the filament radius is small compared to all other scale lengths, hence they are not exact. However, the errors are estimated by Forbes and Isenberg (1991) to be of the second order in the small parameter r/h.

CHAPTER 4

EVOLUTION OF THE EQUILIBRIA AND ERUPTION

This chapter discusses the equilibria determined from the solutions of the vector potential. The equilibria are evolved either by changing the photospheric boundary condition or by reconnecting the coronal field lines below the filament. Let us first look at some interesting limiting cases of the general solution.

Special Cases of Current Sheet Solution

Attached Current Sheet Limit (p = 0)

The attached current sheet problem previously considered by Forbes and Isenberg (1991) is a special case of the general solution for a detached current sheet. The solution for the detached current sheet reduces to the solution for attached current sheet in the limit p = 0, i.e., when the bottom end of the current sheet attaches itself to the boundary. By substituting p = 0 into Equations (3-21a) and (3-24) and then evaluating the integrals for $y > q$, one finds that

$$B_x(0, y) = \frac{\mu I_0}{d}\left\{\frac{J y}{h^2 - y^2}\frac{\sqrt{h^2 - q^2}}{\sqrt{y^2 - q^2}} + \frac{2y}{(y^2-1)^2}\left[1 - \frac{1}{\pi}\,\mathrm{tg}^{-1}\left(\frac{2q\sqrt{y^2-q^2}}{y^2-2q^2}\right)\right] - \right.$$
$$\left. - \frac{y}{\pi(y^2-1)\sqrt{y^2-q^2}}\left[2q + \frac{y^2-2q^2+1}{(y^2-1)\sqrt{q^2-1}}\ln\frac{q+\sqrt{q^2-1}}{q-\sqrt{q^2-1}}\right]\right\}, \qquad (4\text{-}1)$$

which is the same as Equation (29) in Forbes and Isenberg (1991) (except for the difference between MKS and cgs units). Similarly, solutions for the potential, flux, etc.,

are identical with the relevant results in their paper in the limit $p = 0$. Therefore, the Forbes and Isenberg (1991) result is indeed a special case ($p = 0$ limit) of detached current sheet solution. The corresponding discussion and conclusion in their work may be applied appropriately to the problem if the attached limit is considered.

Zero Current Sheet Limit ($q = p$)

In the case in which a current sheet reduces to an '*x*' type neutral point occurring between the filament and the photosphere, the solution for the detached current sheet reduces to Equations (3-10) to (3-12). This special limit of the solution will be referred as the 'vacuum solution' in the remaining part of this chapter, because the field configuration is just like a wire (filament) immersed in a vacuum, with foot points of the field lines being tied in the photospheric boundary. Applying the condition that the magnetic field is zero at the neutral point ($y = p = q$) to Equation (3-11) leads to

$$Jh = (h^2 - p^2)/(p+1)^2, \tag{4-2}$$

which may be combined with the equilibrium condition to determine the position of the neutral point.

Evolution of the Filament Equilibria

The equilibria of the filament can be determined by finding the positions where the force on the filament is zero, as indicated by Equation (2-10). In general, Equation (2-10) is satisfied by substituting Equation (2-12) into Equation (3-9b). That is

$$\frac{1}{2}\frac{J}{h+y} - \frac{1}{(y+1)^2} + \int_p^q \frac{I(v)v\,dv}{v^2 - y^2} = 0, \tag{4-3}$$

which gives the general equilibrium condition for the filament.

Equilibria of the Filament ('Vacuum' Case)

In the 'vacuum' case, the equilibria of the filament can be obtained by substituting $I(v) = 0$ into Equation (4-3) and taking the limit $y \to h$. Hence

$$J = 4h/(h+1)^2. \tag{4-4}$$

The equilibria occur at

$$h = (2 - J - 2\sqrt{1-J})/J. \tag{4-5}$$

The position of the neutral point can be found by substituting Equation (4-4) into Equation (4-2) and then solving the obtained equation for p. That is

$$p = \frac{h(h+3)(h-1)}{(h+1)\sqrt{(h+1)^2 + 4(h^2-1)} + 4h}. \tag{4-6}$$

Since $p = 0$ when $h = 1$, the neutral point appears between the filament and the photosphere only if $h > 1$. Now the total reconnected flux ϕ_1 and the flux between the current sheet (i.e., the neutral point) and the photosphere, ϕ_2, can be expressed as the functions of the filament height, h, only. For $h \geq 1$,

$$\phi_1 = \mu I_0 \left[\frac{2h}{(h+1)^2} \ln\left(\frac{2h}{r} - 1\right) - \frac{h-r}{h-r+1} \right], \qquad h > r, \tag{4-7a}$$

$$\phi_2 = \frac{\mu I_0 h}{(h+1)^2} \left[4 \ln\left(\frac{1}{2} + \sqrt{\frac{1}{4} + \frac{h-1}{h+1}}\right) - \frac{(h-1)(h+3)}{h + \sqrt{1 + 4(h-1)/(h+1)}} \right], \tag{4-7b}$$

where Equations (4-4) and (4-6) have been used in the derivation. A schematic diagram of the field configuration with a neutral point appeared between the filament and the photosphere is shown in Figure 8.

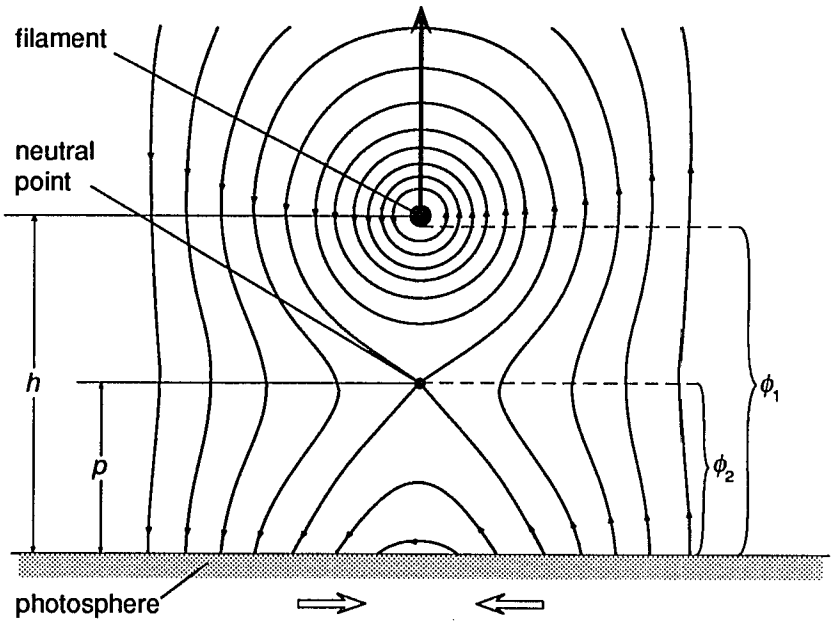

Fig. 8. A schematic diagram of field lines for 'vacuum' solution. The filament motion is indicated by the thick solid arrow, while plasma motion below the photosphere is indicated by the hollow arrows.

If we define $\phi_2 \equiv 0$ when the neutral point is below the photosphere ($p < 0$ case), then, for $h < 1$,

$$\phi_1 = \mu I_0 \left[\frac{2h}{(h+1)^2} \ln \left(\frac{2h}{r} - 1 \right) - \frac{h-r}{h-r+1} \right], \qquad h > r, \tag{4-8a}$$

$$\phi_2 = 0. \tag{4-8b}$$

A 3-D curve is defined by Equations (4-7) and (4-8) in the (h, ϕ_1, ϕ_2) space, with the flux normalized by μI_0, as shown in Figure 9. The curve has a turning point O at which ϕ_1 reaches its maximum value. The position of the turning point O, h_c, can be found by taking the derivatives to h at both sides of Equation (4-7a) and then setting $d\phi_1/dh = 0$, i.e.,

$$2(h-1) \ln [(2h/r - 1)] = (h+1) [4h/(2h-r) - (h+1)^2 /(h+1-r)^2]. \tag{4-9}$$

When $r \to 0$, $h \to 1$. Thus, for small filament radius ($r < 0.01$), we have approximately

$$2(h-1) \ln(2h/r) = h + 1.$$

The solution of Equation (4-9), $h = h_c(r)$, can be substituted into Equation (4-7a) to get

$$\phi_{1max} = \mu I_0 \left\{ \frac{h_c}{h_c^2 - 1} \left[\frac{4h_c}{2h_c - r} - \frac{(h_c+1)^2}{(h_c - r + 1)^2} \right] - \frac{h_c - r}{h_c - r + 1} \right\}, \tag{4-10}$$

which is a function of the filament radius, r. Similarly, by substituting the turning point position, h_c, into Equations (4-4), (4-6) and (4-7b), the corresponding values for J, p, and ϕ_2, can be obtained respectively.

When h (filament height) approaches infinity, J (filament current) approaches zero. The filament is no longer affected by photospheric field as it reaches the equilibrium at infinity, no matter what the values of ϕ_1 and ϕ_2 might be.

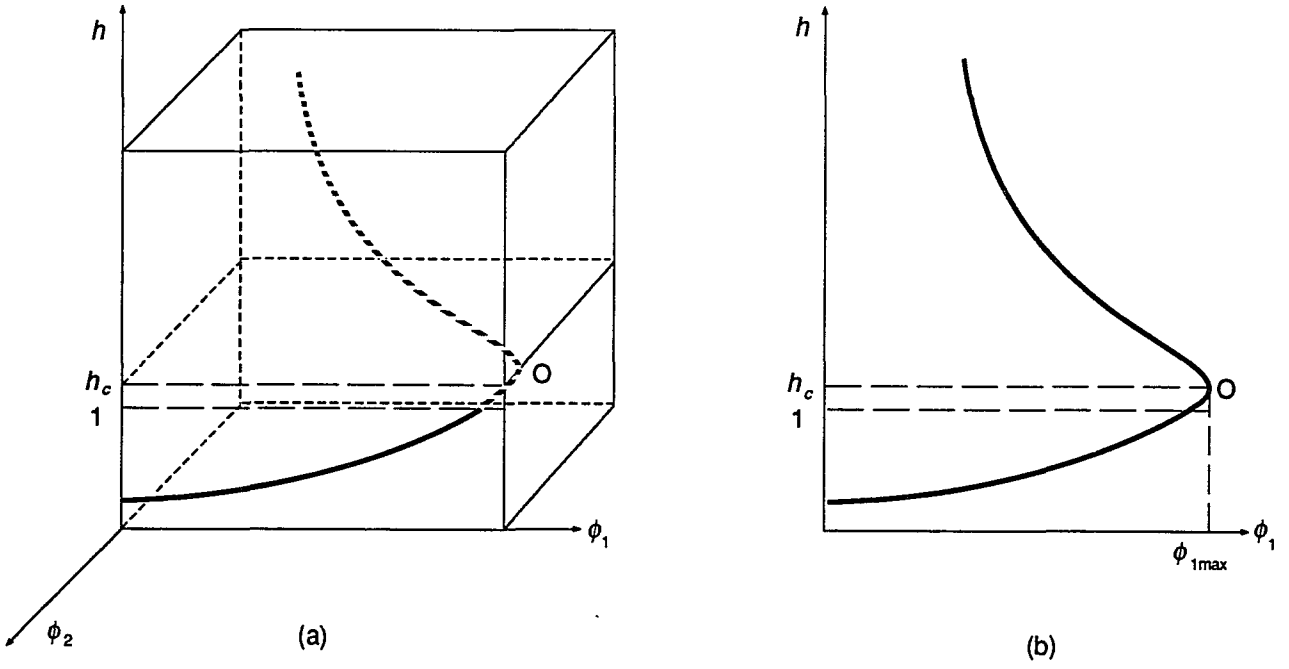

Fig. 9. A schematic diagram of the 'vacuum' solution: (a) in the 3-D (h, ϕ_1, ϕ_2) space, the thick solid (dashed) curve represents the part of the solution in (out of) the h-ϕ_1 plane; (b) its projection on the h-ϕ_1 plane. The point O is the turning point at which $\phi_1 = \phi_{1max}$.

Equilibria of the Filament (with Current Sheet)

After substituting Equation (3-23) into Equation (4-3) and evaluating the integral of the last term on the RHS of Equation (4-3), we obtain the equilibria for the filament, with a current sheet formed below it. That is

$$J\left(\frac{2h^2}{h^2-q^2}+\frac{h^2+p^2}{h^2-p^2}\right)=\frac{2}{\pi}\int_{-\infty}^{\infty}\frac{\sqrt{(h^2-q^2)\,(h^2-p^2)}}{\sqrt{(u^2+q^2)\,(u^2+p^2)}}\,\frac{4h}{h^2+u^2}\,\frac{u^2\,du}{(u^2+1)^2}, \qquad (4\text{-}11)$$

where Equation (3-21a) has been used.

In general, J, q, p, and $I(v)$ depend on h, r and ϕ_1. If we set ϕ_1 and r as constants, then Equations (3-26a) and (4-11) define two functions $p(h)$ and $q(h)$ implicitly through

$$V(h,p,q)=J\ln\left(\frac{2h}{r}-1\right)+\int_p^q \ln\frac{h-r+v}{h-r-v}\,I(v)\,dv-\frac{2(h-r)}{h-r+1}-\frac{2\phi_1}{\mu I_0}=0, \qquad (4\text{-}12a)$$

$$W(h,p,q)=J\left(\frac{2h^2}{h^2-q^2}+\frac{h^2+p^2}{h^2-p^2}\right)-\frac{2}{\pi}\int_{-\infty}^{\infty}\frac{\sqrt{(h^2-q^2)\,(h^2-p^2)}}{\sqrt{(u^2+q^2)\,(u^2+p^2)}}\,\frac{4h}{h^2+u^2}\,\frac{u^2\,du}{(u^2+1)^2}=0, \qquad (4\text{-}12b)$$

where J and $I(v)$ are given by Equations (3-21a) and (3-23), respectively. Therefore, the length of the current sheet, $q-p$, the filament current, J, and the current distribution in the sheet, $I(v)$, are expressed as the functions of the filament height, h, respectively, with ϕ_1 and r as the parameters.

As mentioned previously, the 'vacuum' solution given by Equations (4-7) and (4-8) defines a three dimensional equilibrium curve in the (h, ϕ_1, ϕ_2) space. More generally, the solution with the detached current sheet, given by Equations (3-21a), (3-23), (3-26) and (4-11), defines a three dimensional equilibrium surface in the (h, ϕ_1, ϕ_2) space. The special case of the 'vacuum' solution (the 3-D curve) lies on this surface and serves as a

boundary, while the attached current sheet solution obtained by Forbes and Isenberg (1991) is the intersection line of the equilibrium surface with the h-ϕ_1 plane.

Evolution of the Equilibria

The current filament stays in magnetohydrostatic equilibrium if the magnetic compression of field lines between the filament and the photosphere is balanced by the magnetic tension of the field lines anchored in the photosphere but passing over the top of the filament. The quasi-static evolution of the equilibria is caused by the gradual reconnection of photospheric field lines below the filament. As the flux is transferred from the photosphere into the corona, magnetic energy is stored in the corona. In this way the filament is quasi-statically driven upwards as the magnetic compression increases, until it reaches a critical point where the magnetohydrostatic equilibrium becomes unstable. Eventually an eruption may occur during which the filament is rapidly ejected upwards.

Keeping in mind the basic ideas above, the evolution of the equilibria is determined as follows: Prior to the formation of the current sheet, the evolution is prescribed by the 'vacuum' solution, i.e., Equations (4-8) and (4-7) for $h < 1$ and $h \geq 1$ cases, respectively. The height of the filament is determined by the total reconnected flux, ϕ_1. While after the formation of the current sheet, the evolution is governed by the more general solution given by Equations (3-21a), (3-26) and (4-11).

Now an important question arises: where is the formation point of the current sheet? This point serves as a critical point in the evolution of the equilibria, and two different solutions will be used to describe respectively the evolution before and after this point. According to the discussion in Chap. 2, a current sheet may be formed about an x-type neutral point in response to changes in the surrounding magnetic field when a

magnetohydrostatic equilibrium becomes unstable. It is obvious now that a current sheet can only develop in the corona when $h \geq 1$, since for $h < 1$, the neutral point stays below the photosphere. For $h > 1$, the 'vacuum' solution shows that the neutral point occurs above photospheric boundary (see Figure 8), with its position given by Equation (4-6). In an ideal MHD model, a current sheet would tend to develop immediately after the neutral point occurs. If reconnection in the corona is prohibited, a current sheet with one end attached to the photosphere will be formed below the filament, as happens in the solutions of Forbes and Isenberg (1991). However, in our model, the reconnection in the corona is allowed. Considering that the reconnection time scale, τ_r, is much smaller than the quasi-static evolution time scale, τ_p, no current sheet will be formed during the quasi-static evolution, because the reconnection will immediately dissipate any current sheet. In other words, the current sheet will not be formed in the storage phase.

So it is reasonable to think that the current sheet in the model starts to form spontaneously with the loss of magnetohydrostatic equilibrium and develops during the eruptive phase. Actually, the formation point of the current sheet is the turning point of the 'vacuum' solution (point O in Figure 9) because this turning point is in fact the critical point in the evolution of the equilibrium. This can be deduced as follows: In the quasi-static storage phase, the filament evolves through the stable equilibrium curve (the 'vacuum' solution) until the total reconnected flux, ϕ_1, reaches its maximum value at the point O, as illustrated in Figure 9b. The flux ϕ_1 corresponds to $\phi(t)$, which has been defined in Equations (2-15) and (2-16) as the flux transported by photospheric flow from $x = \pm\infty$, and therefore there should be no limit on its value. In other words, ϕ_{1max} cannot be the upper limit of ϕ_1, either from physical or mathematical considerations. Notice that there is a 'vacuum' equilibrium state at infinity ($h = \infty$) where ϕ_1 could take any value. Thus, it is clear that ϕ_1 has multiple values at the

turning point O where no nearby stable 'vacuum' equilibria are available. Consequently, we see that the point O is indeed the critical point at which the storage phase of the evolution ends. The coronal current system can no longer respond to the quasi-static changes in the photosphere through quasi-static evolution. Any further change, no matter how small it might be, will cause a loss of equilibrium, and the quasi-static evolution will be replaced by the dynamic evolution—the eruption. If the reconnection could occur freely in the corona, i.e., $\tau_A >> \tau_r$, then no current sheet would ever be formed, and the filament would be ejected right up to infinity. However, this is not the case in an ideal-MHD model. In an ideal-MHD model $\tau_r \rightarrow \infty$, and no reconnection occurs in the corona. Without reconnection, a current sheet develops rapidly during the eruption, and the tension force grows so strong that the filament's upward motion is stopped long before the filament reaches ∞. Such an eruption, caused by the loss of ideal-MHD equilibrium, corresponds to the impulsive phase of the eruptive flares. In a realistic plasma like the corona, τ_r will be finite, but it may still be much greater than τ_A, and thus the ideal-MHD solution may be a good approximation during the jump in this case. However, it is also possible that $\tau_r \gtrsim \tau_A$, in which case significant reconnection would occur during the jump. Here we will assume that this is not the case.

Preflare phase

The above discussions have an important implication which is closely related to the preflare phase of the eruptive solar flares. According to the discussions in the last section, an x-type neutral point appears between the filament and the photosphere during the late stage of the quasi-static evolution. Because the reconnection in the corona is so fast compared with quasi-static evolution ($\tau_r << \tau_p$), no current sheet is formed until the evolution of the system reaches the critical point. The evolution in the

period prior to the eruption, starting after the neutral point appears and ending when the system reaches the critical point, can be identified with the preflare phase, and the evolution of the system during the preflare phase is governed by the 'vacuum' solution.

When the system evolves along the equilibrium curve, the force acting on the filament is zero, and no work is done due to the displacement of the filament. The change in magnetic energy is due to the variation of the flux in the circuit only (Forbes and Isenberg, 1991). That is

$$\Delta W = \int_C \frac{\partial W}{\partial \phi_1} d\phi_1 = \int_C I_f [h(\phi_1), \phi_1] \, d\phi_1 = \pi I_0 \int_C J(h) \frac{\partial \phi_1}{\partial h} dh, \tag{4-13}$$

where C is the path of the integration—the 'vacuum' equilibrium curve. Substitution of the 'vacuum' solutions, i.e., Equations (4-4) and (4-7a), into Equation (4-13) gives

$$\Delta W_{pre} = \pi \mu I_0^2 [K^*(h_c) - K^*(1)], \tag{4-14a}$$

$$W_0 = \pi \mu I_0^2 [K^*(\infty) - K^*(1)], \tag{4-14b}$$

$$W_c = \pi \mu I_0^2 [K^*(\infty) - K^*(h_c)], \tag{4-14c}$$

where

$$K^*(h) = \int \frac{4h}{(h+1)^4} \left[\frac{4h}{2h-r} - \frac{(h+1)^2}{(h+1-r)^2} - 2\frac{h-1}{h+1} \ln \left(\frac{2h}{r} - 1 \right) \right] dh, \tag{4-15}$$

and W_0 is the stored magnetic energy when the neutral point appears on the photosphere boundary ($p = 0$), W_c is the stored energy when the evolution of the system reaches the critical point, h_c is the height of the filament corresponding to the critical point given by the solution of Equation (4-9). The energy change during the preflare phase is $\Delta W_{pre} = W_0 - W_e$. The integral in Equation (4-15) can be evaluated to obtain

$$K^*(h) = \frac{4h^2}{(h+1)^4}\ln\left(\frac{2h}{r}-1\right)+\frac{4}{r^2}\left[\left(\frac{2}{r}-1\right)\ln\frac{h+1}{h+1-r}-\frac{1}{h+1}-\frac{1-r}{h+1-r}\right]+$$

$$+\frac{8}{2+r}\left[\frac{1}{3}\frac{1}{(h+1)^3}-\frac{1+r}{2+r}\frac{1}{(h+1)^2}+\frac{r^2}{(2+r)^2}\frac{1}{h+1}-\frac{2r^2}{(2+r)^3}\ln\frac{h+1}{h-r/2}\right], \quad (4\text{-}16)$$

where $K^*(\infty) = 0$. For small filament radius (say, $r < 0.01$), we have approximately

$$K^*(h) = \frac{4h^2}{(h+1)^4}\ln\left(\frac{2h}{r}\right). \quad (4\text{-}17)$$

Eruption and the Formation of the Current Sheet

General Eruption Analysis

The 'vacuum' solution below the critical point O (see the 3-D curve in Figure 9a) represents the lower stable equilibrium branch of the evolution. The upper stable equilibrium branch is represented by the solution with the detached current sheet. Catastrophe behavior occurs if the two branches exhibit multiplicity at $\phi_1 = \phi_{1max}$, as illustrated in Figure 10a. However, if the upper branch of the equilibrium curve is well connected to the lower branch, as shown in Figure 10b, then the transition from the lower to the upper equilibrium will occur smoothly and continuously. To determine the catastrophe behavior, in general we need to calculate the equilibrium curve $h = h(\phi_1)$ by solving Equation (3-26a) and the associated equations, as we did in the 'vacuum' case. However, the better and simpler way to study the catastrophe behavior is to use the condition that the eruptive phase is a transient process during which the flux in the corona is constant. The analysis will be carried out as follows:

Since the previous discussion shows that $\phi_1 = \phi_{1max}$ when the eruption starts, then, by substituting $\phi_1 = \phi_{1max}$ into Equation (4-12a) and solving Equations (4-12) with Equations (3-21a) and (3-23), we obtain $J(h)$, $q(h)$, $p(h)$ and $I(v,h)$ during the eruptive

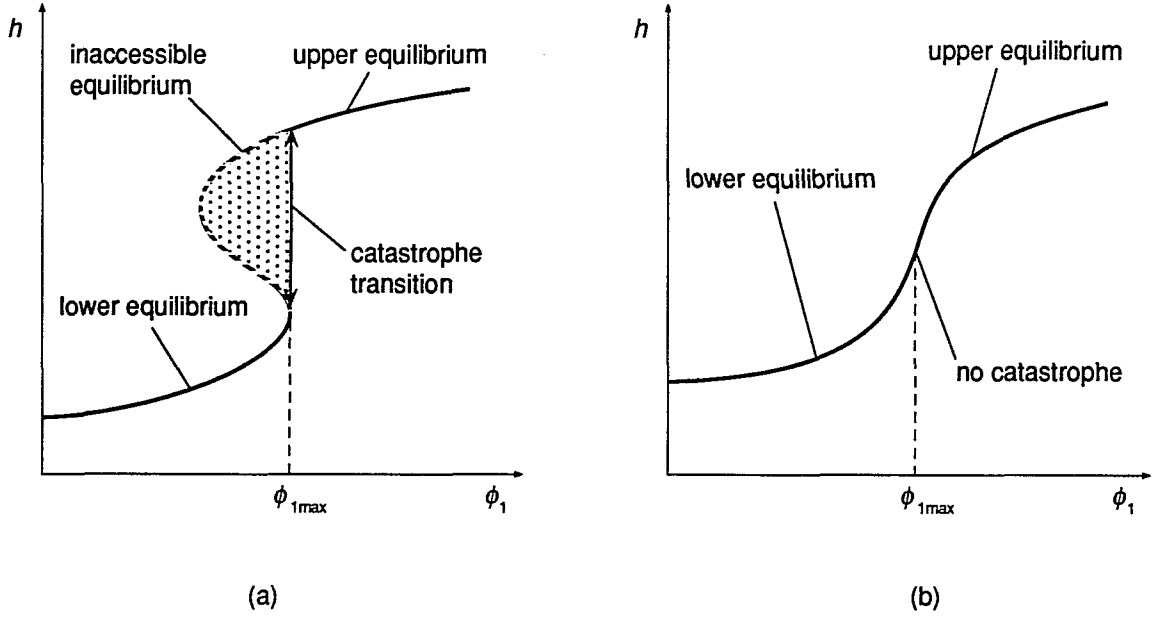

Fig. 10. Schematic diagram of the projection of the filament equilibria onto the h–ϕ_1 plane: (a) with catastrophe; (b) with no catastrophe.

phase, respectively. The next step is to substitute the above results into Equation (3-26b) so that the equilibrium curve $h = h(\phi_2)$ is determined for the detached current sheet solution, with $\phi_1 = \phi_{1max}$. As mentioned previously, the detached current sheet solution in general defines a 3-D equilibrium surface in the (h, ϕ_1, ϕ_2) space, and the equilibrium curve $h(\phi_2)$ is just the intersection line of the 3-D surface with the $\phi_1 = \phi_{1max}$ plane. If $h(\phi_2)$ exhibits multiplicity at $\phi_2 = \phi_{2c}$, where ϕ_{2c} is the value of ϕ_2 at the critical point O ($h = h_c$ in Equation (4-7b)), then catastrophe behavior exists. The eruption due to the catastrophic loss of ideal-MHD equilibrium can be determine by finding h_u, the upper equilibrium position, where again $\phi_2 = \phi_{2c}$. Once h_u is known, the length of the current sheet and other physical quantities are determined accordingly. For instance, the energy released during the eruption (i.e., the impulsive phase) can be calculated by evaluating the integral on the RHS of Equation (4-13), where the path C is the equilibrium curve determined by the detached current sheet solution (from $h = h_c$ to $h = h_u$). In Figure 11 the stored magnetic energy of the system as the function of the filament height is sketched for the fixed total flux ($\phi_1 = \phi_{1max}$), and the energy released during the eruption is also indicated.

The eruption analysis method described above is analogous to the method used by Forbes and Isenberg(1991). The only difference is that in their analysis $\phi_2 = 0$, instead of $\phi_1 = \phi_{1max}$, and they determined $h(\phi_1)$, instead of $h(\phi_2)$ (in their attached current sheet model ϕ_1 is denoted as ϕ since $\phi_2 \equiv 0$). The results of their catastrophe behavior analysis is presented in Figure 4 of Forbes and Isenberg (1991), which is sketched in Figure 12. As an example, we also plot in Figure 13 the magnetic field configurations at various stages in the evolution described by the attached current sheet solution (Forbes and Isenberg, 1991). Although the attached current sheet case is only a special limiting case of the more general detached cases, the field configurations shown in Figure 13

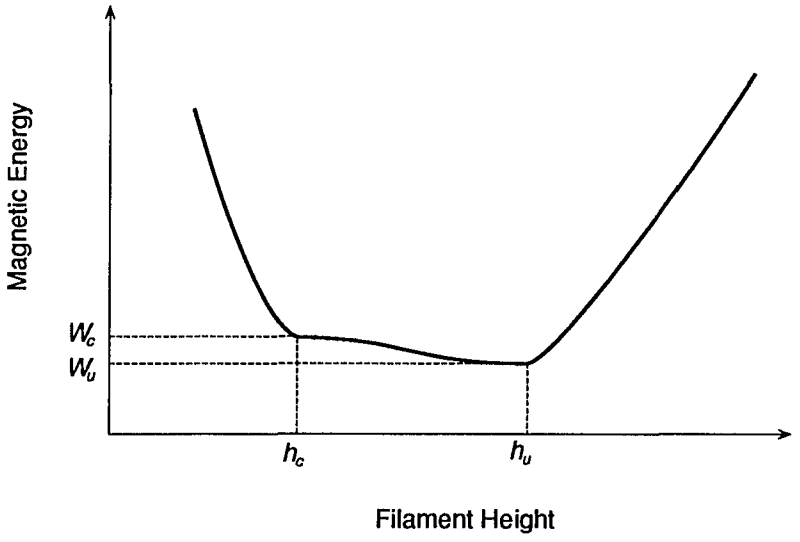

Fig. 11. A schematic diagram of the magnetic energy of the system as the function of the filament height for fixed flux ($\phi_1 = \phi_{1max}$). The energy released during the eruption is: $W_u - W_c$ (if reconnection in the corona is allowed).

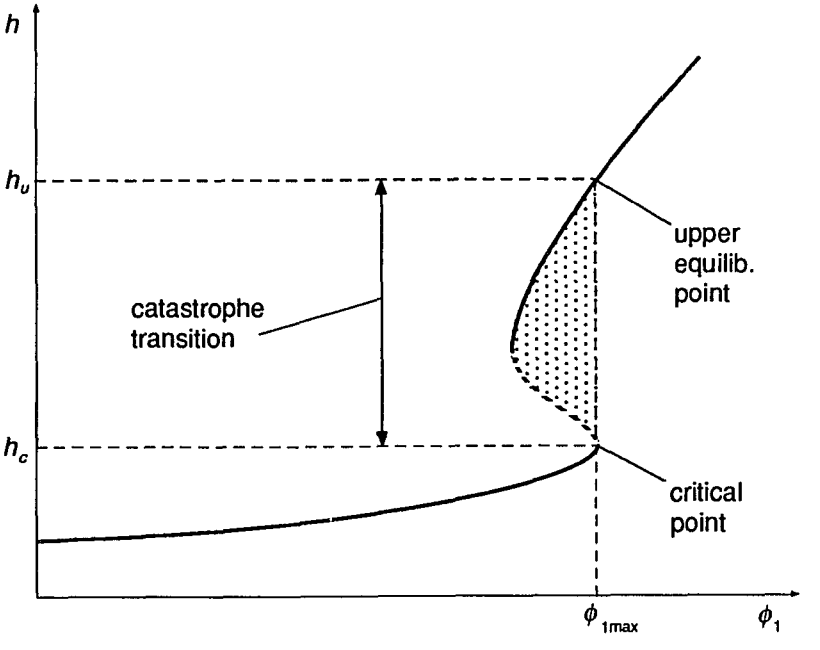

Fig. 12. A schematic drawing of the equilibria in the attached current sheet model (Forbes and Isenberg, 1991) when catastrophe behavior is present. The dashed part of the equilibrium curve is unstable, and the shaded region is inaccessible.

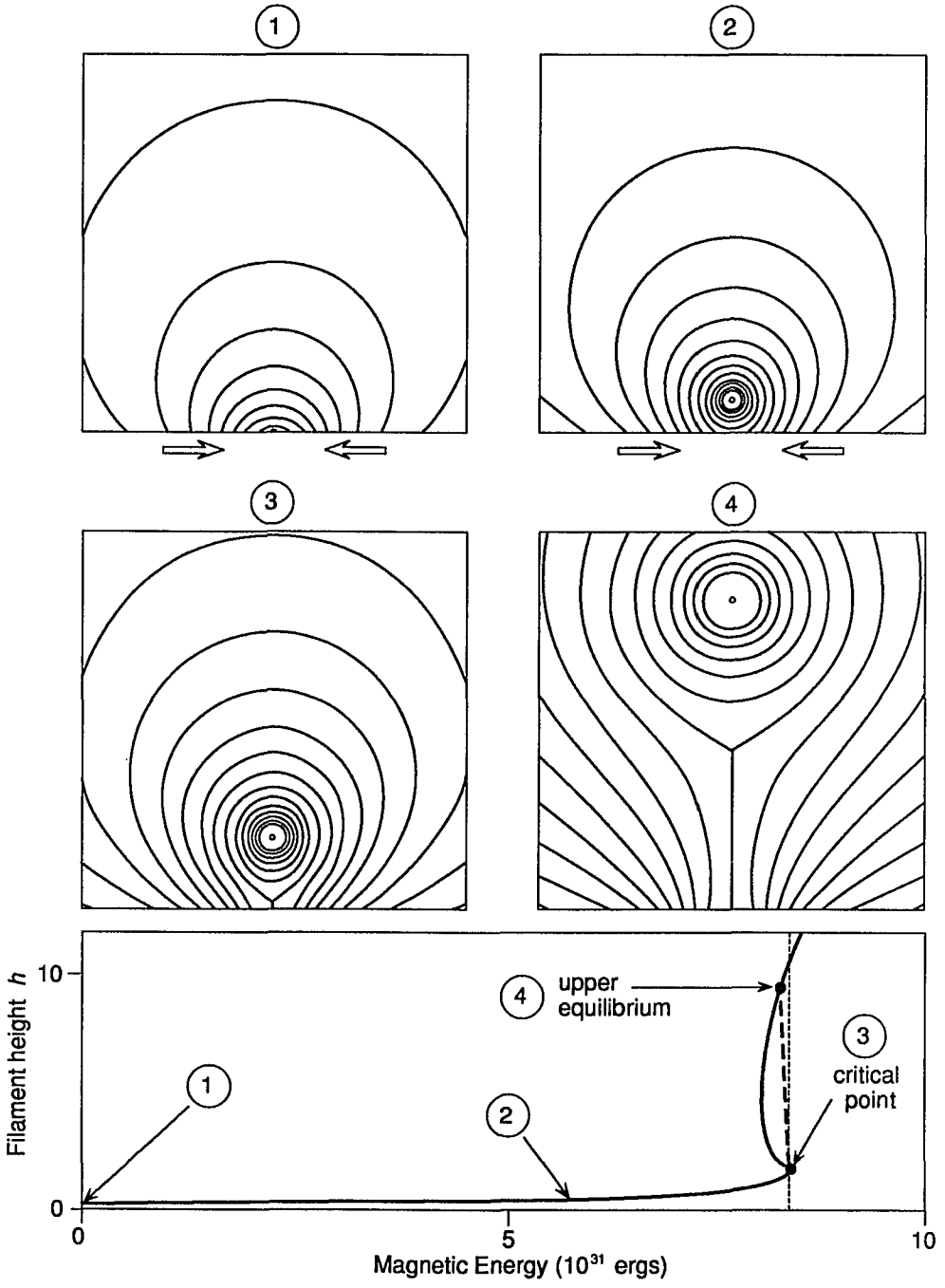

Fig. 13. Magnetic field configurations at various stages in the attached current sheet solution (after Forbes and Isenberg, 1991). A catastrophic loss of equilibrium occurs when the evolution reaches the critical point at 3. The equilibrium filament height is sketched as a function of the stored magnetic energy in the bottom panel. The thick dashed line is the expected filament trajectory during the ideal-MHD jump (the deviation of the trajectory from the vertical line has been exaggerated for illustration).

still illustrate the basic picture of the variation of the field configuration during the evolution. Figure 14 shows schematically the equilibrium filament height as the function of the stored magnetic energy in the detached current sheet model. Also shown are the corresponding curves for the attached model.

Small Current Sheet Expansion Analysis

The general solution for the equilibria with a detached current sheet involves complete elliptic integrals, and a system of 5 coupled transcendental equations. Even if elliptic integrals were not present, the system of transcendental equations is sufficient to rule out the possibility of an analytical solution. Thus only a numerical solution of the full system is possible. Such a numerical solution was previously done by Forbes and Isenberg (1991) for the attached current sheet case, but their numerical method is not yet efficient enough to handle the additional complication of elliptic integrals. However, as we will see, a simple expansion for small current sheets can provide some significant information about the effect of the current sheet and enhance our understanding of the solution.

Let $\varepsilon_0 = q - p$ be the small parameter of the expansion, where $(q-p)/q << 1$ has been assumed for the small current sheet. If we define $s^2 = (p^2 + q^2)/2$ and $s^* = (p+q)/2$, then $s^* = s + o(\varepsilon_0^2)$. By substituting ε_0, s and s^* into Equations (3-21a), (3-23), (3-26) and (4-11) and then expanding Equations (3-26), we obtain

$$\phi_1 = \phi_{10} + \varepsilon^2 \frac{h^2 - s^2}{2s} \ln \frac{h+s-r}{h-s-r} + o(\varepsilon^4), \qquad (4\text{-}18a)$$

$$\phi_2 = \phi_{20} + \varepsilon^2 \frac{h^2 - s^2}{2s} \ln \frac{s+p}{s-p} + o(\varepsilon^4), \qquad (4\text{-}18b)$$

where ϕ_{10} and ϕ_{20} are the 'vacuum' values of ϕ_1 and ϕ_2 given by Equations (4-7),and

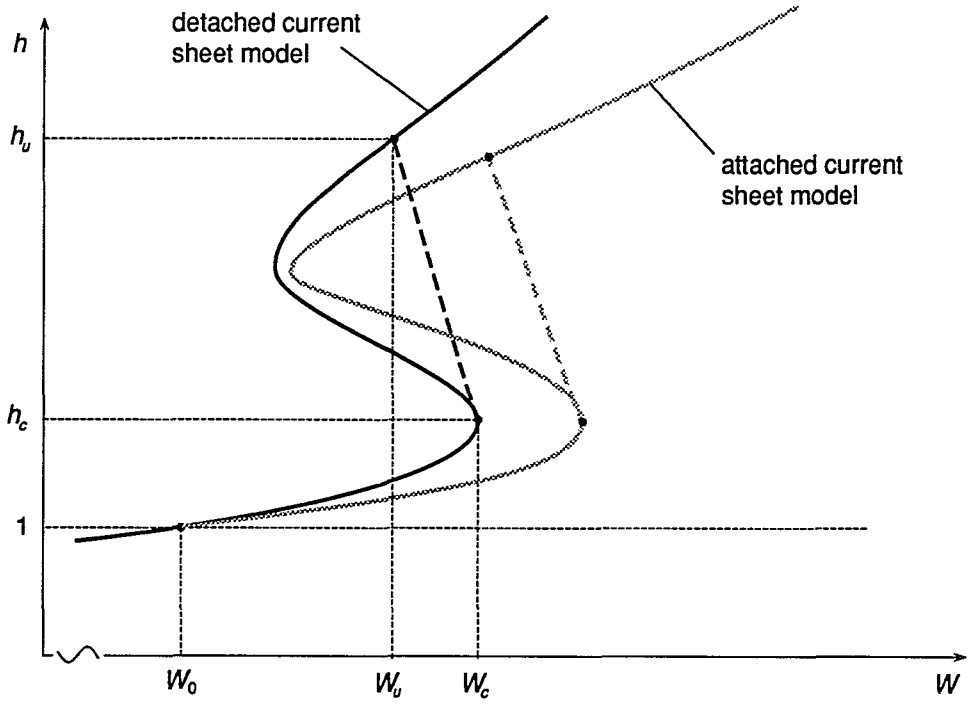

Fig. 14. A schematic diagram of the equilibrium filament height as the function of the stored magnetic energy in the detached current sheet model (dark). The dashed line represents the expected filament trajectory during the catastrophic eruption. The curves for the corresponding attached current sheet model (light shaded) is also sketched for comparison.

$$\varepsilon^2 = \frac{\varepsilon_0^2}{2}\left(\frac{s}{h^2-s^2}\right)^2 \frac{1}{(s+1)^2}\left[1+\frac{h^2-s^2}{s(s+1)}\right]$$

The expansions (4-18) lack the first order terms because the two ends of the current sheet, i.e., points p and q, are symmetric to the neutral point. For small current sheets, $s \approx s^*$, and thus

$$\varepsilon_0 = q-p = 2(s^*-p) \approx 2(s-p),$$

where s is given by Equation (4-6), i.e.,

$$s = \frac{h(h+3)(h-1)}{(h+1)\sqrt{(h+1)^2+4(h^2-1)}+4h},$$

For small current sheets $s \approx s^*$ is just the the position of the neutral point, and the approximate solution, $h = h(\phi_1, \phi_2)$, for small detached current sheet can be solved from Equations (4-18) by using the above relations to eliminate p, ε, and s. To the first order, the solution is basically the same as the 'vacuum' solution. Thus, the behavior and properties of the small current sheet solution are essentially equivalent to the solutions obtained previously by Martens and Kuin (1989), and Priest and Forbes (1990), who used a line current to represent the small current sheet.

Although we are unable to calculate the full solution of the general detached current sheet analytically, we can nevertheless get basic ideas about the overall behavior of the solution from the expansion and plot the full solution schematically. Equations (4-18) indicate that the present of the current sheet increases the total amount of flux that can be stored in the corona ($\phi_1 > \phi_{10}$, $\phi_{10} > 0$) while decreasing the coronal flux below the original x-line ($|\phi_2| < |\phi_{20}|$, $\phi_{20} < 0$). Since

$$\ln[(s+p)/(s-p)] > \ln[(h+s-r)/(h-s-r)],$$

we can see that the effect of the current sheet on ϕ_2 in greater than that on ϕ_1, when the length of the current sheet is small.

About Catastrophe Behavior

Based on the properties above and our knowledge of the two special limiting cases of the detached current sheet solution, namely the 'vacuum' solution and the attached current sheet solution, we are able to determine the general behavior of the overall solution in the 3-D space (h, ϕ_1, ϕ_2), as shown in Figure 15. The thick solid curve (in the h-ϕ_1 plane) is the attached current sheet solution obtained by Forbes and Isenberg (1991), while the dashed 3-D curve represents the 'vacuum' solution . The 3-D surface between the two curves is the equilibrium surface defined by Equations (3-26) and the associated equations. The evolution of the equilibria depends crucially on the rate of the reconnection in the corona. If the reconnection in the corona is prohibited, i.e., $\tau_r >> \tau_p$, then the equilibrium curve is the attached current sheet solution; on the other hand, if the reconnection occurs freely in the corona, i.e., $\tau_r << \tau_A$, then no current sheet can be formed and the equilibrium curve is the 'vacuum' solution. Under the more realistic ordering, $\tau_p >> \tau_r >> \tau_A$, a detached current sheet is formed and the equilibrium curve is somewhere between the two limiting cases discussed above. According to Figure 15 and Equations (4-7) to (4-10), the location and the shape of the equilibrium curve depend on the filament radius, r. If the equilibrium curve exhibits multiplicity at the critical point, then the filament will be ejected upwards by a catastrophic loss of ideal-MHD equilibrium.

An important result obtained by Forbes and Isenberg (1991) is that the occurrence of the catastrophic loss of equilibrium depends crucially on the radius of the filament. In their analysis the catastrophe behavior disappears when the filament radius exceeds a

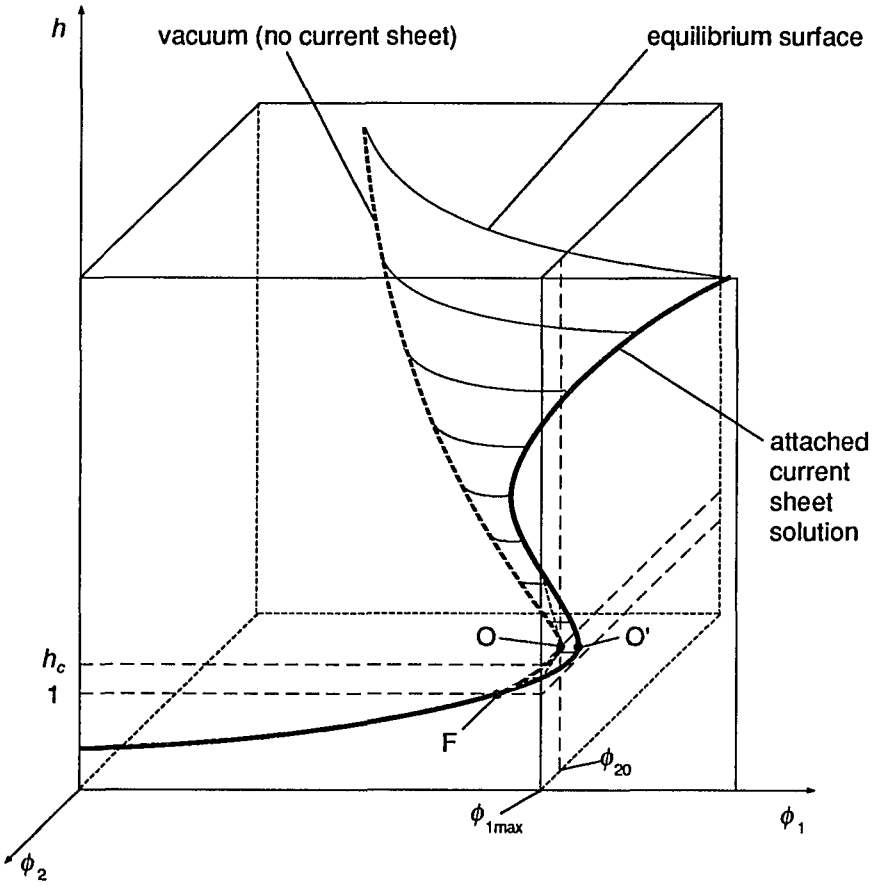

Fig. 15. A schematic diagram of the equilibrium surface defined by the detached current sheet solution. Point O is both the critical point and the sheet formation point for the detached current sheet model, while points O' and F are the critical point and the sheet formation point for the attached model (Forbes & Isenberg, 1991), respectively.

specific value (10^{-3} times the length scale of the photospheric field). Other studies of CME's (Démoulin & Priest, 1988; Anzer & Ballester 1990) have led to similar results.

Since the attached current sheet model by Forbes and Isenberg (1991) represents a special limiting case of our detached current sheet model, we would expect that the above result is generally true for our generalized model. Indeed, by examining Figure 15 carefully, one can tell that the catastrophe behavior exists when the filament radius is sufficiently small. In Figure 15, three points O, O' and F are separated from each other when the filament radius $r \neq 0$, but they approach each other as $r \rightarrow 0$ and become one identical point when $r = 0$. Since catastrophe occurs in the attached current sheet case for small filament radius, the continuity of the equilibrium surface ensures that catastrophe behavior also occurs in the detached case, provided that the filament radius is so small that the two equilibrium curves (attached and detached) are very close and behave similarly. The trajectories of the filament during the overall evolution is sketched in Figure 16a in which the catastrophe eruption (ideal-MHD jump) is indicated by thick dashed curve. After the catastrophic eruption, the system undergoes the third stage—a reconnection jump which is a non-ideal process during which the current sheet is dissipated by fast reconnection and magnetic energy is released as the filament is ejected upwards to infinity. The time scale of the reconnection jump is comparable to τ_r and much faster than the quasi-static time scale τ_p, so that during the reconnection jump the total flux (in the corona) ϕ_1 is constant.

In the detached current sheet model, the critical radius of the filament, r_c, can be determined by investigating the behavior of the equilibrium curve near the critical point, O. According to the previous discussion, the equilibrium curve $h = h(\phi_2)$ which lies on the $\phi_1 = \phi_{1max}$ plane of the 3-D (h, ϕ_1, ϕ_2) space can be determined by solving Equations (4-12) and (3-26b) in association with Equations (3-21a) and (3-23). When the filament radius r satisfies $r < r_c$ so that catastrophe behavior occurs, the shape of the

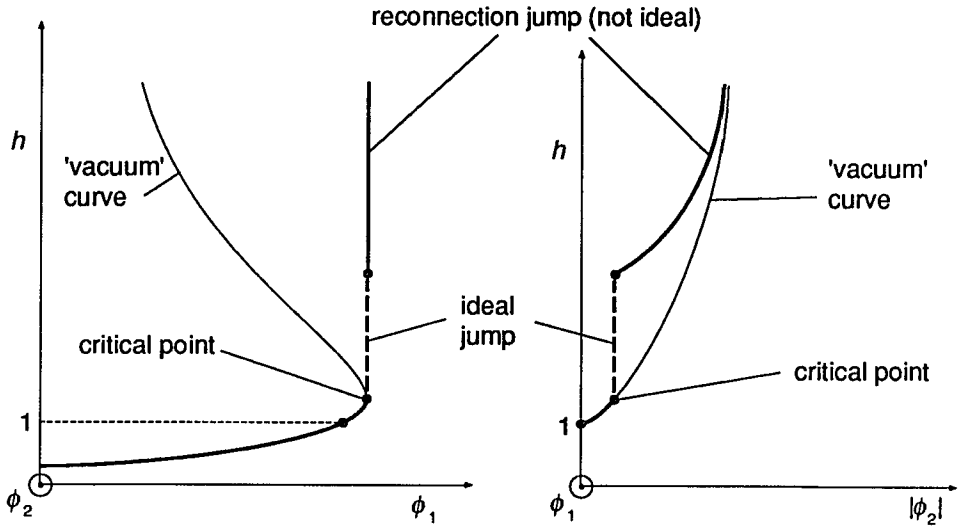

(a) $0 < r < r_c$, with catastrophe

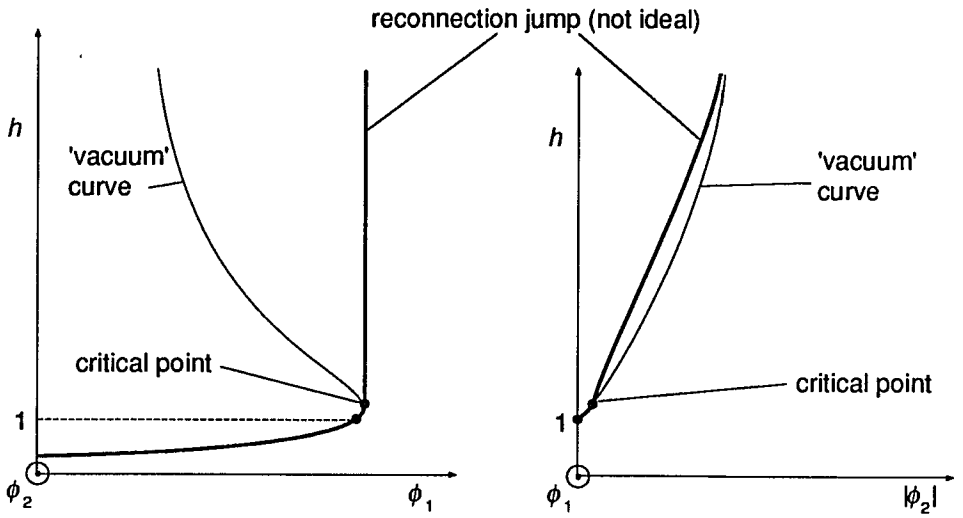

(b) $r > r_c$, with no catastrophe

Fig. 16. Schematic diagrams of 3-D curves projected onto the h-ϕ_1 plane and the h-ϕ_2 plane. The curves show the trajectories of the filament during the evolution. In (a) the filament radius is smaller than the critical radius, and a catastrophic loss of ideal-MHD equilibrium occurs. In (b) the filament radius is greater than the critical radius for catastrophe, and only the reconnection jump occurs.

equilibrium curve $h(\phi_2)$ looks like an 'S' (e.g., Figure 12) in the (h, ϕ_2) plane, and $d\phi_2/dh = 0$ at the two turning points. The lower turning point is in fact the critical point $h = h_c$, which is a maximum-value point of the function $\phi_2(h)$, while the upper turning point which is on the unstable branch of the equilibrium curve is a minimum-value point of $\phi_2(h)$. As the filament radius increases, the two points move closer and eventually become one identical point —the inflection point—when $r = r_c$. For $r > r_c$, there is no catastrophe, and $d\phi_2/dh \neq 0$ at $h = h_c$. Therefore, when $r = r_c$,

$$d\phi_2/dh = 0, \qquad h = h_c, \tag{4-19a}$$

$$d^2\phi_2/dh^2 = 0, \qquad h = h_c, \tag{4-19b}$$

which are the conditions needed to determine the critical radius of the filament.

The physical interpretation of the specific filament radius required for catastrophe behavior is that there must be enough magnetic energy stored in the corona to trigger a catastrophic loss of ideal-MHD equilibrium. From Equations (4-9) and (4-10) we see that the total reconnected flux ϕ_{1max}, which corresponds to the total magnetic energy transferred from the photosphere to the corona prior to the eruption, increases as r decreases. Thus, from the view that the filament current is generated by photospheric reconnection, it is quite reasonable to expect the filament radius to be less than some critical value in order to maintain catastrophe behavior. In other words, the stored magnetic energy must exceeds some critical value, W_{c0}. This critical value of magnetic energy can be computed from Equation (4-14c) by setting $r = r_c$ in Equations (4-9) and (4-16) and substituting them into Equation (4-14c), i.e.,

$$W_{c0} = W_c(r = r_c). \tag{4-20}$$

The energy requirement $|W_c| > |W_{c0}|$ is equivalent to the radius requirement $r < r_c$ for maintaining catastrophe behavior. However, if the critical value of the filament radius

determined by condition (4-19) is too small, then the corresponding field strength at the surface of the filament would be extremely large. For instance, some 10^5 Gauss field is estimated to occur at the surface of a filament with the radius r of about 10^{-3} times the scale length of photospheric field (Forbes and Isenberg, 1991), which is not realistic.

In general, the critical value of the filament radius depends on the photospheric background field of a specific model and other factors such as the consideration of the state of the filament. Recently, Isenberg, Forbes and Démoulin (1992) have found that the critical value of the filament radius can be as large as 0.24 times the length scale of the photospheric field, if a submerged dipole is replaced by a quadrupole for the background field and the filament is compressible or force-free instead of incompressible. Since the effect of a current sheet is to hold the filament and stabilize the equilibrium, it is reasonable to expect the critical energy required for catastrophe in the detached current sheet case is less than that in the attached case, because no current sheet is formed before the eruption in detached case. In other words, the critical radius of the filament in the detached current sheet model should be larger than the critical radius of the filament in the corresponding attached case.

Evolution without Catastrophe

An interesting point worth considering is how the evolution of the system proceeds if no catastrophe occurs. This happens when the filament radius r is greater than the critical value r_c. Without catastrophe means that the system never losses ideal-MHD equilibrium. Instead, it undergoes a reconnection jump which is a resistive process (see Figure 16b). According to the previous discussion, the quasi-static evolution of the coronal system via the 'vacuum' equilibrium curve (lower branch of equilibrium) ends at the critical point O where the magnetohydrostatic equilibrium becomes unstable and a current sheet starts to develop. The evolution beyond the critical point O is no longer

quasi-static compared to the reconnection time scale, τ_r, because it has to be fast enough to allow the current sheet to develop slowly below the rising filament. The corresponding time scale for this evolution is on the order of the reconnection time scale τ_r. When the current sheet becomes long enough, a tearing-mode instability will eventually occur and lead to a relatively slow eruption.

The evolution without catastrophe behavior generally suggests that the system can not acquire enough energy for the catastrophe eruption before it reaches the critical point where the magnetohydrostatic equilibrium becomes unstable. This may be because the filament radius exceeds the critical value and the photospheric background field is relatively weak. After the formation of the current sheet, a relatively slow (compared with the eruption caused by loss of ideal-MHD equilibrium) eruption may be triggered by the tearing mode instability developed in the current sheet when the length of the sheet reaches certain value (Priest, 1982a). This implies that a huge filament in a relatively weak field environment may erupt at certain height. Eruptions of quiescent prominences might be examples of this type of eruption (Isenberg, Forbes & Démoulin, 1992). Other possible examples are those thermal flare with no impulsive phase.

Summary

A detached current sheet model for eruptive flares, CME's and prominence ejections has been developed based on the assumption of three characteristic time scales, namely, τ_p, for convective motions in the photosphere, τ_r, for reconnection in the corona, and τ_A for Alfvén wave propagation in the corona. The analysis makes the assumption that $\tau_p >> \tau_r >> \tau_A$. The model is an MHD version of the circuit model first proposed by Van Tend and Kuperus (1978) for erupting prominences. By allowing reconnection in the corona, we have generalized the attached current sheet model of Forbes and Isenberg (1991), and solved the vector potential problem for a flux rope in a

field configuration which contains a detached current sheet and which satisfies the line-lied boundary condition in the photosphere.

In this new model a current sheet starts to develop when the magnetohydrostatic equilibrium of the system becomes unstable. The magnetohydrostatic equilibrium is maintained by the balance between the magnetic compression and tension forces acting on the filament. Work done by the convective motions in the photosphere increases the total magnetic energy of the system by transferring magnetic flux from the photosphere to the corona. As this process proceeds, the filament is driven upwards quasi-statically until the equilibrium is suddenly lost.

An important result based on the ordering of three characteristic time scales in our model is that the critical point in the evolution of the system equilibrium is just the critical point of the 'vacuum' equilibrium evolution in which no current sheet forms. Unlike Forbes and Isenberg (1991), we have assumed that magnetic reconnection in the corona is much faster than the convective motion in the photosphere so that no current can be formed or sustained before the system reaches the critical point. This allows us to study the preflare phase of an eruptive flare. The preflare phase in our model is identified with the period starting when the x-type neutral point appears at the photospheric boundary and ending when the system reaches the critical point.

The critical point of the system moves towards the point at which the neutral point appears at the photospheric boundary when filament radius r approaches zero, and the two points become identical when $r = 0$. Therefore, as $r \rightarrow 0$, the asymptotic solution of the detached current sheet will be the same as that of the attached case obtained by Forbes and Isenberg (1991) because the lower end of the current sheet approaches the photospheric boundary as $r \rightarrow 0$.

Unlike any previous analyses, our analysis here distinguishes between equilibrium losses due to ideal-MHD processes and those due to non-ideal MHD (i.e., reconnection) processes. When filament radius is less than certain critical value, an eruption occurs due to catastrophic loss of ideal-MHD equilibrium, and the current sheet lengthens rapidly during the eruption. This current sheet is destroyed in the successive non-ideal-MHD process called the reconnection jump which occurs after the eruption. If the filament radius is greater than the critical value, no catastrophe occurs. However, in the later case, a current sheet still forms due to the loss of magnetohydrostatic equilibrium, and a relatively slow non-ideal eruption occurs. If filament radius is less than the critical value, the system evolves through three stages, i.e., the quasi-static evolution, the catastrophic eruption, and the reconnection jump. On the other hand, if filament radius is greater than the critical value, then the system evolves through two stages only, namely the quasi-static evolution and the reconnection jump.

The critical value of the filament radius corresponds to the critical value of stored magnetic energy in the corona before the system reaches the critical point. The above discussion indicates that if the stored energy is greater than the critical value before the eruption, then an ideal-MHD jump occurs and the flare eruption is associated with an impulsive phase. However, if the system can not acquire enough energy (exceeding the critical value) before it reaches the critical point, the corresponding flare lacks an impulsive phase.

Considering that the effect of a current sheet is to hold the filament and stabilize the equilibrium, the critical value of the energy required for an impulsive phase to occur in the detached current sheet case is less than that in the attached case, because in the detached case no current sheet is formed before the eruption. In other words, the critical radius of the filament in the detached current sheet model is larger than the critical radius of the filament in the corresponding attached model.

The eruptions caused by catastrophic loss of ideal-MHD equilibrium correspond to the impulsive phase at the start of the eruptive flare phenomenon. The fraction of the total stored magnetic energy released during the eruption will be liberated within a few Alfvén time scales. The remaining fraction of the energy will be released by magnetic reconnection during the gradual phase. Such reconnection might be nearly as fast as the Alfvén time scale (see Forbes, 1990), but here we have assumed that this is not the case.

PART TWO

THE STRUCTURE OF RADIATIVE SLOW-MODE SHOCKS

CHAPTER 5

INTRODUCTION

It has long been recognized that magnetic reconnection plays a very important role in solar flare phenomena (Giovanelli, 1947; Sweet, 1958; Parker, 1963; Petschek, 1964; Sonnerup, 1979; 1984; Priest, 1984; 1985b), and magnetic reconnection has been used to explain the observed energy release in solar flares and the formation of the flare loops (Parker, 1984; Malherbe, Forbes, and Priest, 1984; Forbes, 1986; Priest and Forbes, 1986; Low and Wolfson, 1988; Forbes, Malherbe, and Priest, 1989). Solar flare loops, with their temperature ranging from 10^4 to 3×10^7 K, are unusually dense compared with the surrounding corona (Lin, Lin, and Kane, 1985; Withbroe, 1978; Zirin, 1986; Heinzel and Karlický, 1987), and they are long-lived features which may persist for 10 hours or more. An enormous amount of material—greater than the mass of the entire corona—flows through the flare loops system during its lifetime (Kleczek, 1964; Kopp and Pneuman, 1976). Thus, the evolution of the flare loops involves not only reconnection, but also the additional processes of chromospheric ablation and thermal condensation (Sturrock, 1972; Hirayama, 1974; Ohki, 1975; Schmieder *et al.*, 1987; Forbes and Malherbe, 1986a; 1986b).

Slow-Mode Shocks and Isothermal Subshocks

MHD slow-mode shocks, which were first introduced in reconnection theory by Petschek in 1964, are the key link between magnetic reconnection and chromospheric ablation (see, e.g., Cargill and Priest, 1982). To see why this is so, consider Figure 17 which shows the expected shock pattern in the reconnection model of flare loops by

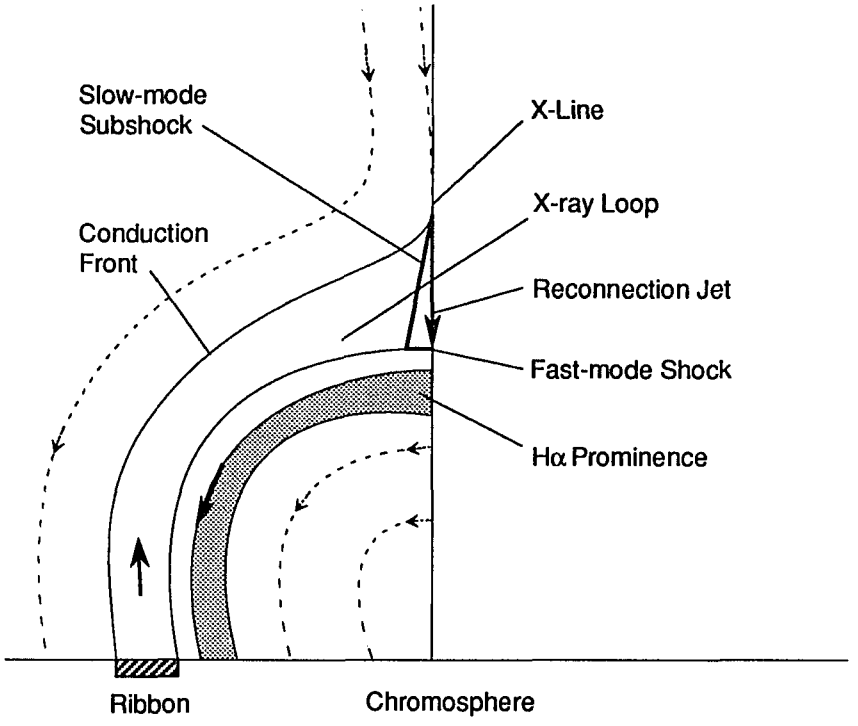

Fig. 17. Expected flow pattern in the reconnection model of flare loops. Chromospheric ablation is continually driven by heat released from magnetic field annihilation. As field lines (dashed lines) are reconnected, the loops grow in size, and the ribbons propagate outward, away from the axis of sysmmetry (after Forbes *et al.*, 1989).

Forbes *et al.*, (1989). According to this model reconnection occurs at a coronal x-line which lies at the intersection of two pairs of slow-mode shocks. These shocks convert magnetic energy into bulk flow kinetic energy and heat. Due to the strong thermal conduction along the field lines, the slow shocks dissociate into isothermal subshocks and foreshocks (thermal conduction fronts) (Forbes and Malherbe, 1986b), but the jump conditions across the total shock transition, from upstream of the foreshock to downstream of the subshock, are given by the usual slow mode jump conditions. The foreshocks and the subshocks annihilate the magnetic field in the plasma flowing through them, and the thermal energy released in the annihilation is spread out all along the field lines. Consequently the heat is conducted from the corona to the chromosphere and leads to extensive heating and ablation of chromospheric plasma, creating and sustaining the hot x-ray loops.

The thickness of the total shock transition is of the order of the scale-size of the loops. Therefore, the total transition can no longer be considered strictly as a shock since its thickness is not small compared to its extension in the other dimensions. However, the subshocks still exist as proper shocks, although strictly speaking they should no longer be thought of as subshocks.

Formation of Flare Loops

The plasma which crosses the subshocks forms a pair of reconnection jets which are directed towards and away from the photosphere. Unlike the upward jet, the downward jet forms on field lines which are connected to the chromosphere. Consequently, evaporation injects dense chromospheric plasma into the lower jet but not into the upper one. Because the downward jet is supermagnetosonic with respect to the fast-mode wave speed, it terminates at a fast shock (termination shock) below which is a region of deflected flow, forming a deflection sheath (see Forbes, 1986). As

reconnection proceeds, the *x*-line moves upward, and field lines on which the ablated plasma is flowing move through the termination shock and become disconnected from the subshocks. Once the field lines are disconnected, the plasma on them is no longer heated, and it immediately begins to cool. During the cooling, a thermal instability is triggered and the plasma temperature drops below the corona temperature. This cool plasma forms the visible Hα loop prominence where the cool plasma flows, or falls, down the legs of the loops and returns to the chromosphere.

Brief Overview

In the past 25 years, studies of the structure, the stability and the propagation of slow-mode shocks in different aspects (Kantrowitz and Petschek, 1966; Coroniti, 1970; Bel and L.-Micoulant, 1973; Rosenau, 1978; Swift, 1983; Feldman *et al.*, 1984; 1985; 1987; Hada and Kennel, 1985; Winske, Stover, and Gary, 1985; Edmiston and Kennel, 1986; Kennel, 1987; 1988; Richter, 1988) have built up a considerable knowledge base about slow shocks. However, very little work has yet been done on the radiative slow shocks involved in the evolution of solar flares.

The structure of slow shocks becomes much more complicated when radiation and thermal conduction are both taken into consideration. The large density of the flare loops makes radiative cooling a significant factor in the energy equilibrium. The effect of radiation on shock wave behavior in fluid dynamics has long been studied. One of the first studies on radiative fluid dynamic shocks was done by Marshak (1958). And some authors have studied radiative shocks in connection with the evolution of supernova remnants (Cox and Tucker, 1969; Cox, 1972a; 1972b; Chevalier, 1974; Chevalier and Theys, 1975). An analysis of radiative shocks must necessarily include coronal heating to reflect the radiative coupling with the surrounding coronal

environment. Accordingly, when talking about radiative cooling, we consider both radiative cooling and coronal heating as a united process unless otherwise specified.

The purpose of this part of the thesis is to present a theoretical analysis on the structure of radiative slow shocks. In addition to the foreshock and the subshock there is a radiative cooling region downstream of the subshock. The plasma flowing through this region radiates the excess heat generated during its passage through the shock. Some radiative loss also occurs in the foreshock region, but in general the dominant radiative loss occurs in the downstream region.

It should be kept in mind that the very concept of a simple planar shock transition is not directly applicable to flare loops, since in flare loops the foreshock region extends all the way from the reconnection site to the chromosphere. This distance is on the order of the size of the loops, hence the total shock transition cannot be considered planar. The actual problem of the structure of the flare loops is more complicated than the problem of planar shocks. Furthermore, in flare loops ablation of chromospheric plasma by the conduction electrons and energetic particles is a dominant factor in the formation of the loops. By ignoring this ablation process in this paper and assuming shocks to be planar, this analysis of radiative slow-mode shocks represents only a first step in modeling the actual structure of flare loops.

For purposes of comparison and illustration, the structure of radiative gas dynamic shocks in a thermally conducting medium will be first considered. Following this, the structure of MHD switch-off shocks where the component of magnetic field tangential to the shock is annihilated completely, will be then determined . Switch-off shocks are very good approximations to the type of slow shocks that are likely to exist when reconnection occurs in the corona (Petschek, 1964).

In Chapter 6 that follows, the MHD equations given in Chap. 2 will be specified in the 'shock-rest' frame, and the structure will be considered as a steady-state one in this frame. The corresponding boundary conditions will be determined according to the energy equilibrium between coronal heating and radiative cooling. In Chapter 7 an analytic solution of shock structure will be derived by means of the *boundary layer analysis* for the specific case of gas dynamics with the strong thermal conduction but negligible radiative cooling. For the case in which radiation is significant, the effect of the cooling on the equilibrium in the downstream region of isothermal subshock will be discussed. Chapter 8 discusses the MHD jump relations for the total shock transition as well as the isothermal subshock, including some details about switch-off shocks. Then both analytical and numerical effort will be concentrated on radiative switch-off shocks to determine the effects of radiative cooling on the shock structure, finally the principal results will be summarized.

CHAPTER 6

GOVERNING EQUATIONS FOR MHD SHOCKS

Steady-state Equations in Shock-Rest Frame

The fundamental MHD equations used here are the same equations given in Chap. 2. Consider the stationary movement of a plane shock propagating along the positive x direction at a speed V_0. Two coordinate systems are adopted: the laboratory frame in which the fluid upstream of the shock is at rest, while the shock wave propagates through it; and a shock-rest frame in which the shock stays at rest while the fluid flows through it at the velocity $-V_0$, as shown in Figure 18.

The shock-rest frame is related to the lab. frame by transformation $z = x - V_0 t$. Accordingly, in the shock-rest frame, the component MHD equations are:

$$P = \rho R T, \tag{6-1a}$$

$$dB_x/dz = 0, \tag{6-1b}$$

$$d(\rho V_x)/dz = 0, \tag{6-1c}$$

$$d[V_x B_y + V_y B_x + \eta (dB_y/dz)]/dz = 0, \tag{6-1d}$$

$$d[P + B_y^2/2\mu + \rho V_x^2 + (4\rho\nu/3)(dV_x/dz)]/dz = 0, \tag{6-1e}$$

$$d(\rho V_x V_y + B_x B_y/\mu + \rho\nu(dV_y/dz)]/dz = 0, \tag{6-1f}$$

$$\gamma P dV_x/dz + V_x dP/dz + (\gamma - 1)[d(\kappa dT/dz)/dz - \rho^2 Q(T) + \rho H_c + \eta[(dB_y/dz)^2/\mu + \rho\nu\{4(dV_x/dz)^2/3 + (dV_y/dz)^2\}] = 0, \tag{6-1g}$$

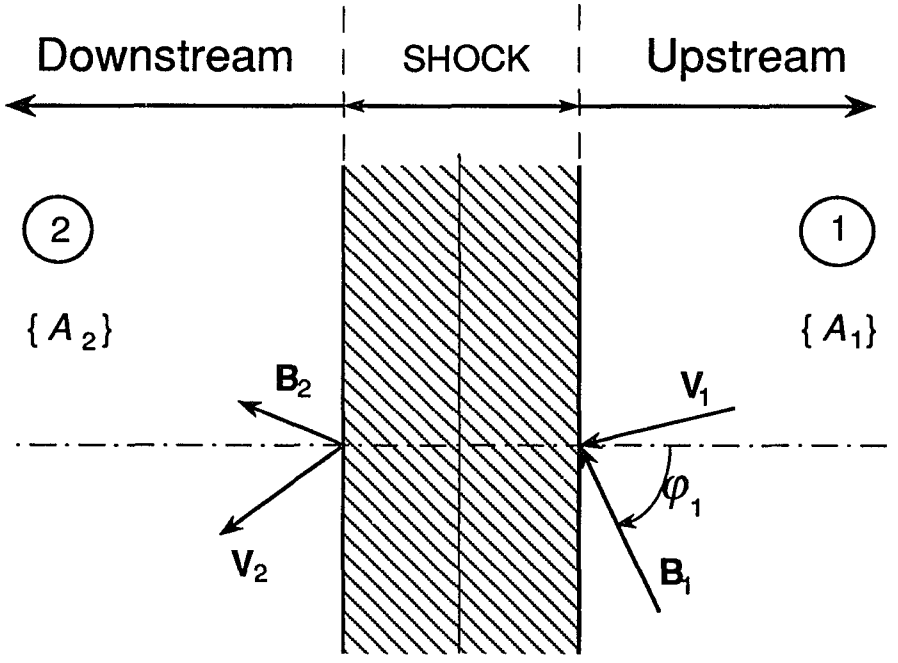

Fig. 18. Schematic diagram of the slow shock geometry in the shock-rest frame. The upsteam and downstream parameters are labeled by subscripts 1 and 2, repectively

where P, ρ, T, γ, R, and μ denote the pressure, the density, the temperature, the ratio of specific heats, the gas constant, and the magnetic permeability, respectively. The quantities $B_x(V_x)$and $B_y(V_y)$ are the normal and the tangential components of magnetic field (velocity), and $V_x = V_0 - v$, where v is the perturbed fluid velocity (in the lab frame) normal to the shock. The dissipation coefficients are the magnetic diffussivity η, the kinematic viscosity ν, and the thermal conduction κ. The optically thin radiative cooling is characterized by cooling function $\rho^2 Q(T)$, while coronal heating is characterized by the heating function ρH_c , where H_c is a constant. In reality H_c is not constant but is instead an unknown function of the magnetic field and possibly of the plasma variables. On the absence of any theory of coronal heating, we follow the generally accepted procedure of assuming H_c as a constant.

Physical Considerations and Assumptions

In an ideal fluid shocks are discontinuities, since ν, η, and κ vanish. However, for a real fluid with finite dissipation coefficients, shocks are transition layers in which dissipation effects are balanced by nonlinear effects. The "thickness" of the transition layer is measured by the scale length of the corresponding dissipation.

To emphasize the effect of radiative cooling, the dissipation coefficients η, ν, and κ are treated as constants throughout the following sections. It will be also assumed that the scale lengths of viscosity' L_ν, and resistivity, L_η, are comparable but much smaller than thermal conduction scale length, L_κ.

The radiative cooling function $Q(T)$ takes form of $\tilde{\chi} T^{\alpha}$, where $\tilde{\chi}$ and α are piecewise constants (Cox and Tucker, 1969; Priest, 1982a). For simplicity we will consider two simple approximations: First, a single value of α, i. e., $\alpha = 2$, therefore $\tilde{\chi}$ is a constant for all temperature; and second, two values of α, i. e., $\alpha = 2$ for $T < T_c$ and $\alpha = -1/2$ for

$T > T_c$, with corresponding constants $\tilde{\chi}$ for each α value. The temperature T_c is defined as the critical temperature at which $Q(T)$ reaches a maximum. Figure 19 shows an analytic fit of radiative cooling function $Q(T)$ by Rosner et al. (1978) as well as our two-value α fit.

Boundary Condition

The occurrence of slow shocks requires $V_0 > C_{sL1}$, where C_{sL1} is slow-mode wave speed given by the smaller value of

$$C_{sL1}^2 = \frac{1}{2}\left\{C_{A1}^2 + C_{s1}^2 \pm \left[\left(C_{A1}^2 + C_{s1}^2\right)^2 - 4\, C_{A1}^2\, C_{s1}^2 \cos\varphi_1\right]^{\frac{1}{2}}\right\}. \qquad (6\text{-}2a)$$

For isothermal subshocks, the condition is $V_{xd} < \tilde{C}_{sLd}$ (Coroniti, 1970), where $\tilde{C}_{sLd}$ is the downstream isothermal slow-mode wave speed given by the smaller value of

$$\tilde{C}_{sLd}^2 = \frac{1}{2}\left\{C_{Ad}^2 + \tilde{C}_{sd}^2 \pm \left[\left(C_{Ad}^2 + \tilde{C}_{sd}^2\right)^2 - 4 C_{Ad}^2\, \tilde{C}_{sd}^2 \cos\varphi_d\right]^{\frac{1}{2}}\right\}, \qquad (6\text{-}2b)$$

here C_A, C_s, $\tilde{C}_s$ and φ denote the Alfvén speed, the sound speed, the isothermal sound speed and field direction, respectively. The upstream (downstream edge of subshock) parameters are labeled by subscript $1(d)$. Coroniti's condition indicates that an isothermal subshock occurs when the total shock strength exceeds the critical value so that the dissipation of thermal conduction can no longer balance the nonlinear effect of the strong shock, hence additional dissipations, such as viscosity, have to be introduced.

It is usually assumed that the motion of fluid outside the total transition layer is uniform and steady (viewed in the shock-rest frame). Hence $d/dz = 0$ except within the transition layer. This physical consideration requires, therefore, that radiative

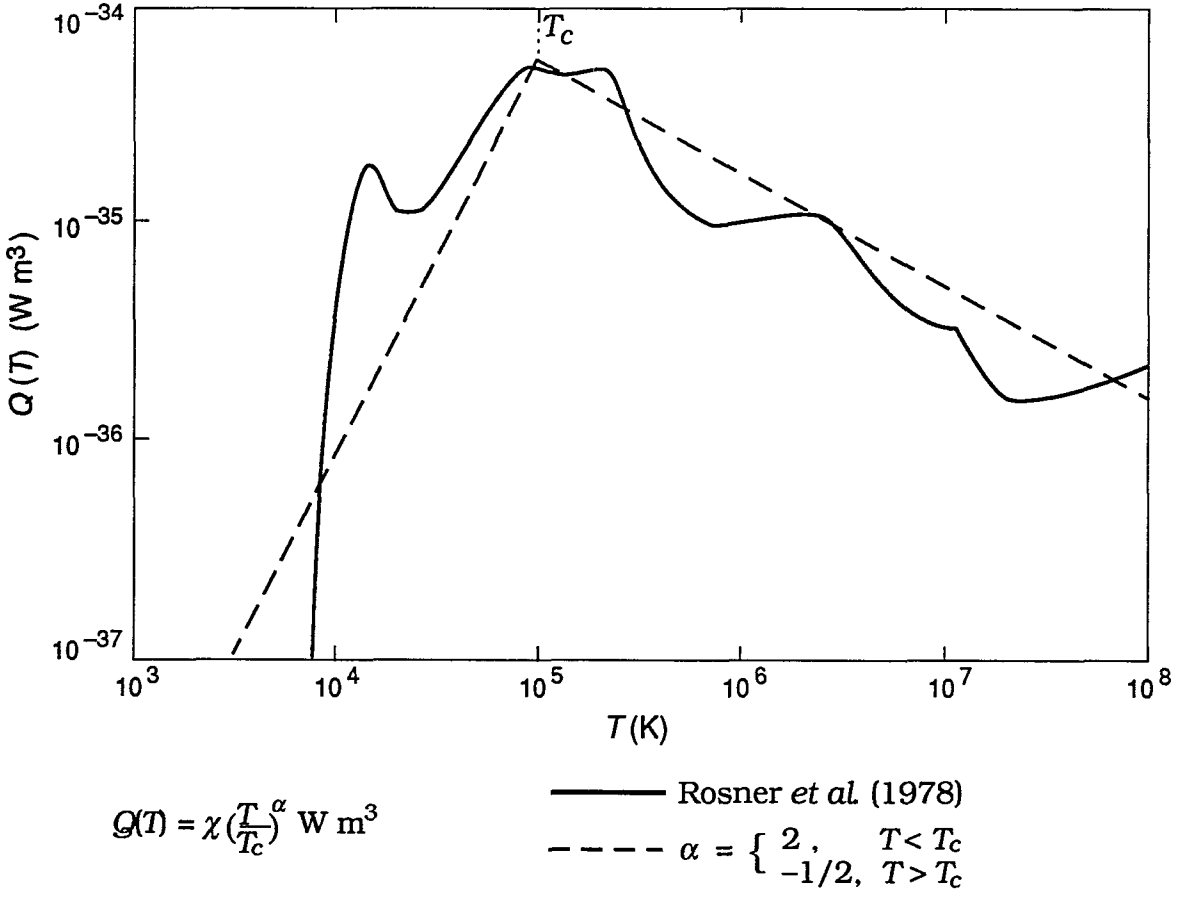

Fig. 19. The optically thin radiative loss function $Q(T)$ for the solar atmosphere. The solid curve is an analytic fit by Rosner *et al.*, while the dashed curve is the two-value fit used here.

cooling be balanced by coronal heating outside the total transition layer. The outer boundary conditions (OBC's), i. e., the equilibrium conditions, are expressed accordingly as

$$\rho^2 Q(T) - \rho H_c \to 0, \text{ as } z \to \infty \text{ or } z \to -\infty, \tag{6-3a}$$

$$d/dz \to 0, \text{ as } z \to \infty \text{ or } z \to -\infty, \tag{6-3b}$$

$$A \to A_1, \text{ as } z \to \infty, \tag{6-3c}$$

$$A \to A_2, \text{ as } z \to -\infty, \tag{6-3d}$$

where A denotes an arbitrary physical parameter (see Figure 18).

The OBC's above are often given as general BC's of the MHD Rankine-Hugoniot (R-H) relations, when all the transitions are confined within the total shock layer. However, this is not the case when radiative cooling in the downstream region of the subshock is considered. Equation (6-3a) describes the equilibrium requirement in the far downstream region, which, in general, is not satisfied by the MHD R-H relations. According to Kennel (1987), an isothermal viscous subshock occurs at the downstream edge of the total shock transition. Therefore, the MHD jump relations specify the parameters at the downstream edge of the subshock rather than in the region far downstream of the radiative cooling region. So the region immediately downstream of the subshock is no longer uniform. Instead, in the radiative cooling region in which the variation of physical parameters is mainly due to the effect of radiation, the flow is nonuniform and thus $d/dz \neq 0$ at the downstream edge of the shock transition. The total transition is no longer the same as the total shock transition since the total transition now consists of the shock transition and the radiative cooling region. Thus the inner boundary conditions (IBC's) of the radiative slow shocks are defined as those MHD jump relations for the total shock including the subshock transition. The IBC's

may also include the non-zero derivatives of the physical parameters at both upstream and downstream edges of the subshocks, if necessary.

CHAPTER 7

RADIATIVE GAS DYNAMIC SHOCKS

Before considering the slow-mode radiative shocks, we first review the simpler case of radiative shocks without magnetic field. This review is necessary because the structure of radiative gas shocks has been little discussed in space physics literature. Almost all work on radiative gas dynamic shocks has been done in connection with interstellar blast waves created by supernovae (see Chevalier and Theys, 1975).

Basic Equations and Boundary Conditions

The elimination of the magnetic field simplifies Equations (6-1) to

$$P = \rho RT, \tag{7-1a}$$

$$d(\rho V)/dz = 0, \tag{7-1b}$$

$$d[P + \rho V^2 + (4\rho\nu/3)(dV/dz)]/dz = 0, \tag{7-1c}$$

$$\gamma P\frac{dV}{dz} + V\frac{dP}{dz} + (\gamma - 1)\left[\frac{d}{dz}\left(\kappa\frac{dT}{dz}\right) - \rho^2\mathcal{Q}(T) + \rho H_c + \frac{4}{3}\rho\nu\left(\frac{dV}{dz}\right)^2\right] = 0. \tag{7-1d}$$

The OBC's are given by Equations (6-3), i.e., $d/dz \to 0$ as $z \to \infty$ or $z \to -\infty$, so that

$$[\rho\mathcal{Q}(T) - H_c]_1 = [\rho\mathcal{Q}(T) - H_c]_2, \tag{7-2a}$$

the IBC's are derived by integrating Equations (7-1*b*)-(7-1*d*)),

$$X = \frac{(\gamma + 1)M_1^2}{\gamma M_1^2 + 1 - \sqrt{(M_1^2 - 1)^2 + \Delta}}, \tag{7-2b}$$

$$Y = \frac{\gamma M_1^2 + 1 + \gamma\sqrt{(M_1^2-1)^2 + \Delta}}{\gamma + 1}, \tag{7-2c}$$

$$X_S = X\eta_g - 1, \tag{7-2d}$$

where M_1 is the upstream Mach number, $V_0 = V_1$, and

$$\eta_g = (P_1 + \rho_1 V_0^2)/\rho_1 V_0^2 = 1 + 1/\gamma M_1^2, \tag{7-3a}$$

$$\Delta = 2(\gamma + 1)M_1^4 I, \tag{7-3b}$$

$$I = \frac{\gamma - 1}{\rho_1 V_0^3}\left\{\left(\kappa\frac{dT}{dz}\right)\Big|_d - \frac{4}{3}\frac{\rho_1 V_0 \nu}{(\gamma-1)}\left(\frac{dV}{dz}\right)\Big|_d + \int_d^1 \rho[\rho\mathcal{Q}(T) - H_C]dz\right\}. \tag{7-3c}$$

The quantities X and Y represent the total shock jump, and X_S gives the subshock jump:

$$X = \frac{V_1}{V_d} = \frac{\rho_d}{\rho_1}, \qquad Y = \frac{P_d}{P_1}, \qquad X_S = \frac{V_S}{V_d} = \frac{\rho_d}{\rho_S} = \frac{P_d}{P_S}.$$

Thus, Coroniti's condition becomes $X_S > 1$.

The above OBC's and IBC's imply that radiative cooling affects the shock structure in two ways. First, as an integral effect, radiative cooling changes the jump conditions for shocks and subshocks since the ordinary jump relations are replaced by Equations (7-2) and (7-3). Second, radiative cooling creates a radiative region attached at the downstream edge of the isothermal subshock. The extent of the first effect depends on the thickness of the shock because if the shock is very thin, the radiative loss within the shock is negligible. Figure 20 shows a schematic plot of the shock geometry. The thicknesses of the shock and the subshock are determined by thermal and viscous scale lengths, respectively. Fluid flows through the various regions which are indicated as follows:

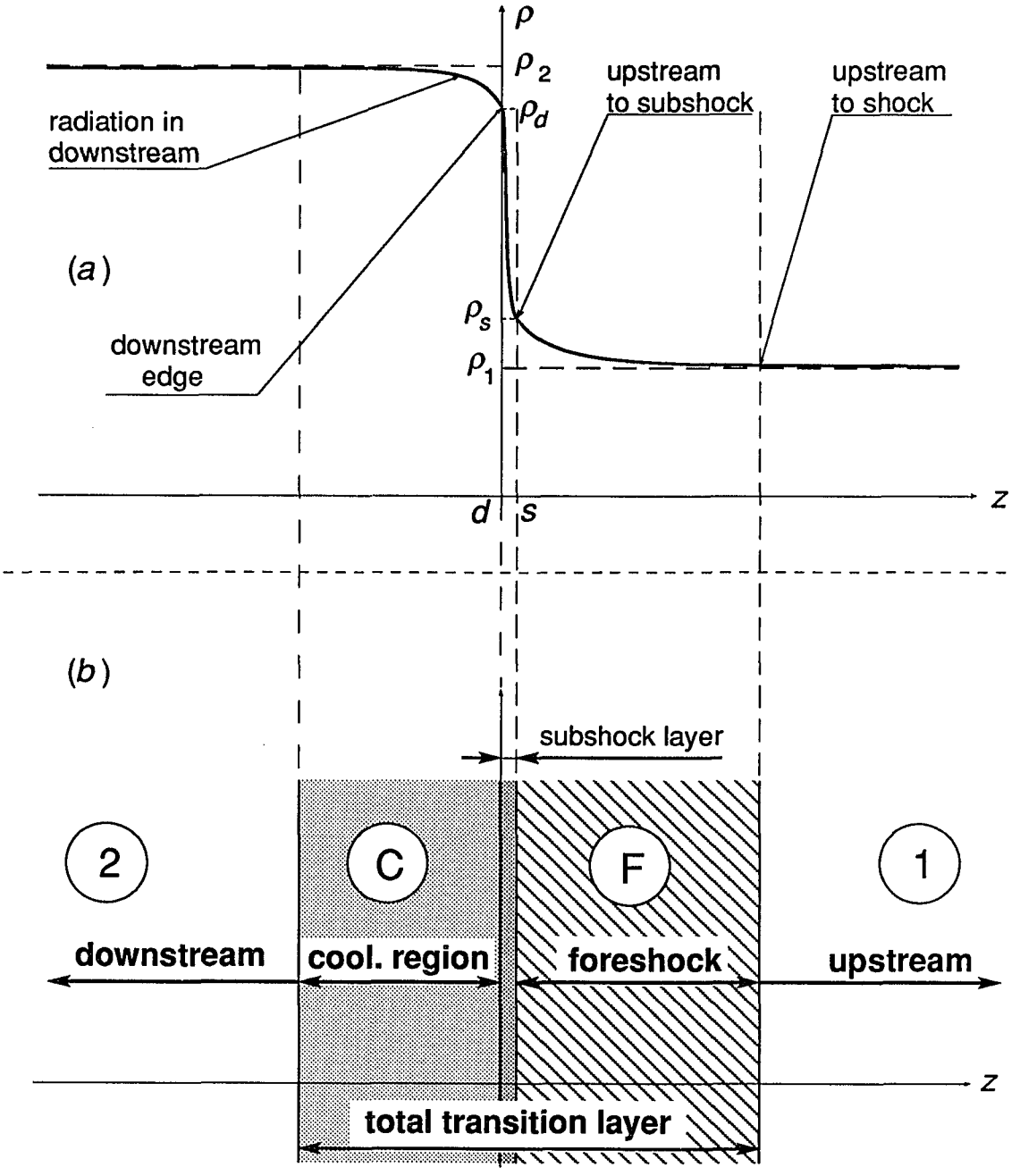

Fig. 20. A schematic diagram for gasdynamic shock structure: (a) the density curve; (b) different regions of shock structure. Subscripts d and s denote the downstream and upstream edges of subshock, respectively.

upstream of total shock transition—[1]; foreshock—[*F*];

upstream edge of subshock—[*s*]; downstream edge of subshock—[*d*];

radiative cooling region—[*C*]; far downstream of shock—[2].

In this thesis the subshock is assumed to be very thin compared to all other scale lengths, or equivalently, $v = 0$ ($\eta = 0$ is also expected because $v \sim \eta$ is assumed). Thus the radiative energy loss within the subshock is negligible. By contrast, the foreshock is assumed to be very thick, so that the radiative loss in the foreshock is not negligible.

Thermal Conduction Alone

When the effect of radiative cooling is negligible, the outer and inner boundary conditions reduce to the ordinary BC's for gas dynamic shocks because region *C* vanishes. That is, if *A* denotes an arbitrary parameter, then $A_1 = A_\infty$, $A_d = A_2 = A_{-\infty}$, $(dA/dz)|_1 = (dA/dz)|_d = 0$, and

$$X = \frac{(\gamma+1)M_1^2}{(\gamma-1)M_1^2+2}, \tag{7-4a}$$

$$Y = \frac{2\gamma M_1^2-(\gamma-1)}{\gamma+1}, \tag{7-4b}$$

$$X_S = X\eta_g - 1, \tag{7-4c}$$

The condition $X_S > 1$ leads to $M_1^2 > M_c^2$, where M_c is the critical Mach number defined by

$$M_c^2 = \frac{3\gamma-1}{\gamma(3-\gamma)}. \tag{7-5}$$

Integrating Equations (7-1*b*) and (7-1*c*) and substituting the results into Equations (7-1*a*) and (7-1*d*) gives

$$\rho = \rho_1 V_0/(V_0 - v), \tag{7-6a}$$

$$P = P_1 + \rho_1 V_0 v + (4\rho\nu/3)(dv/dz), \tag{7-6b}$$

$$T = T_1 + (1/R)\{v[V_0 - P_1/(\rho_1 V_0) - v] + (4\nu/3)(dv/dz)\}, \tag{7-6c}$$

$$[\gamma P_1 - \rho_1 V_0^2 + (\gamma+1)\rho_1 V_0 v]\frac{dv}{dz} = \frac{d}{dz}\left[\frac{4}{3}\rho_1 V_0 \nu \frac{dv}{dz} + (\gamma-1)\kappa\frac{dT}{dz}\right], \tag{7-6d}$$

where $v = V_0 - V$. One equation for $v(z)$ can be drawn from equations (7-6), and once this equation is solved, the corresponding shock structure is obtained.

Analytical Solution

The well known solution of Burger's equation (Whitham, 1974) gives the shock structure for weak shocks (i.e., $\Delta V << V_0$) with no subshock present (see Appendix B)

$$v = \frac{V_0 - V_d}{1 + exp\left[(V_0^2 - C_{S1}^2)z/(\delta_\kappa V_0)\right]}, \tag{7-7}$$

where V_d is the downstream fluid velocity, C_{S1} is the upstream sound speed, $\Delta V = V_0 - V_d$,

$$\delta_\kappa = (\gamma-1)\kappa/(\rho_1 c_p),$$

and c_p is the specific heat at constant pressure.

To derive the shock structure for strong shocks with isothermal subshocks, we treat the subshock as a boundary layer, in which the derivatives of the physical parameters become very large. Therefore Equations (7-6) can be solved approximately by means of the boundary layer analysis.

If the subshock is located at $z = 0$, a boundary layer with a thickness proportional to L_ν appears in the vicinity of $z = 0$. The approximate solution for the velocity is

$$v = \frac{(V_0 - V_s)(V_0 - V_d)}{V_0 - V_s + (V_s - V_d)exp[(V_0^2 - C_{s1}^2)z/(\delta_\kappa V_0)]} + \frac{V_s - V_d}{1 + exp[(V_s - V_d)z/\delta_\nu}, \qquad (7\text{-}8)$$

where V_S is the fluid velocity at upstream edge of the subshock, $\delta_\nu = 4\nu/3$.

the quantities δ_κ and δ_ν ($\delta_\nu/\delta_\kappa = o(\varepsilon)$, here ε is the parameter of smallness) give the measure of thermal scale length L_κ and viscous scale length L_ν, respectively (for detailed derivation see Appendix B).

Numerical Calculation

The boundary layer analysis only gives an approximate solution, so in order to know how good the approximation is, we calculated a numerical solution using a Runge Kutta algorithm (see notes in Appendix D).

Equation (7-6d) is first integrated to read

$$-\frac{\gamma+1}{2} v(V_0 - V_d - v) = \frac{4}{3}\nu\frac{dV}{dz} + \frac{(\gamma-1)\kappa}{\rho_1 V_0}\frac{dT}{dz}, \qquad (7\text{-}9)$$

Next Equations (7-9) and (7-6c) are combined, rearranged, and normalized to obtain

$$\frac{d\overline{T}}{d\xi} = \frac{\gamma-1}{2}\gamma\overline{V}^2 + \frac{\gamma-1}{M_1}\overline{V} - \overline{T}, \qquad (7\text{-}10a)$$

$$\frac{d\overline{V}}{d\xi} = R_{LHD}\left[\frac{\overline{T}}{\gamma M_1} + \frac{\overline{V}^2}{M_1} - \overline{V}\left(1 - \frac{1}{\gamma M_1^2}\right)\right], \qquad (7\text{-}10b)$$

where

$$\overline{T} = \frac{T - T_1}{T_1}, \quad \overline{V} = \frac{v}{C_{s1}}, \quad \xi = \frac{z}{L_\kappa}, \quad R_{LHD} = \frac{L_\kappa}{L_\nu}, \quad L_\kappa = \frac{\gamma\kappa}{\rho_1 V_0 c_p}, \quad L_\nu = \frac{4}{3}\frac{\nu}{V_0}.$$

Equations (7-10) represent a two-dimensional autonomous system which has two critical points, namely point **A** at $(\overline{V}, \overline{T}) = (0, 0)$, and point **B** at $(\overline{V}, \overline{T}) = (\overline{V}_d, \overline{T}_d)$, as shown in Figure 21. The two points, **A** and **B**, correspond to the upstream and downstream

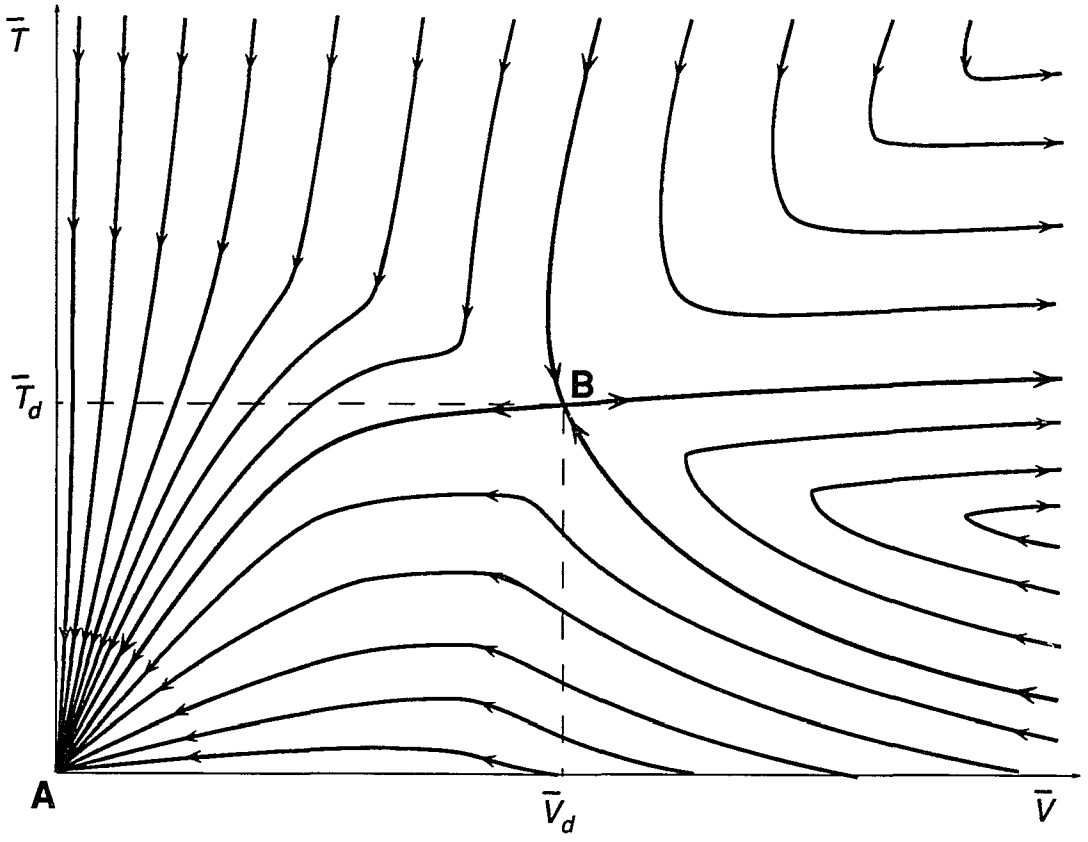

Fig. 21. Schematic diagram of the solution to system (7-10). Two critical points **A** and **B** are corresponding to the upstream and downstream of the standard R-H jump relations. Thus, the curve connecting **A** and **B** gives the solution satisfying the boundary conditions that the upstream and downstream regions are uniform.

values of the shock transition, and the curve connecting these points gives the standard Rankine-Hugoniot jump conditions for uniform upstream and downstream conditions. The other curves are for transitions with non-uniform upstream and downstream conditions.

The behavior of the solution to Equation (7-10) near these two critical points can be studied by the *critical-point analysis* (see Bender and Orszag, 1978, and Appendix C). Critical-point analysis indicates that point **A**, at (0, 0), is a stable node while point **B**, at $(\overline{V}_d, \overline{T}_d)$, is a saddle point. Because of the behavior of system near the two critical points, it is better to start at the shock, i.e., $(\overline{V}_d, \overline{T}_d)$, and integrate towards the upstream region when solving Equations (7-10) numerically. The jump conditions for the shock and subshock now serve as initial conditions for the numerical calculation. To avoid using the infinity as a boundary condition in the calculation, the $\overline{T}(\overline{V})$ curve is calculated first. Then, by setting the subshock location to $\xi = 0$ and choosing $\overline{V}(0)$ and $\overline{T}(0)$ from $\overline{T}(\overline{V})$, all other curves depending on ξ can be integrated from the subshock towards the upstream and downstream regions, respectively. Figures 22 and 23 compare the numerical results with the analytical results from the boundary layer approximation.

The good agreement between the analytic and numerical solutions indicates that the boundary layer analysis is effective in dealing with the detailed structure of both the subshock and the foreshock. Figure 23 shows that the numerical and analytic solution tends to be identical in the limit $R_{LHD} \rightarrow \infty$.

Radiation Alone

To clarify the effect of radiative cooling, we first consider the simple case in which thermal conduction is zero. The total shock transition reduces to a discontinuity when

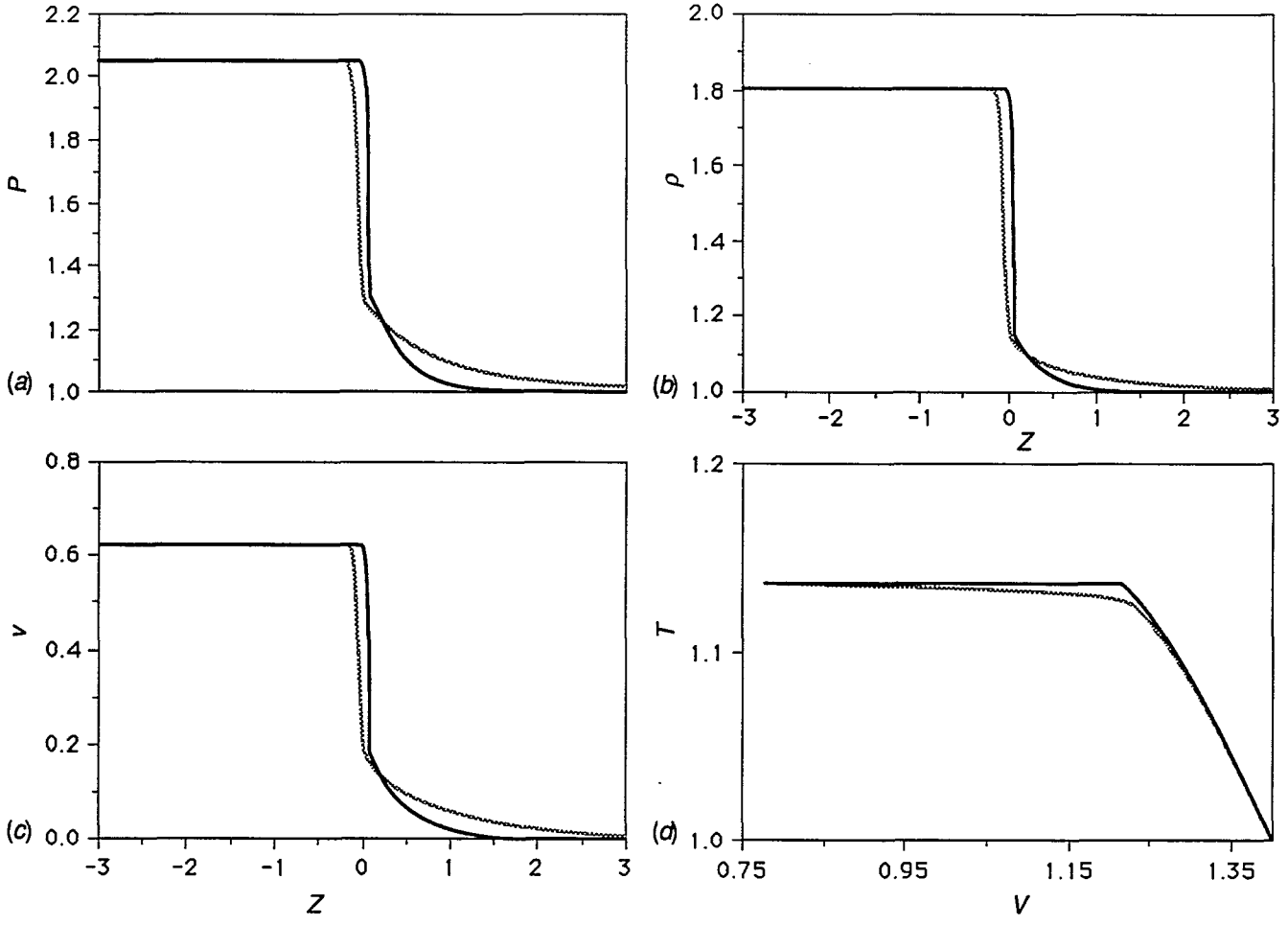

Fig. 22. Comparison of solutions for the radiative gasdynamic shock . From (a) to (c) are the pressure $P(z)$, the density $\rho(z)$, and the velocity $v(z)$, respectively. Fig. (d) shows $T(V)$. Solid curves represent solutions by boundary layer analysis, dashed curves are numerical solutions. The units of T, P, V, ρ, $v\,(=V_0-V)$ are T_1, P_1, V_0, ρ_1, and V_0, respectively, and the upstream condition is $M_1 = 1.38$.

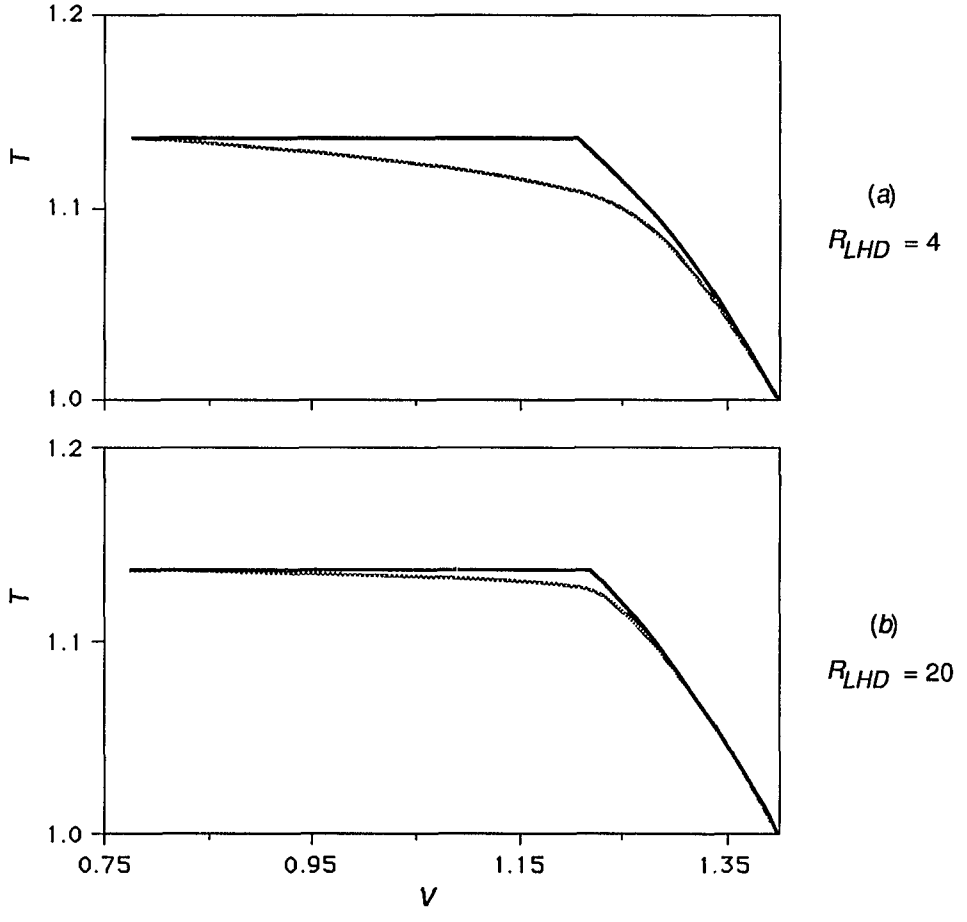

Fig. 23. Comparison of the analytic solution (solid) to the numerical solution (dashed). The parameters are the same as those in Fig. 22, except for R_{LHD}, the ratio of the thermal scale length to viscous scale length. As R_{LHD} becomes larger and larger, the two solutions become more identical.

$\kappa = 0$, and the jump conditions are those of an ordinary gas dynamic shock. The solution for region C is easily found by substituting $\nu = 0$ and $\kappa = 0$ into (4), that is

$$V = uV_1, \tag{7-11a}$$

$$\rho = \rho_1/u, \tag{7-11b}$$

$$P = \rho_1 V_0^2(\eta_g - u), \tag{7-11c}$$

$$T = V_0^2(\eta_g - u)u/R, \tag{7-11d}$$

where $u(z)$ is the normalized gas velocity satisfying

$$[\gamma\eta_g - (\gamma+1)u]du/dz = (\gamma-1)\rho[\rho\mathcal{Q}(T) - H_c]/(\rho_1 V_0^3), \tag{7-12}$$

with $\mathcal{Q}(T) = \tilde{\chi}T^{\alpha}$, and $d/dz \to 0$ (as $z \to -\infty$), i. e. ,

$$H_c = \rho_1\mathcal{Q}(T_1) = \rho_2\mathcal{Q}(T_2) \tag{7-13}$$

The matter we are most concerned about is whether or not the above equations lead to a physically realistic solution. Let's first look at the case $\alpha = 2$.

Substituting $\alpha = 2$ into Equation (7-13) produces a cubic equation for u, namely,

$$[u(\eta_g - u)^2]|_2 = (\eta_g - 1)^2. \tag{7-14}$$

It has three roots ($u_+ > u_o > u_-$):

$$u_o = 1,$$

and

$$u_{\pm} = [2\eta_g - 1 \pm (4\eta_g - 3)^{1/2}]/2.$$

The quantity u_o represents the trivial solution of no shock at all because it gives a downstream velocity which is the same as the upstream velocity. The solution u_+ gives

an unphysical solution because it leads to a negative value for the downstream pressure. Thus the only choice for a physical solution is

$$u_2 = u_- = [\,2\eta_g - 1 - (4\eta_g - 3)^{1/2}]/2. \tag{7-15}$$

Equation (7-12) can then be normalized and rewritten as an autonomous system, i.e.,

$$\frac{du}{d\xi_R} = \frac{\gamma-1}{u}\,\frac{(u-1)\,(u-u_2)\,(u-u_+)}{\gamma\eta_g - (\,\gamma+1)u}\,, \tag{7-16}$$

where $\xi_R = z\,\rho_1 Q(T_1)/[V_0^3(\eta_g - 1)^{\,2}]$. Critical-point analysis shows that $u = u_2$ is a stable node of the system (7-16). This means that the combined effect of radiative cooling and wave heating is to drive the system towards thermal equilibrium in the downstream region when $\alpha = 2$. This conclusion can be generalized further to all α satisfying

$$\alpha > \frac{\eta_g - u^*}{\eta_g - 2u^*} = \alpha_0, \tag{7-17}$$

where $1 < \alpha_0 < \infty$, and u^* represents the expected solution of Equation (7-13). For the other values of α, the effect of radiative cooling is to drive the system away from equilibrium, and thus the system is thermally unstable. In other words, the plasma flow will approach equilibrium in the downstream region only when condition (7-17) is satisfied, otherwise no proper equilibrium can be reached.

The cooling function $Q(T)$ in the temperature range appropriate for the corona and flare loops ($10^4 - 3 \times 10^7$ K) may be roughly modeled as (see Priest, 1982a):

$$Q(T) = \begin{cases} Q_<(T) = \tilde{\chi}_< T^{\,2}, & T < T_c \\ Q_>(T) = \tilde{\chi}_> T^{\,-1/2}, & T > T_c \end{cases} \tag{7-18}$$

where $\tilde{\chi}_{>} = 10^{-31.5}$, $\tilde{\chi}_{<} = 10^{-44}$, and $T_c = 10^5$ K. Figure 19 shows schematically this two-value α fit. The velocity u_c, corresponding to T_c, is

$$u_c = \frac{1}{2}\left[\eta_g - \sqrt{\eta_g^2 - 4\,T_c / (V_0^2/R)}\right]. \tag{7-19}$$

Since we wish to apply our results to flare loops we will assume that the upstream temperature corresponds to that of the chromosphere (2×10^4 K) rather than the corona (10^6 K). Hence, in the upstream region we set $\alpha = 2$, and $H_c = \rho_1 \mathcal{Q}(T_1) = \rho_1 \tilde{\chi}_{<} T_1^2$. According to the previous discussion and condition (7-17), the equilibrium in the downstream region is approached only when $\alpha = 2$ (i. e., $T < T_c$). Thus the cooling in region C is governed by

$$\frac{du}{d\xi_R} = \frac{\gamma-1}{u}\,\frac{(u-1)(u-u_2)(u-u_+)}{\gamma\eta_g - (\gamma+1)u}, \qquad u < u_c, \tag{7-20a}$$

$$\frac{du}{d\xi_R} = \frac{\gamma-1}{u\,[\gamma\eta_g - (\gamma+1)u]}\left[\frac{(T_c\,R/V_0^2)^{5/2}}{u^{3/2}(\eta_g-u)^{1/2}} - (\eta_g-1)^2\right], \quad u > u_c. \tag{7-20b}$$

Radiation and Thermal Conduction Combined

The differential equation for the velocity u in a radiative gas dynamic shock with thermal conduction as derived from Equations (7-1) is

$$[\gamma\eta_g - (\gamma+1)u]\,du/d\xi = D_{RC} - d\mathcal{Q}_g/d\xi, \tag{7-21}$$

where $\xi = Z/L_\kappa$, the length L_κ is the thermal scale length of the total shock defined by $L_\kappa = \gamma\kappa/(\rho_1 c_p V_0)$, and D_{RC} is the differential energy loss due to radiative cooling, i.e.,

$$D_{RC} = (\gamma-1)R_L\,u_c\,[\rho_1\mathcal{Q}(T)/(uH_c) - 1]/u, \tag{7-22}$$

where $R_L = L_\kappa H_C / u_C V_0^3$ is a dimensionless constant representing the ratio of the thermal scale length L_κ to characteristic length of radiative cooling L_R, defined by $L_R = u_C V_0^3 / H_C$.

For the two-value α case, D_{RC} is:

$$D_{RC} = (\gamma - 1) R_L u_c [u(\eta_g - u)^2 / T_1^2 - 1] / u, \qquad T < T_C \tag{7-23a}$$

$$D_{RC} = (\gamma - 1) R_L \frac{u_c}{u} \left[(T_C / T_1)^2 u^{-3/2} \sqrt{T_C / (\eta_g - u)} - 1 \right], \quad T > T_C \tag{7-23b}$$

The normalized heat flux ($\kappa \nabla T$) is

$$Q_g = \mathrm{d}[u(\eta_g - u)] / \mathrm{d}\xi = (\eta_g - 2u)\, \mathrm{d}u / \mathrm{d}\xi. \tag{7-24}$$

The boundary condition of Equation (7-21) is given by Equations (7-2) and $v = 0$, where Δ is replaced by Δ_g,

$$\Delta_g = 2(\gamma + 1) M_1^4 I_g, \tag{7-25a}$$

and

$$I_g = R_C + Q_g|_d = \int_d^1 D_{RC}\, \mathrm{d}\xi + [(\eta_g - 2u)\, \mathrm{d}u / \mathrm{d}\xi]|_d \,. \tag{7-25b}$$

Do Equation (7-21) and its accompanying BC's lead to a physical solution? The answer can only be found by investigating the behavior of $u(\xi)$ in the region downstream of the subshock. Let's rewrite Equation (7-21) as a 2-D autonomous system:

$$\mathrm{d}u / \mathrm{d}\xi = Q_g / (\eta_g - 2u), \tag{7-26a}$$

$$\mathrm{d}Q_g / \mathrm{d}\xi = D_{RC} - [\gamma \eta_g - (\gamma + 1)u] Q_g / (\eta_g - 2u). \tag{7-26b}$$

It can be shown by critical-point analysis that condition (7-17) is the decisive criterion for the above question. If $u = u^*$ satisfies the equilibrium equation $\rho Q(T) - \rho_1 Q(T_1) = 0$, i.e., $D_{RC} = 0$, then the point $(u, Q_g) = (u^*, 0)$ is a critical point of the system (7-

26). When the condition (7-17) is not satisfied, $(u^*, 0)$ is an unstable node or an unstable spiral point—in the phase plane of (u, Q_g), all trajectories near the point $(u^*, 0)$ move away from it as $\xi \to -\infty$. The physical interpretation is that radiative cooling drives the system away from the equilibrium. By contrast, $(u^*, 0)$ becomes a saddle point when α satisfies condition (7-17). That is, trajectories near this point approach it in a specific direction, and move away from it in the other direction. Only one trajectory reaches this point as $\xi \to -\infty$ (see Bender and Orszag, 1978), and this special trajectory corresponds to the expected physical solution. In other words, the system approaches the appropriate equilibrium in the downstream region when $\alpha > (\eta_g - u^*)/(\eta_g - 2u^*)$.

For example, when $\alpha = 2$, the autonomous system (7-26) has three critical points, namely, $(u, Q_g) = (1, 0)$, $(u_2, 0)$, and $(u_+, 0)$. Point $(u_2, 0)$ corresponds to the physical solution, and this point is a saddle point near which trajectories approach it in the direction $dQ_g/du = A_{g+}$ and move away from it in the direction $dQ_g/du = A_{g-}$, where

$$A_{g\pm} = \frac{1}{2}\left\{(\gamma+1)u_2 - \gamma\eta_g \pm \sqrt{[\gamma\eta_g - (\gamma+1)u_2]^2 + 4(\gamma-1)R_L\frac{u_c}{u_2}\frac{(\eta_g-2u_2)(\eta_g-3u_2)}{T_2}}\right\}. \quad (7\text{-}27)$$

Figure 24 diagrams the saddle point behavior of the solution of the system (7-26) near the point $(u_2, 0)$. The figure shows that $(u_2, 0)$ can be reached only through the trajectory $(dQ_g/du = A_{g+})$ as $\xi \to -\infty$.

What if $\alpha < (\eta_g - u^*)/(\eta_g - 2u^*)$ and $u_d = u^*$? This special value of u_d corresponds to the solution where equilibrium is reached immediately at the downstream edge of the subshock. For this solution there is no cooling region at all, but the solution is still an unstable one because any tiny deviation from it would immediately drive the system away from equilibrium.

Accordingly, we conclude that the downstream equilibrium can only be reached at a temperature lower than T_c. In other words, the downstream fluid must cool down from

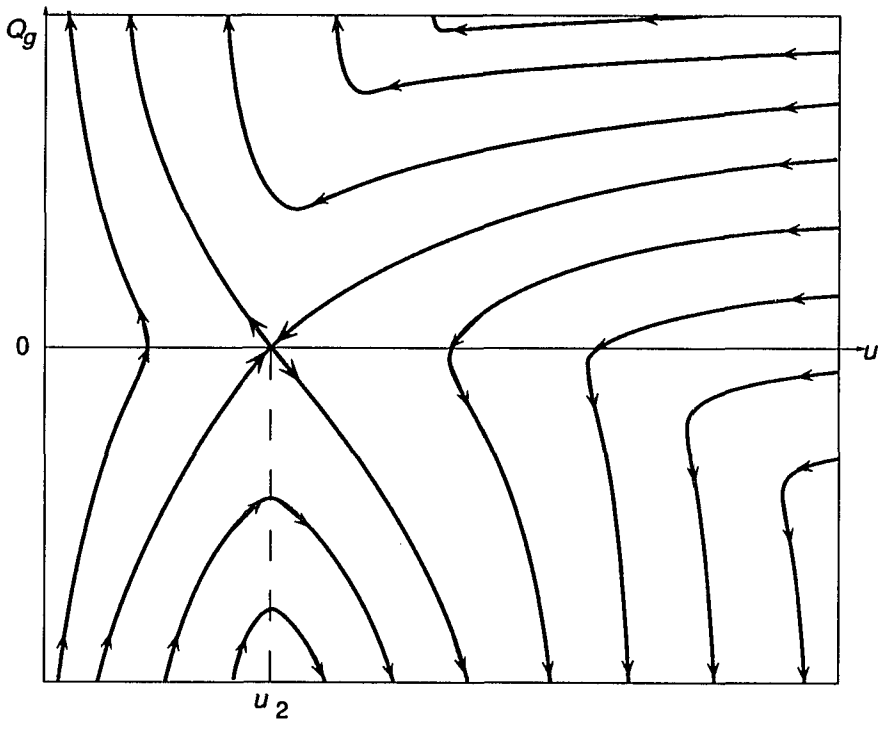

Fig. 24. Schematic plot for solution of system (7-26) near $(u_2, 0)$—saddle point behavior ($\alpha = 2$). One, and only one, trajectory would reach $(u_2, 0)$ in the direction $(dQ_g/du)|_2 = A_{g+}$, as $\xi \to -\infty$.

its high temperature above T_c to a low temperature below T_c, if it is to reach an equilibrium. The lack of steady-state solutions for $T_d > T_c$ reflects the fact that a plasma on the high-temperature side of the maximum of $Q(T)$ is thermally unstable (Cox and Tucker, 1969).

The velocity u can be obtained by solving Equation (7-21) numerically. However, an important point has to be taken into consideration in doing the numerical calculation. As mentioned previously, the introduction of radiative cooling changes the jump conditions radically. When radiative cooling is negligible, X, the density jump for total shock, is completely determined by the upstream parameters. However, when radiative cooling is not negligible, X depends not only on the upstream parameters, but also on the shock solution (see above expressions of Δ_g and I_g). That is, we need to know X before solving Equation (7-21), whereas X depends on the solution of Equation (7-21). A similar situation also occurs when the radiative MHD equations are solved numerically. We use an iterating method to deal with this problem, and this method is discussed further in the following sections and Appendix D.

Figure 25 shows the numerical solution of Equation (7-21) for $\alpha = 2$. Also shown is the shock solution when radiation is absent. The principal effect of the radiation is to decrease the temperature and flow speed in the downstream cooling region.

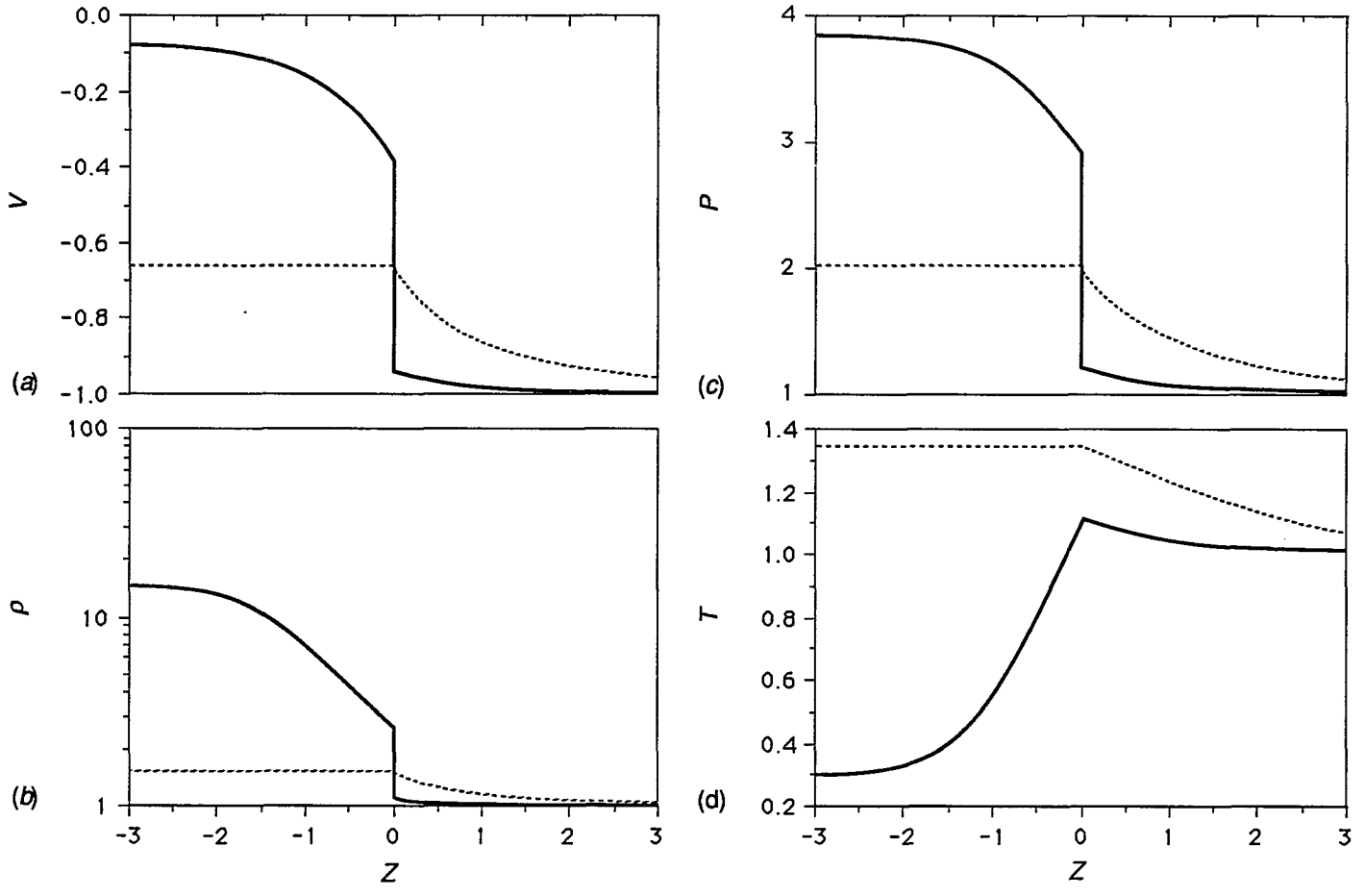

Fig. 25. Numerical solution for the radiative gasdynamic shock. Panels (a) to (d) plot respectively the variations of the velocity, the density, the pressure and the temperature in the total shock transition region. The corresponding units are the same as those in Fig. 22, but the upstream conditions are $M_1 = 1.35$, $R_L = 1$, and $u_c = 0.1$. Solutions with no radiation ($R_L = 0$) are also plotted in dashed curves for comparison.

CHAPTER 8

SLOW MODE SHOCKS

In this chapter we determine the shock structure of MHD slow-mode shocks in the switch-off shock limit. This limit means that there is no tangential magnetic field in the region downstream of the subshock, so for this region the solution is similar to the gas dynamic solution. However, as we will see, in the foreshock region upstream of the subshock it is considerably different. Physically, the most significant difference between the gas dynamic shock and the slow shock is that the gas dynamic shock converts the kinetic energy of the flow into heat, while the slow shock converts magnetic energy into both heat and kinetic energy. As before, the jump conditions at the subshock serve as IBC's and the starting point for numerical integration of the shock structure equations. Because these MHD jump relations are much more complicated than the gas dynamic ones, we will discuss the MHD jump relations separately before considering the integration of the shock structure equations.

In analyzing shock structure it is very helpful to know what conditions must be given in order to define a unique shock transition. It is well known that for ordinary gas dynamic shocks that one parameter, such as the upstream Mach number, is enough. By comparison, three parameters are needed for ordinary MHD shocks. For example, the upstream plasma β, the Alfvén Mach number, and the field direction are sufficient. When radiation is taken into consideration, an extra parameter has to be introduced to describe the effect of the radiation. In this thesis, R_L—the ratio of the thermal scale length L_κ to characteristic length of radiative cooling L_R, where $L_\kappa = \gamma\kappa/(\rho_1 c_p V_0)$, $L_R =$

$u_c V_0^3/H_c$, is chosen as the parameter. Since L_K is also the scale length of the total shock transition, this choice of R_L gives a measure of the strength of the radiative cooling.

Thermal Conduction Alone

General Jump Relations for Total Shock and Subshock

With no radiative cooling, equations (6-1) can be integrated across the total shock transition layer (see Figure 18) and rearranged to read

$$\frac{X\beta_1}{\theta_1}+\frac{\gamma-1}{\gamma}(X+1)-2\cos^2\varphi_1+\left(X-\frac{\gamma-1}{\gamma}\theta_1\right)\frac{X\theta_1+\theta_1-2X}{(X-\theta_1)^2}\sin^2\varphi_1=0, \tag{8-1a}$$

$$Y=1+\beta_1^{-1}\left\{\sin^2\varphi_1+2\theta_1\cos^2\varphi_1\left(1-\frac{1}{X}\right)-\left[\sin\varphi_1\frac{X(1-\theta_1)}{X-\theta_1}\right]^2\right\}, \tag{8-1b}$$

where X and Y are defined as: $X = \rho_d/\rho_1 = V_{x1}/V_{xd} = V_0/V_{xd}$, $Y = P_d/P_1$, and

$$B_{yd}/B_{y1} = X(1-\theta_1)/(X-\theta_1), \tag{8-2a}$$

$$V_{yd} = V_{y1} + V_0\, tg\,\varphi_1(X-1)/(X-\theta_1), \tag{8-2b}$$

$$B_x = B_{x1}, \tag{8-2c}$$

$$\theta_1 = V_0^2/C_{AX1}^2 \le 1, \tag{8-2d}$$

$$C_{Ax1}^2 = C_{A1}^2\cos^2\varphi_1 = B_{x1}^2/(\mu\rho_1), \tag{8-2e}$$

$$\beta_1 = 2\mu P_1/B_1^2, \tag{8-2f}$$

$$\cos\varphi_1 = B_{x1}/B_1. \tag{8-2g}$$

Here β_1, C_{Ax1} and $\cos\varphi_1$ denote the upstream plasma parameter ($\beta_1 << 1$ for solar flares), the Alfvén speed normal to the shock, and the magnetic field direction, respectively.

The above relations are the general jump conditions for MHD slow-mode shocks. The real root (greater than 1) of the cubic equation (8-1*a*) gives the density jump X, and all of the other physical parameters can be determined once X is known.

Jump conditions for the isothermal subshock can be derived by integrating Equations (6-1) across the subshock (from *d* to *s*) and using the isothermal condition $T_s = T_d$ to replace the energy equation (6-1*g*). Then combining the results with Equations (8-2) and $\nu = 0$, $\eta = 0$, we obtain:

$$2\theta_1\cos^2\varphi_1\,(X_s+1-X) - X\beta_1 - X\sin^2\varphi_1\left[1-\left(\frac{X-X\theta_1}{X-X_s\theta_1}\right)^2\frac{X^2-X_s\theta_1^2}{(X-\theta_1)^2}\right]=0, \qquad (8\text{-}3a)$$

$$B_{ys} = B_{y1}X(1-\theta_1)/(X-X_s\theta_1), \qquad (8\text{-}3b)$$

$$V_{ys} = V_{y1} + V_0\, tg\,\varphi_1(X-X_s)/(X-X_s\theta_1). \qquad (8\text{-}3c)$$

Switch-off Shock Limit

For switch-off shocks (see Figure 26), $B_{yd} = 0$ (i. e., $\theta_1 = 1$), hence the shock speed is the same as upstream Alfvén speed normal to the shock. Accordingly, we obtain

$$X = \frac{1+\beta_1+\cos^2\varphi_1+\sqrt{(\beta_1+\sin^2\varphi_1)^2+4\cos^2\varphi_1\,(1-\beta_1\gamma)/\gamma^2}}{2[\,\beta_1+(\gamma-1)/\gamma]}, \qquad (8\text{-}4a)$$

$$Y = 1+\beta_1^{-1}\,(1+\cos^2\varphi_1-2\cos^2\varphi_1/X), \qquad (8\text{-}4b)$$

$$V_{yd} = V_{y1} + V_0\, B_{y1}/B_{x1}. \qquad 8\text{-}4c)$$

As mentioned in Chapter 6, Coroniti's condition has to be satisfied in order for isothermal subshocks to occur, i. e., $V_{xd} < \widetilde{C}_{sLd}$, where $\widetilde{C}_{sLd}$ is given by the smaller value of Equation (6-2*b*).

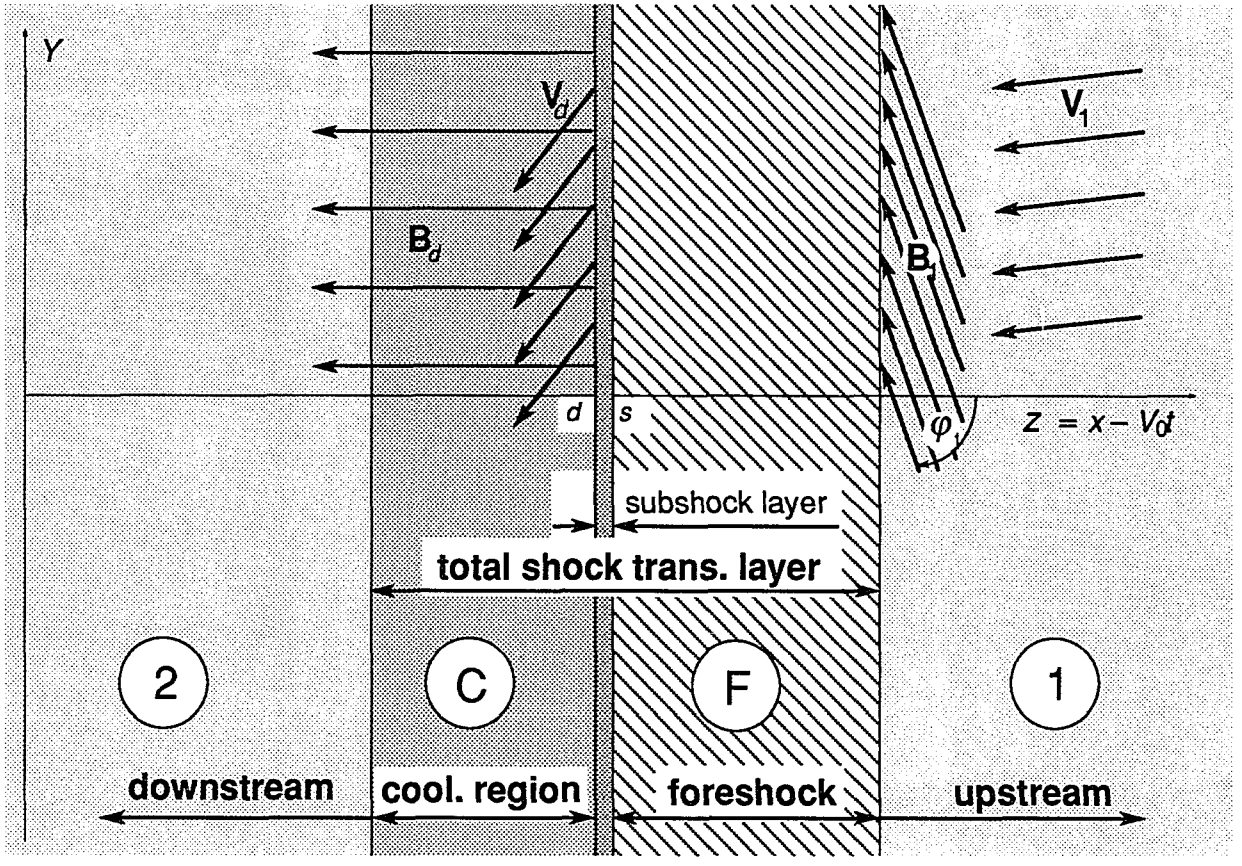

Fig. 26. Schematic geometry of the slow-mode switch-off shock.

For switch-off shocks, $\varphi_d = 0$, hence $C_{Ad}^2 = C_{Axd}^2 = C_{Ax1}^2/X$. From

$$\widetilde{C}_{sd}^2 = P_d/\rho_d = C_{Ad}^2 \beta_d/2 = Y C_{A1}^2 \beta_1/2X,$$

One finds that

$$\beta_d = Y\beta_1 C_{A1}^2/C_{Ax1}^2 \approx C_{A1}^2/C_{Ax1}^2 >> 1, \tag{8-5}$$

since $B_{y1}^2 >> B_{x1}^2$, i. e., $\widetilde{C}_{sd}^2 >> C_{Ad}^2$.

Therefore, $\widetilde{C}_{sLd}^2 = C_{Ad}^2$, and the formation of the isothermal subshock in a slow-mode switch-off shock is ensured because for $X > 1$,

$$C_{Ax1}/X = V_0/X = V_{xd} < \widetilde{C}_{sLd} = C_{Ad} = C_{Ax1}/\sqrt{X}. \tag{8-6}$$

When $\theta_1 = 1$, two possible solutions for isothermal subshocks can be drawn directly from Equation (8-3*b*):

$$\text{a) } B_{yS}=0; \qquad \text{b) } X=X_S.$$

The solution $B_{yS} = 0$ is an impossible result for real shocks because it leads to $X_S > X$ (subshock jump is greater than total shock jump), and therefore, for switch-off shocks, the isothermal subshock jump condition is $X_S = X$. The foreshock may then be thought of as a "tangential shock" because only the tangential components of velocity and magnetic field are changed, while the normal components of velocity and magnetic field remain unchanged.

The subshock jump of the fluid variables are:

$$V_{xs} = V_0, \tag{8-7a}$$

$$\rho_S = \rho_1, \tag{8-7b}$$

$$P_S = P_1 Y/X = P_1\left[1+\beta_1^{-1}\left(1+\cos^2\varphi_1 - 2\cos^2\varphi_1/X\right)\right]/X, \tag{8-7c}$$

$$B_{ys}^2 = B_{y1}^2 (X-1)[X+(X\beta_1 - 2\cos^2\varphi_1)/\sin^2\varphi_1]/X^2, \tag{8-7d}$$

$$V_{ys} = V_{y1} + V_0 (B_{y1} - B_{ys})/B_{x1}. \tag{8-7e}$$

Table 1 shows the jump conditions for some typical solar flare loops.

The normal fluid velocity and the density are constants in the foreshock region of switch-off shocks. This behavior makes switch-off shocks quite different from gasdynamic shocks and fast-mode MHD shocks. As Table 1 shows we expect:

$$\beta_1 << 1;\ \beta_d >> 1;\ \beta_s \leq 1,$$

therefore,

$$X \approx \left(1 + \beta_1 + \gamma^{-2}\cos^2\varphi_1\right)/[\beta_1 + (\gamma-1)/\gamma], \tag{8-8a}$$

$$Y \approx \beta_1^{-1}, \tag{8-8b}$$

$$V_{yd} \approx C_{A1}, \tag{8-8c}$$

$$B_{ys} \approx B_{y1}\sqrt{(X-1)/X}. \tag{8-8d}$$

Equation (8-8*d*) implies that of the total energy released by the annihilation of the magnetic field in the shock, about $1/X$ is released in the foreshock region while about $1-1/X$ is released at the subshock. For typical flare loop conditions $X \approx 3$, therefore above results suggest that about 2/3 of the magnetic energy will be released at the subshocks, i.e., at the top of the flare loops, while the remaining 1/3 will be released in the region upstream of the subshocks.

For the near switch-off shocks, fast wave speed $C_{fd} \approx C_{sd}$, the downstream sound speed, since $B_{yd}/B_{y1} << B_{yd}/B_x < 1$ and $\beta_d >> 1$. Therefore,

$$V_{yd}^2/C_{fd}^2 \approx 2XY^{-1}\beta_1^{-1}/\gamma \approx 2X/\gamma > 1,$$

Table 1. Shock and Subshock Jump Conditions

($T_1 = 2 \times 10^4$ K, $B_1 = 100$ G, $n_1 = 5 \times 10^{10}$ cm^{-3})

$B_{x1}/B_1 = V_0/C_{A1} = V_{y1}/V_0 = M_{1A}$, M_{1A} is the upstream Alfvén Mach number

$C_{A1} = 9.76 \times 10^2$ km/s is the upstream Alfvén speed

reg.	M_{1A}	V_x/V_{x1}	V_y/V_{y1}	B_y/B_{y1}	ρ/ρ_1	T/T_1	P/P_1	β
1	0.1	1.00	1.00	1.00	1.00	1.00	1.00	3.47×10^{-4}
	0.01	1.00	1.00	1.00	1.00	1.00	1.00	3.47×10^{-4}
s	0.1	1.00	23.76	0.772	1.00	1.15×10^3	1.15×10^3	0.665
	0.01	1.00	2.26×10^3	0.775	1.00	1.15×10^3	2.89×10^3	0.667
d	0.1	0.399	1.01×10^2	0	2.51	1.15×10^3	2.89×10^3	1.00×10^2
	0.01	0.400	1.00×10^4	0	2.50	1.15×10^3	2.88×10^3	1.00×10^4

and the downstream flow is supermagnetosonic with respect to the fast-mode wave speed.

When

$$\cos^2 \varphi_1 = X(1+\beta_1)/(X+2),$$

$B_{ys} = 0$, $\beta_d = 2$, and hence the subshock is simply a gas dynamic shock for

$$\cos^2 \varphi_1 \geq X(1+\beta_1)/(X+2). \tag{8-9}$$

The subshock vanishes when $\beta_d \leq 2/X$. (8-10)

Radiation and Thermal Conduction Combined

In the light of the discussion in the last chapter, we let $\nu = \eta = 0$ for simplification so that isothermal subshocks reduce to discontinuities. The modification of the MHD jump conditions is discussed first. Next we determine the fluid velocity in the regions upstream and downstream of the subshock. Because the switch-off shock is quite different from the gasdynamic shock, the fluid velocity behaves differently than before.

Modification of Jump Relations

When radiative cooling is taken into account, the jump conditions obtained in the previous section need to be modified correspondingly. Actually, all other relations would remain the same as before, except the expression for X. The equation for X now reads

$$X^2[\beta_1 + (\theta_1 - I_0)(\gamma-1)/\gamma] - X\left(\beta_1 + 2\theta_1 - \theta_1^2 \sin^2\varphi_1\right) + \theta_1 \cos^2\varphi_1(\gamma+1)/\gamma$$
$$+X\theta_1 \sin^2\varphi_1 (X/\gamma + X - \theta_1)[(1-\theta_1)/(X-\theta_1)]^2 = 0. \tag{8-11}$$

For switch-off shocks,

$$X=\frac{1+\beta_1+\cos^2\varphi_1+\sqrt{(\beta_1+\sin^2\varphi_1)^2+4\cos^2\varphi_1\,[1-\beta_1\gamma+(\gamma^2-1)\,I_0]/\gamma^2}}{2[\,\beta_1+(1-I_0)\,(\gamma-1)/\gamma]}\,, \tag{8-12}$$

where

$$I_0=\left[2M_{1A}^2/(\rho_1 V_0^3)\right]\left\{(\kappa\,dT/dz)|_d+\int_d^1 \rho[\,\rho\mathcal{Q}(T)-H_c]\,dz\right\}$$

$$=\left[=\left[2M_{1A}^2/(\gamma-1)\right]\left\{(dT/d\xi)_d+\int_d^1(\gamma-1)\,R_L\,u_c[\rho_1\mathcal{Q}(T)/H_c-\right.\right.\frac{d\xi}{}\Bigg\} \tag{8-13}$$

is the normalized effect of radiative loss as well as the heat flux at the downstream edge of the subshock, $M_{1A} = V_0/C_{A1}$ is the upstream Alfvén Mach number ($M_{1A} << 1$ since we have assumed $B_{y1} >> B_{x1}$).

Radiation in Foreshock Region

Substituting $B_x = B_{x1}$, $V_x = V_o$, $\rho = \rho_1$ into Equations (6-1), we obtain immediately that in the foreshock

$$V_0B_y+B_{x1}V_y = V_0B_{y1}+B_{x1}V_{y1}, \tag{8-14a}$$

$$P+B_y^2/2\mu = P_1+B_{y1}^2/2\mu, \tag{8-14b}$$

$$d(\kappa\,dT/dz)/dz+\rho_1V_0R(dT/dz)/(\gamma-1)-\rho_1[\,\rho_1\mathcal{Q}(T)-H_c]=0. \tag{8-14c}$$

Equation (8-14*c*) is the critical equation—once it is solved for T, all the other physical parameters are readily obtained. If T is expressed in units of $T_o = V_o^2/R$, then Equation (8-14*c*) is reduced to

$$d^2T/d\xi^2+dT/d\xi-(\gamma-1)\,R_L\,u_c[\rho_1\mathcal{Q}(T)/H_C-1]=0, \tag{8-15}$$

by appropriate normalization (notations follow Equation (8-21)).

If the radiative loss function $Q(T)$ is fitted with a two-component piecewise curve (i.e., $\alpha = 2$ and $\alpha = -1/2$), then by using $\tilde{\chi}_< T_c^2 = \tilde{\chi}_> T_c^{-1/2}$, Equation (8-15) can be written as,

$$d^2T/d\xi^2 + dT/d\xi - (\gamma - 1) R_L u_c[(T/T_1)^2 - 1] = 0, \qquad T < T_c, \tag{8-16a}$$

$$d^2T/d\xi^2 + dT/d\xi - (\gamma - 1) R_L u_c\left[T_c^{5/2}/\left(T_1^2 T^{1/2}\right) - 1\right] = 0, \quad T > T_c, \tag{8-16b}$$

Equations (8-16) govern the behavior of T in the foreshock region and can be solved numerically.

Radiation and Equilibrium in the Downstream Region

In the downstream region, the switch-off condition $B_y = 0$ leads to $V_y = V_{yd}$ so that the plasma movement exhibits pure gas dynamic behavior. The equation for $u = V_x/V_0$ is then reduced from Equations (6-1) by substituting in $B_y = 0$ and $V_y = V_{yd}$ and normalizing. The result is

$$\frac{d^2}{d\xi^2}[u(\eta_0 - u)] + [\gamma\eta_0 - (\gamma + 1)u]\frac{du}{d\xi} - (\gamma - 1) R_L \frac{u_c}{u}\left[\frac{\rho_1 Q(T)}{u H_C} - 1\right] = 0, \tag{8-17}$$

where

$$\eta_0 = \frac{P_d + \rho_1 V_0 V_{xd}}{\rho_1 V_0^2} = \frac{P_1 + B_{y1}^2/2\mu + \rho_1 V_0^2}{\rho_1 V_0^2} = 1 + \frac{\beta_1 + \sin^2\varphi_1}{2M_{1A}^2}. \tag{8-18}$$

Equation (8-17) has the same form as Equation (7-21) (with Equation (7-24) substituted in) except η_g is replaced by η_0 ($\eta_0 >> \eta_g$, since $M_{1A} << 1$). Consequently the relevant discussion on Equation (7-21) can be generalized to include Equation (8-17). If we define $\eta^* = (P_d + \rho_1 V_0 V_{xd})/\rho_1 V_0^2$, then the condition (7-17) is generalized as

$$\alpha > \alpha^* = (\eta^* - u^*)/(\eta^* - 2u^*), \tag{8-19}$$

where $1 < \alpha^* < \infty$. The quantity η^* describes the normalized total momentum. For gas dynamic shocks, $\eta^* = \eta_g$, while for MHD shocks, $\eta^* = \eta_o$. The quantity u^* is the solution of the equilibrium equation

$$\rho_1 Q(T)/H_c - u = 0. \tag{8-20}$$

Again, according to condition (8-19), when the piecewise α is chosen for the over-all fitting with $Q(T)$, the downstream equilibrium can not be approached when $T > T_c$. When $T < T_c$, $\alpha = 2$, Equation (8-20) becomes:

$$u(\eta_0 - u)^2 = (T_1 R/V_0^2)^2. \tag{8-21}$$

The expected equilibrium velocity is estimated by using $\eta_o >> 1$ and $u < 1$ as

$$u^* = u_{-\infty} = u_2 \approx [T_1 R/(\eta_0 V_0^2)]^2 = [\beta_1/(\beta_1 + 2M_{1A}^2 + \sin^2\varphi_1)]^2 \approx \beta_1^2,$$

and the equilibrium temperature T_2 is:

$$T_2 = u_2(\eta_0 - u_2)V_0^2/R \approx \beta_1 T_1.$$

The above equilibrium temperature T_2 is estimated for the data in Table 1:

$$T_2 \approx \beta_1 T_1 = 3.47\text{x}10^{-4}\,\text{x}\,2\,\text{x}\,10^4\,\text{K} \approx 7\text{K!}$$

This unrealistically low temperature occurs because we use $\alpha = 2$ to fit with $Q(T)$ for the temperature lower than the critical temperature ($T < T_c$). However, $\alpha = 2$ is no longer appropriate for $T < 2 \times 10^4$ K since α increases more rapidly in that temperature range. A better fit suggested by Peres *et al.*, (1982), that $\alpha = 11.7$ when $4.4 \times 10^3\,\text{K} < T < 8\text{x}10^3\,\text{K}$, gives $T_2 = 5.8 \times 10^3$ K. Therefore, a better over-all fit with $Q(T)$ may be obtained by choosing the more precise power law of T, such as

$$\alpha = 10,\ \tilde{\chi} = 3.9\times10^{-79}, \qquad T < 2\times10^{4}\,\mathrm{K},$$
$$\alpha = 2,\ \tilde{\chi} = 10^{-44}, \qquad 2\times10^{4}\,\mathrm{K} < T < T_c,$$
$$\alpha = -1/2,\ \tilde{\chi} = 10^{-31.5}, \qquad T > T_c.$$

Equation (8-17) can be then combined with above to describe the cooling in the downstream region.

An interesting point worth considering is that the fluid may be heated rather than cooled in the downstream region. It is known that the cooling function $\mathcal{Q}(T)$ reaches a maximum at around 10^5 K (i.e., T_c) and a minimum at around 3×10^7 K (i. e., T_{c1}). Hence $\alpha < 0$ for $T_c < T < T_{c1}$, and $\alpha > 0$ for the temperature outside that range. Since values of $\alpha < 0$ never satisfies condition (8-19), it is impossible for the system to approach the equilibrium when $\alpha < 0$ because of thermal instability. However, when α is sufficiently greater than zero such that condition (8-19) is satisfied, then equilibrium is possible in regions where either $T > T_{c1}$ or $T < T_c$. The equilibrium in the region where $T > T_{c1}$ implies heating of the downstream plasma. Since the subshock formation requires $u_2 < \tilde{C}_{sLd}$, an upper limit for the temperature is

$$T_{max} = T(u = \tilde{C}_{sLd}) \approx T_d X^{1/2}. \tag{8-22}$$

Therefore, radiative heating can occur for $T_{max} > 3 \times 10^7$ K.

Numerical Calculation

Since the subshock is assumed to be located at $\xi = 0$, the equations which govern the shock structure can be summarized as

$$d^2T/d\xi^2 + dT/d\xi - (\gamma-1)\,R_L\,u_c[\rho_1\mathcal{Q}(T)/H_C - 1] = 0, \qquad \xi > 0, \tag{8-23a}$$

$$\frac{d^2}{d\xi^2}[u(\eta_0-u)] + [\gamma\eta_0 - (\gamma+1)u]\frac{du}{d\xi} - (\gamma-1)\,R_L\frac{u_c}{u}\left[\frac{\rho_1\mathcal{Q}(T)}{u\,H_C} - 1\right] = 0, \quad \xi < 0 \tag{8-23b}$$

In order to solve Equations (8-23), we have to first calculate the necessary IBC's because $u(\xi)$ and $T(\xi)$ cannot be integrated numerically from $-\infty$ or ∞. The numerical calculation has to start from the subshock, i. e., $\xi = 0$.

Let $\xi = 0^+$ and $\xi = 0^-$ denote the upstream and the downstream edges of the isothermal subshock. The following equations are obtained by integrating Equations (8-23*a*) and (8-23*b*) from $\xi = 0^+$ to ∞, and $\xi = -\infty$ to 0^-, respectively:

$$Q_{ms} + R_{cu} = \left[X\beta_1 - \left(1 + \cos^2\varphi_1 - 2\cos^2\varphi_1 / X + \beta_1\right)\right] / \left(2X M_{1A}^2\right), \tag{8-24a}$$

$$Q_{md} - R_{cd} = (u_2 - 1/X)\left[\gamma\eta_0 - (u_2 + 1/X)(\gamma + 1)/2\right], \tag{8-24b}$$

Equation (8-12) can be rewritten as ($I_0 = Q_{md} + R_{cu}$)

$$Q_{md} + R_{cu} = \left[\beta_1\gamma + \gamma - 1 - \gamma(\beta_1 + 1 + \cos^2\varphi_1)/X + (\gamma+1)\cos^2\varphi_1 / X^2\right] / \left(2M_{1A}^2\right), \tag{8-24c}$$

where $Q_m = dT/d\xi$ is the normalized heat flux($\kappa\nabla T$) with T expressed in units of V_0^2/R, R_{cu} and R_{cd} are the energy losses due to radiation in the foreshock and cooling regions, respectively:

$$R_{cu} = \int_{0^+}^{\infty} (\gamma - 1)\, R_L\, u_c\left[\rho_1 Q(T)/H_c - 1\right] d\xi, \tag{8-25a}$$

$$R_{cd} = \int_{-\infty}^{0^-} (\gamma - 1)\, R_L \frac{u_c}{u}\left[\rho_1 Q(T)/(uH_c) - 1\right] d\xi. \tag{8-25b}$$

Equations (8-24) are not enough to determine the five unknowns X, R_{cu}, R_{cd}, Q_{ms} and Q_{md}, which are needed to solve $T(\xi)$ in the upstream region and $u(\xi)$ in the downstream region. Thus to obtain additional constraints we rewrite Equations (8-23) as

$$\frac{dQ_m}{du} + \gamma\eta_0 - (\gamma + 1)u - (\gamma - 1)R_L u_c\left[\frac{(\eta_0 - u)^2}{T_1^2} - \frac{1}{u}\right]\frac{\eta_0 - 2u}{Q_m} = 0, \quad u_2 < u < u_d,$$

$$\frac{dQ_m}{dT} + 1 - (\gamma - 1)R_L \frac{u_c}{Q_m}\left[\left(\frac{T}{T_1}\right)^2 - 1\right] = 0, \qquad T_1 < T < T_d,$$

where the piecewise α with two components has been used to fit $Q(T)$. Two initial conditions can then be drawn by taking the limit $u \to u_2$ and $T \to T_1$ in the above two equations, namely,

$$\left.\frac{dQ_m}{du}\right|_2 = \frac{(\gamma+1)u_2 - \gamma\eta_0}{2} + \sqrt{\frac{[\gamma\eta_0 - (\gamma+1)u_2]^2}{4} + (\gamma-1)R_L u_c \frac{(\eta_0 - 2u_2)(\eta_0 - 3u_2)}{u_2 T_2}}, \quad (8\text{-}26a)$$

$$\left(\frac{dQ_m}{dT}\right)_1 = -\frac{1}{2}\left[1 + \sqrt{1 + 8(\gamma-1)R_L \frac{u_c}{T_1}}\right]. \quad (8\text{-}26b)$$

To determine Q_{md} and Q_{ms}, Equation (8-23*a*) is integrated from $u = u_2$, $Q_m = 0$ to $u = u_d$, $Q_m = Q_{md}$, while Equation (8-23*b*) is integrated from $T = T_1$, $Q_m = 0$ to $T = T_s$, $Q_m = Q_{ms}$. These coupled equations are solved iteratively until the values converge. Once Q_{md} and Q_{ms} are known, X, R_{cu} and R_{cd} can be obtained from Equations (8-24). In turn $u(\xi)$ and $T(\xi)$ can be calculated by integrating Equations (8-23*a*) and (8-23*b*) from the subshock towards the downstream and the upstream regions.

In Figure 27, we plot an example of the structure of a radiative slow shock from the far upstream region through to the far downstream region. When compared with the shock solution with no radiation ($R_L = 0$, shown by the dashed curve), the figure shows that the radiation in the downstream region is much stronger than it is in the upstream region. Apparently this occurs because downstream of the subshock the density is much higher. Due to the switch-off limit, the radiation has almost no effect on the pressure and the tangential components of the velocity and the field, though it does substantially change the temperature, the density, and the normal velocity in the downstream region.

Figure 28 shows the variation of the magnetic, kinetic and internal energy through the shock and the downstream cooling region. Also shown are the plasma parameter,

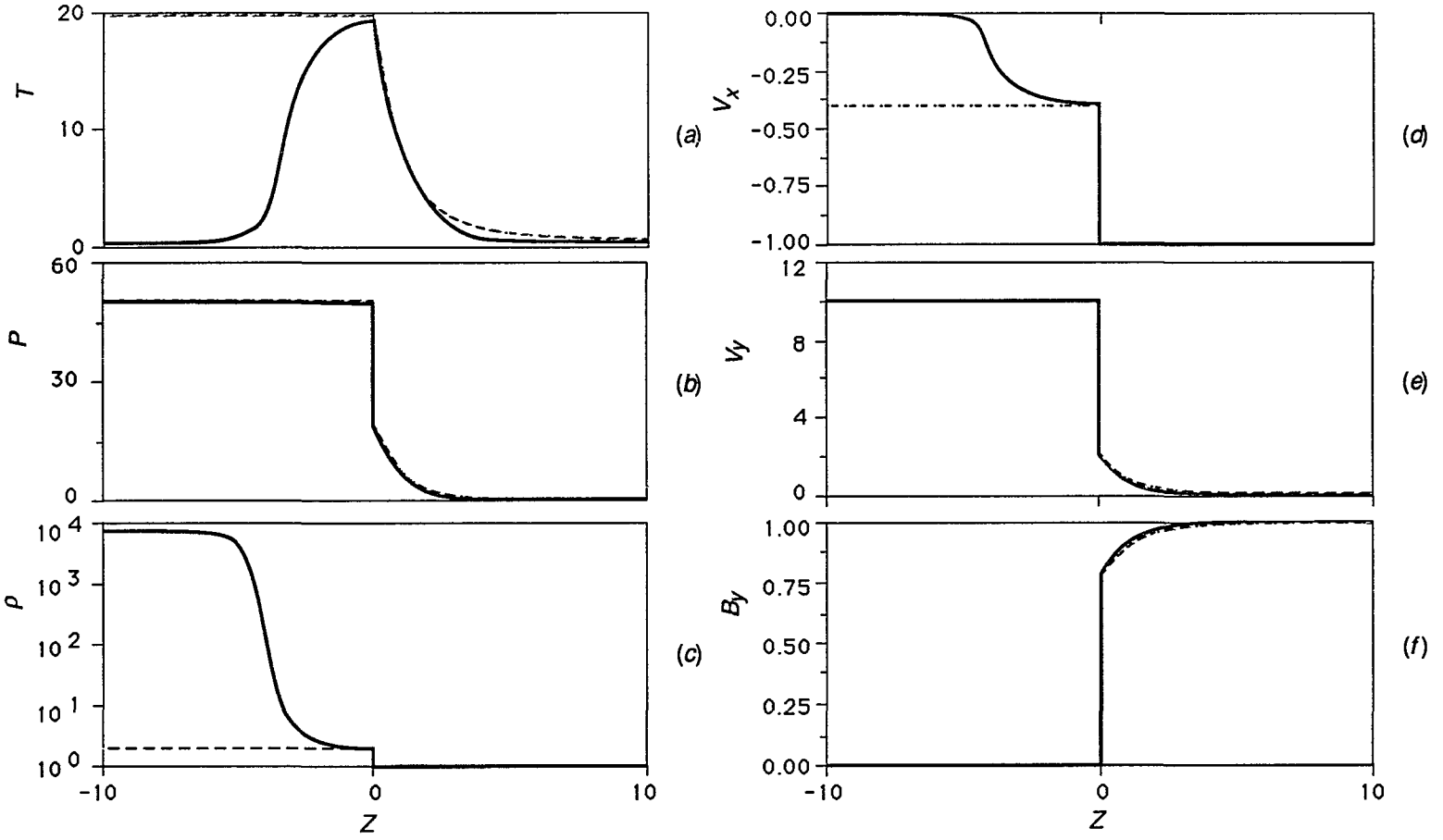

Fig. 27. A numerical solution of an MHD switch-off shock. From (a) to (f), T, P, ρ, V_x, V_y, B_y are in the units of V_0^2/R, $\rho_1 V_0^2$, ρ_1, V_0, V_0 and B_{y1}, respectively. The Alfvén Mach number $M_{1A} = \cos\varphi_1 = 0.1$, $\beta_1 = 3.47 \times 10^{-4}$, and $R_L = 1$, where a 3-component-α fit has been used for $Q(T)$. Solutions with no radiation ($R_L = 0$) are shown by the dashed curves.

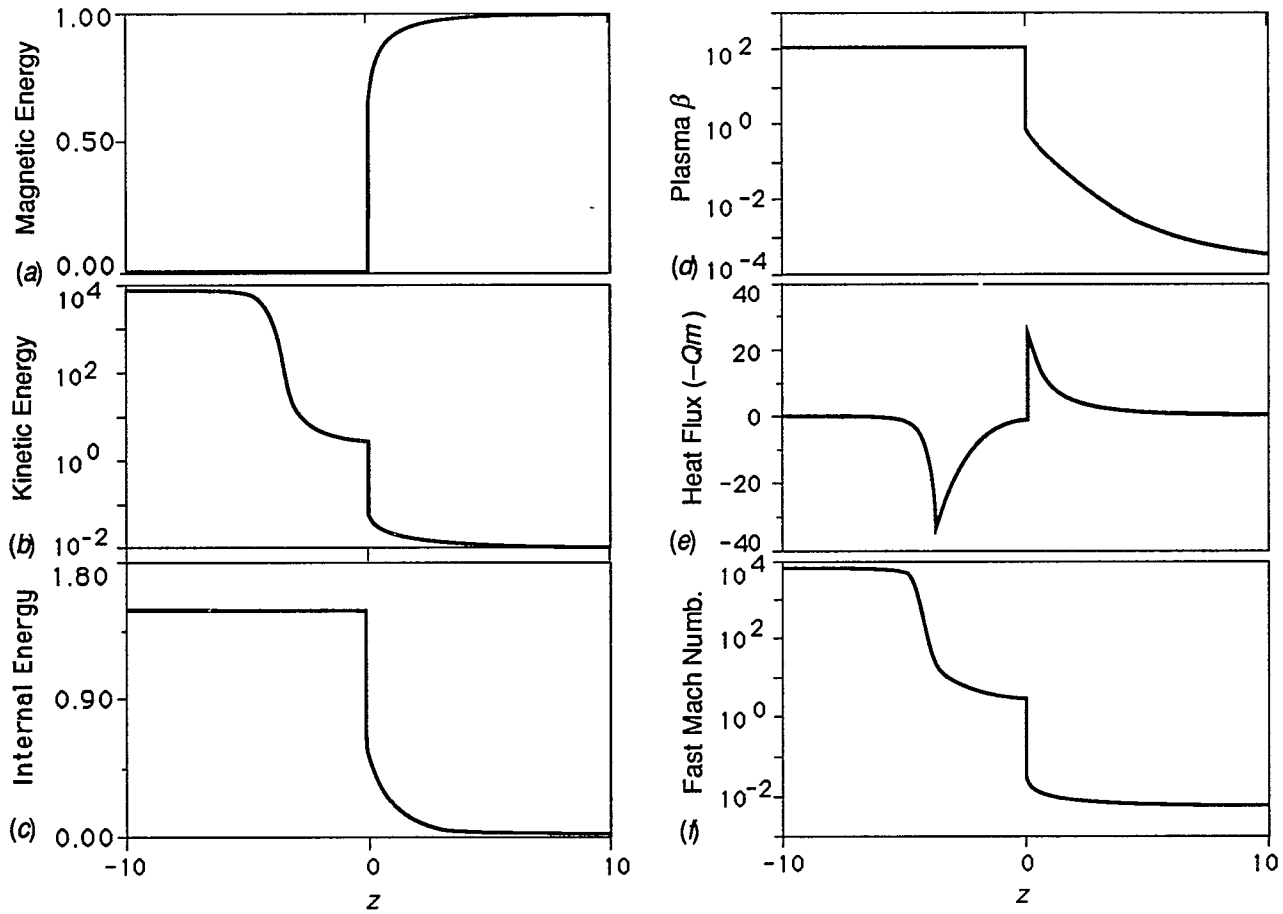

Fig. 28. Various physical quantities across the total transition layer: (a) magnetic energy $B^2/2\mu$; (b) kinetic energy $\rho(V_x^2+ V_y^2)/2$; (c) internal energy $P/(\gamma- 1)$; (d) plasma β; (e) heat flux – Q_m; (f) fast Mach number V^2/C_f^2, where the unit of the heat flux is V_0^2/RL_*, and all the energies are normalized by the upstream total energy. The upstream parameters are the same as in Fig. 27.

the heat flux, and the fast-mode Mach number. The fast-mode Mach number is important for determining whether the out flow from the reconnection in the corona can produce supermagnetosonic jets. If such jets exist they will produce termination shocks which may serve as sites for particle acceleration (Forbes et al., 1989). The effect of the radiation is to greatly increase the Mach number to extremely high values ($\sim 10^4$). Normally this Mach number is about 1.7 (for $\gamma = 5/3$) in the absence of the radiation.

To show how the shock structure varies with the strength of the radiative loss, we plot the temperature jump across the total shock transition. As shown in Figure 29, the temperature is nearly constant as, R_L, the ratio of radiation to conduction scale lengths increases. However, at R_L near 1, the temperature jump suddenly decreases (note that the examples shown in Figures 27 and 28 for $R_L = 1$ are just to the left of where this sudden decrease occurs. This sudden decrease is due to the fact that for $R_L > 1$, the radiative scale length becomes smaller than the thermal conduction scale length. When this happens, the radiation loss is greater than the thermal energy (converted from magnetic energy by slow-mode shocks) available in the total shock transition, and more energy has to be drawn from the inflow plasma by greatly changing the structure of the shock. Thus the sudden transfer of the curve from nearly horizontal to steep falling at $R_L = 1$ suggests that the shock is nearly getting destroyed when the characteristic length of radiative cooling is less than the thermal scale length.

Summary

In the presence of strong thermal conduction an MHD slow shock dissociates into a foreshock, which is dominated by heat-flux transport, and an isothermal subshock, which is dominated by viscous dissipation. The addition of radiation creates a third region immediately downstream of the subshock, and in this region radiative cooling dominates. Because of the thermal conduction, the downstream cooling region is

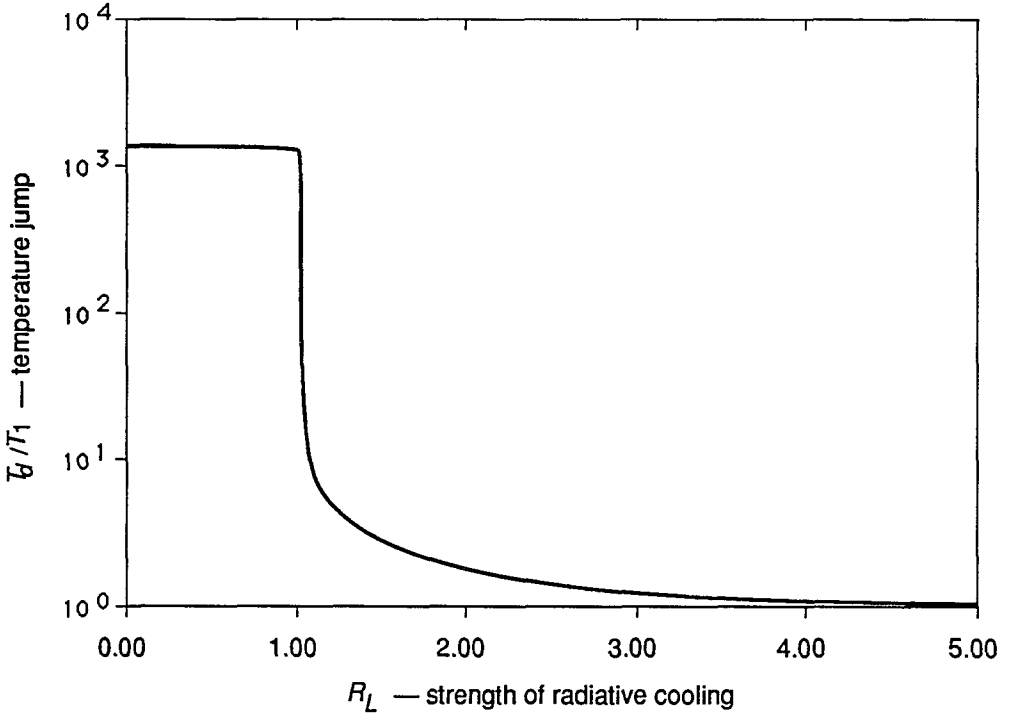

Fig. 29. The temperature jump across the total shock T_d/T_1 vs. R_L, the strength of the radiative cooling. M_{1A}, $\sin\varphi_1$ and β_1 are the same as in Figures 27 and 28.

strongly coupled to the foreshock, and the determination of the shock structure requires simultaneous solution of the equations governing all three regions.

For typical flare conditions, we find that the pressure jump across the total shock transition is nearly equal to β_1^{-1}, where β_1 is the upstream plasma β. The downstream tangential velocity is about the same as the upstream Alfvén speed, and the downstream tangential velocity is supermagnetosonic with respect to the fast-mode wave speed. The tangential magnetic field (normalized by upstream tangential field) at upstream edge of the subshock is close to $(1-1/X)^{1/2}$, where X is the density jump across the total shock. This indicates that of the total energy released by the annihilation of magnetic field, about 1/3 ($\sim 1/X$) is released in the foreshock region while remaining 2/3 ($\sim 1-1/X$) is released at the subshock. Since the thickness of total shock transition is of the order of the scale-size of flare loops, this result suggests that the magnetic energy release occurs not only at the top of the flare loop (where the x-line is), but also throughout the entire length of the loop.

In a previous order-of-magnitude analysis of flare loops, Forbes *et al.*, (1989) assumed that almost all of the energy release occurs in the subshock, and that the thermal energy conducted into the foreshock region was on the order of the radiative loss there. However, our analysis of the structure of slow shocks implies that substantial (up to 1/3) of the energy release occurs in the foreshock region.

Thus, the energy source which heats the flare loops acts partly like a localized source at the top of the loops and partly like a global source distributed throughout the length of the loops. Our analysis also shows that it is the radiative loss in the downstream cooling region rather than the foreshock region, which is of the same order as the energy conducted into the foreshock. Therefore, the balance between the radiative cooling and thermal heating is never reached in the foreshock as assumed by

Forbes et al. (1989). Instead, it should occur in the downstream of the subshock, although we don't know whether this will really be the case in the flare loops, since a full two-dimensional solution will be necessary to determine the correct behavior.

A criterion for equilibrium in the far downstream, i.e., inequality (8-19), has been derived by critical-point analysis. It shows that no stable, steady-state solutions exist for radiative slow shocks unless the temperature in the downstream region of the subshock falls below 10^5 K.

Numerical results indicate that excessively strong radiative cooling could lead to the destruction of the slow-mode shocks. This occurs when the characteristic scale length of radiative cooling becomes smaller than the thermal conduction scale length. However, for typical coronal conditions, the characteristic scale length of radiative cooling is greater than the thermal conduction scale length, and so radiative shocks should exist during a flare.

SUMMARY

This thesis considers two aspects of the reconnection model for large solar flares and related eruptive phenomena. The first part presents a quasi-static analysis of the effect of magnetic reconnection on the evolution of a magnetic field configuration, which can undergo a sudden transition from stable to unstable equilibrium even when reconnection is absent. The second part studies the effect of radiation on the slow-mode MHD shocks produced by magnetic reconnection in the corona.

In the first part of the thesis, we have assumed that the coronal reconnection time scale, τ_r, is much smaller than the photospheric convective motion time scale, τ_p, but much greater than the coronal wave propagation time scale, τ_A (i.e., Alfvén time scale), i.e., $\tau_p >> \tau_r >> \tau_A$. Accordingly, the system evolves quasi-statically via a series of equilibria during a time period of τ_p, until a critical point is reached at which no nearby stable equilibrium is available. During the quasi-static evolution, no current sheet can be formed or sustained, and only at the critical point do current sheets appear. The period starting when the x-type neutral point appears on the photospheric boundary and ending when the system reaches the critical point is identified with the preflare phase.

The MHD equations for the general detached current sheet problem have been solved analytically. The attached current sheet problem previously considered by Forbes and Isenberg (1991) is a special limiting case of the detached problem, and the corresponding asymptotic solutions become identical as the filament radius $r \rightarrow 0$.

Unlike any previous analyses, our analysis here distinguishes between equilibrium losses due to ideal-MHD processes and those due to non-ideal-MHD processes. If the free

magnetic energy of the system is greater than certain critical value before the loss of the magnetohydrostatic equilibrium, then a catastrophic eruption (i.e., ideal-MHD jump) occurs, and a current sheet develops rapidly during the eruption. This current sheet is destroyed during the reconnection jump (non-ideal) after the eruption. However, if the system cannot acquire enough energy (exceeding the critical value), no catastrophe occurs. If an ideal-loss of equilibrium does not occur, then the system undergoes a reconnection jump during which the energy release occurs on the reconnection time scale.

The critical value of the energy required for maintaining catastrophe behavior is equivalent to the critical value of the filament radius. Catastrophe occurs when the filament radius is smaller than the critical radius, or equivalently, one can say that catastrophe occurs when the stored energy is greater than the critical energy. In general, the critical radius required in the detached current sheet model is greater than that in the attached case.

The catastrophic eruption caused by the loss of ideal-MHD equilibrium is identified with the impulsive phase at the start of the flash phase of eruptive flare phenomenon. Our result implies that if the filament radius is small enough (say, on the order of 0.1 times the scale of the photospheric field), then a large eruptive flare with an impulsive phase will occur. On the other hand, if the radius is not small enough, then the eruption will occur without an impulsive phase. This later behavior is like what happens in a quiescent prominence eruption.

In the second part of the thesis we have found that the presence of strong thermal conduction dissociates a slow-mode MHD shock into a foreshock and an isothermal subshock. The effect of radiation is to create a third region immediately downstream of the subshock. Because of the thermal conduction, the downstream cooling region is

strongly coupled to the foreshock, and the determination of the shock structure requires simultaneous solution of the equations governing all three regions.

For typical flare conditions, we find that the pressure jump across the total shock transition is nearly equal to β_1^{-1}, where β_1 is the upstream plasma β (i.e., the ratio of the gas to magnetic pressure). The downstream tangential velocity is about the same as the upstream Alfvén speed, and the downstream tangential velocity is supermagnetosonic with respect to the fast-mode wave speed. Of the total energy released by the annihilation of the magnetic field, about 1/3 is released in the foreshock region while remaining 2/3 is released at the subshock. Since the thickness of total shock transition is of the order of the scale-size of flare loops, which are created by reconnection during the flare. This result suggests that the magnetic energy release occurs not only at the top of the flare loop where the reconnection site is (i.e., the x-line), but also throughout the entire length of the loop.

Thus, the energy source which heats the flare loops acts partly like a localized source at the top of the loops and partly like a global source distributed throughout the length of the loops. Our analysis also shows that it is the radiative loss in the downstream cooling region rather than the foreshock region, which is of the same order as the energy conducted into the foreshock. Therefore, the balance between the radiative cooling and thermal heating is never reached in the foreshock as assumed by Forbes et al. (1989). Instead, it should occur in the downstream of the subshock. To determine the correct behavior, a full two-dimensional solution will be necessary.

According to the criterion for equilibrium in the far downstream, no stable, steady-state solutions exist for radiative slow-mode MHD shocks unless the temperature in the downstream region of the subshock falls below 10^5 K.

Numerical results indicate that excessively strong radiative cooling could lead to the destruction of the slow-mode shocks. This occurs when the characteristic scale length of radiative cooling becomes smaller than the thermal conduction scale length. However, for typical coronal conditions, the characteristic scale length of radiative cooling is greater than the thermal conduction scale length, and so the radiative shocks should exist during a flare.

APPENDICES

Appendix A

Some Mathematics Involved in the Current Sheet Problem

In this appendix the solution of the singular integral equation (3-14) will be derived. More detailed discussion is found in § 17, § 88, and relevant sections of Muskhelishvili (1953). Also presented are some integral results which are useful in simplifying the obtained solutions.

The singular integral equation to be solved is

$$f(t) = \frac{1}{i\pi}\int_L \frac{\varphi(t)\,dt}{t-t_0}, \qquad \text{on } L, \tag{A-1}$$

where L is a segment of the real axis of the complex plane (t, η), $f(t)$ is a known function of t, and $\varphi(t)$ is the unknown function to be found. Some other notations are defined as follows: C— the contour enclosing the upper half complex plane; L'— the remaining part of C excluding L; Z— any point of the plane not lying on C; t— any point on C; t_0 — some point on L, $a < t_0 < b$, a and b are the two ends of L. The unknown function $\varphi(t)$ is assumed continuous on L (may excluding the ends where $\varphi(t)$ is bounded), and to satisfy $\varphi(\infty) = 0$.

The Plemelj Formula

Now consider a sectionally holomorphic function $\Phi(Z)$, defined as

$$\Phi(Z) = \frac{1}{2\pi i}\int_L \frac{\varphi(t)\,dt}{t-Z}. \tag{A-2}$$

According to Cauchy integral formula, if L is a closed contour, i.e., $L = C$, then

$$\Phi(Z) = \frac{1}{2\pi i}\int_L \frac{\varphi(t)\,dt}{t-Z} = \frac{1}{2\pi i}\oint_c \frac{\varphi(t)\,dt}{t-Z} = \frac{1}{2\pi i}\oint_c \frac{\varphi(t)-\varphi(t_0)}{t-Z}dt + \frac{\varphi(t_0)}{2\pi i}\oint_c \frac{dt}{t-Z}$$

$$= \begin{cases} \varphi(t_0) + \dfrac{1}{2\pi i}\oint_c \dfrac{\varphi(t)-\varphi(t_0)}{t-Z}dt, & Z \text{ in upper half plane,} \\ \dfrac{1}{2\pi i}\oint_c \dfrac{\varphi(t)-\varphi(t_0)}{t-Z}dt, & Z \text{ in lower half plane,} \end{cases} \tag{A-3}$$

Let $\Phi^+(t_0)$ and $\Phi^-(t_0)$ denote respectively the limits of $\Phi(Z)$ when Z tends to point t_0, which is on L, from left of L (i.e., the upper half of Z plane) and right of L (i.e., the lower half of Z plane). Apparently, $\Phi(Z)$ tends to $\Phi^+(t_0)$ and $\Phi^-(t_0)$ uniformly when Z tends to point t_0 from left and right of L, respectively, thus

$$\begin{cases} \Phi^+(t_0) = \varphi(t_0) + \dfrac{1}{2\pi i}\oint_c \dfrac{\varphi(t)-\varphi(t_0)}{t-t_0}dt, \\ \Phi^-(t_0) = \dfrac{1}{2\pi i}\oint_c \dfrac{\varphi(t)-\varphi(t_0)}{t-t_0}dt. \end{cases} \tag{A-4}$$

Notice that

$$\frac{1}{2\pi i}\oint_c \frac{dt}{t-t_0} = \frac{1}{2}, \text{ and } \oint_c \frac{\varphi(t)\,dt}{t-t_0} = \int_L \frac{\varphi(t)\,dt}{t-t_0},$$

hence

$$\begin{cases} \Phi^+(t_0) = \dfrac{\varphi(t_0)}{2} + \dfrac{1}{2\pi i}\oint_L \dfrac{\varphi(t)\,dt}{t-t_0}, \\ \Phi^-(t_0) = -\dfrac{\varphi(t_0)}{2} + \dfrac{1}{2\pi i}\oint_L \dfrac{\varphi(t)\,dt}{t-t_0}, \end{cases} \tag{A-5a}$$

or

$$\begin{cases} \Phi^+(t_0) - \Phi^-(t_0) = \varphi(t_0), \\ \Phi^+(t_0) + \Phi^-(t_0) = \dfrac{1}{\pi i}\oint_L \dfrac{\varphi(t)\,dt}{t-t_0}. \end{cases} \tag{A-5b}$$

The above formula is known as the Plemelj formula. It holds even if L is not a contour but only a part of a contour, such as an arc or a union of arcs. It can be proved similarly by setting $\Phi(t) \equiv 0$ for t on L'.

Solution of the Singular Integral Equation

According to the Plemelj formula (A-5*b*), the original singular integral equation (A-1) corresponds to the boundary value problem of finding $\Phi(Z)$ which satisfies the boundary condition

$$\Phi^+(t_0) + \Phi^-(t_0) = f(t_0), \quad \text{on } L, \tag{A-6}$$

where $\Phi(Z)$ is the sectionally holomorphic function defined in Equation (A-2).

The problem represented by Equation (A-6) is a non-homogeneous Hilbert problem. The corresponding homogeneous H-problem is to find a function $\Phi_0(Z)$ satisfying

$$\Phi^+(t_0) + \Phi^-(t_0) = 0, \quad \text{on } L, \tag{A-7}$$

or

$$\Phi^+(t_0)/\Phi^-(t_0) = -1, \quad \text{on } L. \tag{A-7'}$$

We next substitute $\Psi_0(Z) = \ln\Phi_0(Z)$ into equation (A-7'), where the proper branch of $\ln\Phi_0(Z)$ is below the branch cut along L, then

$$\Psi_0^+(t_0) - \Psi_0^-(t_0) = \ln(-1) = \pi i, \quad \text{on } L, \tag{A-8}$$

According to Equation (A-2) and the Plemelj formula, it is clear that

$$\Gamma(Z) = \frac{1}{2\pi i}\int_L \frac{\pi i}{t - Z}\,dt = \frac{1}{2}\ln\frac{Z-b}{Z-a} \tag{A-9}$$

satisfies the above boundary condition, and thus it is a particular solution of Equation (A-8), i.e.,

$$e^{\Gamma(z)} = i\sqrt{(b - Z)\,(Z - a)}$$

is a particular solution of Equation (A-7). Apparently, the general solution of Equation (A-7) can be written as $X_0(Z)P(Z)$, where $P(Z)$ is an arbitrary polynomial, $X_0(Z) = (Z-a)e^{\Gamma(z)}$ is the solution of Equation (A-7), and $X_0(Z)$ is bounded at both ends of L (i.e., $Z = a$, and $Z = b$). By using the Plemelj formula, we have

$$X_0^+(t_0) = \sqrt{(b-t_0)(t_0-a)} = -X_0^-(t_0). \tag{A-10}$$

Returning to the non-homogeneous H-problem (A-6), we substitute (A-10) to obtain

$$\Phi^+(t_0) = -\Phi^-(t_0) + f(t_0) = \Phi^-(t_0)X_0^+(t_0)/X_0^-(t_0) + f(t_0), \quad \text{on } L,$$

i.e.,

$$\Phi^+(t_0)/X_0^+(t_0) - \Phi^-(t_0)/X_0^-(t_0) = f(t_0)/X_0^+(t_0), \quad \text{on } L. \tag{A-11}$$

A homogeneous H-problem is immediately obtained by setting $\Psi(Z) = \Phi(Z)/X_0(Z)$, i.e.,

$$\Psi^+(t_0) - \Psi^-(t_0) = f(t_0)/X_0^+(t_0), \quad \text{on } L. \tag{A-12}$$

The general solution of the above equation is readily written down by using equations (A-2) and (A-5*a*)

$$\Psi(Z) = \frac{1}{2\pi i}\int_L \frac{f(t)\,dt}{X_0^+(t)(t-Z)} + P(Z), \tag{A-13}$$

or

$$\Phi(Z) = \frac{X_0(Z)}{2\pi i}\int_L \frac{f(t)\,dt}{X_0^+(t)(t-Z)} + P(Z)\,X_0(Z). \tag{A-14}$$

Therefore, the solution of the original singular integral equation (A-1) is obtained by using the Plemelj formula (A-5*b*) once more. That is

$$\varphi(t_0) = \Phi^+(t_0) - \Phi^-(t_0) = \frac{X_0^+(t_0)}{\pi i}\int_L \frac{f(t)\,dt}{X_0^+(t)(t-t_0)} + 2P(t_0)\,X_0^+(t_0). \tag{A-15}$$

Similarly, if we allow the unknown function $\varphi(t)$ to be unbounded at either end of L, or unbounded at both ends of L, the corresponding solutions are

$$\varphi_j(t_0) = \frac{X_j^+(t_0)}{\pi i}\int_L \frac{f(t)\,dt}{X_j^+(t)\,(t-t_0)} + 2P_j(t_0)\,X_j^+(t_0)\,, \quad j = 1,2,3, \tag{A-16}$$

where

$$X_1^+(t_0) = \sqrt{(b-t_0)/(t_0-a)}, \tag{A-17a}$$

$$X_2^+(t_0) = \sqrt{(t_0-a)/(b-t_0)}, \tag{A-17b}$$

$$X_1^+(t_0) = 1/\sqrt{(b-t_0)(t_0-a)}, \tag{A-17c}$$

and $\varphi_1(t_0)$, $\varphi_2(t_0)$, and $\varphi_3(t_0)$ are solutions unbounded at $t_0 = a$, $t_0 = b$, and at both ends of L, respectively.

Some Useful Integrals

$$\int_p^q \frac{1}{\sqrt{(q^2-v^2)(v^2-p^2)}}\frac{v\,dv}{v^2-y^2} = 0, \quad p<y<q, \tag{A-18a}$$

$$\int_p^q \frac{\sqrt{(q^2-v^2)(v^2-p^2)}}{h^2-v^2}\,v\,dv = \int_p^q \sqrt{\frac{v^2-p^2}{q^2-v^2}}\left(1-\frac{h^2-q^2}{h^2-v^2}\right)v\,dv$$
$$= \frac{\pi}{4}\left(\sqrt{h^2-p^2}-\sqrt{h^2-q^2}\right)^2, \tag{A-18b}$$

$$\int_p^q \frac{\sqrt{(q^2-v^2)(v^2-p^2)}}{u^2+v^2}\,v\,dv = \int_p^q \sqrt{\frac{q^2-v^2}{v^2-p^2}}\left(1-\frac{p^2+u^2}{u^2+v^2}\right)v\,dv$$
$$= \frac{\pi}{4}\left(\sqrt{u^2+q^2}-\sqrt{u^2+p^2}\right)^2, \tag{A-18c}$$

$$\int_p^q \frac{\sqrt{(q^2-v^2)(v^2-p^2)}}{v^2-y^2}\,v\,dv = \int_p^q \sqrt{\frac{q^2-v^2}{v^2-p^2}}\,v\,dv - \int_p^q \frac{(y^2-p^2)\,v\,dv}{\sqrt{(q^2-v^2)(v^2-p^2)}}$$
$$+\int_p^q \frac{(q^2-y^2)(y^2-p^2)}{\sqrt{(q^2-v^2)(v^2-p^2)}}\frac{v\,dv}{v^2-y^2}$$

$$= \frac{\pi}{4}(q^2 + p^2 - 2y^2) + \begin{cases} -\frac{\pi}{2}\sqrt{(q^2 - y^2)(p^2 - y^2)}, & 0 \le y < p, \\ 0, & p < y < q, \\ \frac{\pi}{2}\sqrt{(y^2 - p^2)(y^2 - q^2)}, & y > q. \end{cases} \qquad \text{(A-18}d\text{)}$$

The Integral Involving Elliptic Integral Functions

By using transformation $t = q/\sqrt{u^2 + q^2}$, the last term in equation (3-18b) can be expressed by the complete elliptic integrals:

$$\frac{2}{\pi}\int_{-\infty}^{\infty} \frac{\sqrt{(u^2 + p^2)(u^2 + q^2)}}{(u^2 + y^2)(u^2 + 1)^2} u^2 du$$

$$= \frac{4}{\pi q}\int_0^1 \frac{\sqrt{(1 - t^2)[1 - t^2(1 - p^2/q^2)]}\, dt}{[1 + t^2(y^2/q^2 - 1)][1 - t^2(1 - 1/q^2)]^2}$$

$$= \frac{2}{\pi q}\left\{ \frac{q^2}{y^2 - 1}\left[\frac{p^2 - 1}{q^2 - 1}K(k) - E(k)\right] + 2\frac{(y^2 - p^2)y^2}{(y^2 - 1)^2}\Pi\left(\frac{y^2}{q^2} - 1, k\right) \right.$$

$$\left. + \frac{1}{(y^2 - 1)^2}\left[y^2(p^2 - 2) + \frac{y^2 - 1}{q^2 - 1} - p^2\frac{y^2 - q^2}{q^2 - 1}\right]\Pi\left(\frac{1}{q^2} - 1, k\right)\right\}. \qquad \text{(A-19)}$$

where $k^2 = 1 - p^2/q^2$, K, E, and Π are the complete elliptic integrals of the first, the second, and the third kind, respectively.

Appendix B

Boundary Layer Analysis

Following the argument and discussion in Chapter 7, we present the derivations leading to solutions (7-7) and (7-8). After substituting Equations (7-4) into Equations (7-6) and normalizing, we obtain

$$\delta\rho = \delta u/(1-\delta u), \tag{B-1a}$$

$$\delta P = \delta u + \frac{\lambda_v}{\delta u}\frac{d\delta u}{d\xi_0}, \tag{B-1b}$$

$$\delta T = \frac{\gamma-1}{\gamma}\delta u + \delta u\left(\frac{\gamma+1}{2\gamma}\delta u_d - \delta u\right) + \lambda_v\frac{d\delta u}{d\xi_0}, \tag{B-1c}$$

$$-\frac{\gamma+1}{2}\frac{d}{d\xi_0}[\delta u(\delta u_d - \delta u)] = \frac{d}{d\xi_0}\left(\lambda_v\frac{d\delta u}{d\xi_0} + \lambda_\kappa\frac{d\delta T}{d\xi_0}\right), \tag{B-1d}$$

where $\delta\rho = (\rho-\rho_1)/\rho_1$, $\delta P = (P-P_1)/\rho_1 V_0^2$, $\delta T = (T-T_1)R/V_0^2$, $\delta u = v/V_0$, and $\xi_0 = Z/L$, $\lambda_v = L_v/L$, $\lambda_\kappa = L_\kappa/L$, and L denotes the global scale length of the system. The associated boundary conditions are:

$$\delta u|_1 = 0, \tag{B-2a}$$

$$\delta u|_d = \delta u_d = (V_0 - V_d)/V_0, \tag{B-2b}$$

and

$$(d\delta u/d\xi_0)|_1 = (d\delta u/d\xi_0)|_d = 0. \tag{B-2c}$$

Burger's Equation and Solution

An approximate solution of δu can then be derived from Equations (B-1) by setting ε as a parameter of smallness and assuming

$$\delta u = o(\varepsilon),\ L_v/L_\kappa = o(\varepsilon) \text{ and } L_\kappa/L = o(\varepsilon). \tag{B-3}$$

Accordingly the order of each term in Equation (B-1*c*) and (B-1*d*) is shown as follows,

$$\text{Terms in Eq.:} \quad \delta T = \frac{\gamma - 1}{\gamma}\delta u + \delta u\left(\frac{\gamma + 1}{2\gamma}\delta u_d - \delta u\right) + \lambda_v \frac{d\delta u}{d\xi_0}$$

$$\text{Order of } \varepsilon \qquad \varepsilon \qquad \varepsilon \qquad\qquad \varepsilon^2 \qquad\qquad \varepsilon^3 \ ,$$

$$\text{Terms in Eq.:} \quad -\frac{\gamma + 1}{2}\frac{d}{d\xi_0}[\delta u\,(\delta u_d - \delta u)] = \frac{d}{d\xi_0}\left(\lambda_v \frac{d\delta u}{d\xi_0} + \lambda_\kappa \frac{d\delta T}{d\xi_0}\right)$$

$$\text{Order of } \varepsilon \qquad\qquad \varepsilon^2 \qquad\qquad\qquad \varepsilon^3 \qquad\qquad \varepsilon^2 \ ,$$

where δu is assumed to vary slowly so that its derivatives are not very large. As a matter of fact, this implies weak shocks with no subshocks present.

Substituting Equation (B-1*c*) into Equation (B-1*d*) and taking the leading-order approximation according to the order of ε, then

$$-\frac{\gamma + 1}{2}\frac{d}{d\xi_0}[\delta u\,(\delta u_d - \delta u)] = \frac{\gamma - 1}{\gamma}\lambda_\kappa \frac{d^2\delta u}{d\xi_0^2} \ , \tag{B-4}$$

which is Burger's equation in stationary state (Whitham, 1974). It is solved by integrating Equation (B-4) and using the boundary conditions. That is

$$\delta u = \delta u_d\left[1 + exp\left(\frac{\gamma + 1}{\gamma - 1}\frac{\gamma}{2}\frac{\delta u_d}{\lambda_\kappa}\xi_0\right)\right]^{-1} \ , \tag{B-5}$$

which is the normalized form of Equation (7-7).

Boundary Layer analysis

For a strong shock with a subshock present, a boundary layer, in which derivatives of δu become very large, appears in the vicinity of $\xi_0 = 0\,(z = 0)$, where the subshock is assumed to be located. In order to solve the shock structure in this transition layer, the boundary layer analysis has to be used (for further discussion, see Bender and Orszag, 1978). Inside the boundary layer, the inner variable $\xi_l = \xi_0 / \varepsilon$ is introduced to describe $\delta u_{(in)}$—the inner solution of δu. Substitution of them into Equation (B-1d) gives

$$-\frac{\gamma+1}{2}\frac{d}{d\xi_l}\left[\delta u_{(in)}\left(\delta u_d - \delta u_{(in)}\right)\right] = \frac{d}{d\xi_l}\left(\frac{\lambda_v}{\varepsilon}\frac{d\delta u_{(in)}}{d\xi_l} + \frac{\lambda_\kappa}{\varepsilon}\frac{d\delta T_{(in)}}{d\xi_l}\right), \tag{B-6}$$

On the RHS of Equation (B-6), the last term is of the order ε, while the other two terms are of the order ε^2. This implies that

$$d\delta T_{(in)}/d\xi_l = 0,$$

which indicates that the subshock will be isothermal because $\delta T_{(in)}$ is constant inside the boundary layer. According to Kennel (1987), the isothermal subshock is located at the downstream edge of strong shock, thus the boundary conditions (B-2) become

$$\delta u|_1 = 0, \tag{B-7a}$$

$$\delta u|_{0^-} = \delta u_d, \tag{B-7b}$$

$$\delta u|_{0^+} = \delta u_S = (V_0 - V_S)/V_0, \tag{B-7c}$$

$$(d\delta u/d\xi_0)|_1 = (d\delta u/d\xi_l)|_{0^-} = 0, \tag{B-7d}$$

where

$$0^+ = \lim_{\varepsilon\to 0}\,(0+\varepsilon),\quad 0^- = \lim_{\varepsilon\to 0}\,(0-\varepsilon).$$

Now consider δu in two regions—outer region where δu varies slowly and inner region (boundary layer) where δu varies rapidly.

Outer Solution

In the outer region δu varies slowly. Follow the same procedure as we did in weak shock case and combine with boundary condition (B-7*b*), i.e., $\delta u_{(out)} = \delta u_d$, $\xi_0 < 0^-$, we have

$$-\frac{\gamma+1}{2}\frac{d}{d\xi_0}[\delta u_{(out)}(\delta u_d - \delta u_{(out)})] = \frac{\gamma-1}{\gamma}\lambda_\kappa \frac{d^2\delta u_{(out)}}{d\xi_0^2}, \tag{B-8}$$

for $\xi_0 > 0$. Its solution is readily written down as

$$\delta u_{(out)} = \delta u_d\left[1 + C_{(out)}\exp\left(\frac{\gamma+1}{\gamma-1}\frac{\gamma}{2}\frac{\delta u_d}{\lambda_\kappa}\xi_0\right)\right]^{-1}, \tag{B-9}$$

by Equation (B-5), where $C_{(out)}$ is the constant of integration to be determined.

Inner Solution

Inside the boundary layer, we substitute the isothermal condition $T = T_d$ and the inner variable ξ_i into Equation (B-1*c*) and simplify the result to

$$\frac{\lambda_v}{\varepsilon}\frac{d\delta u_{(in)}}{d\xi_i} = -(\delta u_{(in)} - \delta u_s)(\delta u_d - \delta u_{(in)}), \tag{B-10}$$

where Equations (7-4) have been used. Integration of (B-10) gives

$$\delta u_{(in)} = \delta u_s + (\delta u_d - \delta u_s)\left[1 + C_{(in)}\exp\left(\frac{\delta u_d - \delta u_s}{\lambda_v}\varepsilon\,\xi_i\right)\right]^{-1}, \tag{B-11}$$

where $C_{(in)}$ is the constant of integration.

Matching

Outer and inner solutions must be asymptotically matched in the overlap regions which are defined by the intermediate limits

$$\xi_0 \to 0^+, \quad \xi_l = \xi_0/\varepsilon \to \infty, \quad \varepsilon \to 0,$$

$$\xi_0 \to 0^-, \quad \xi_l = \xi_0/\varepsilon \to -\infty, \quad \varepsilon \to 0.$$

By Equation (B-3), $\delta u_d/\lambda_\kappa = o(\varepsilon^0)$, $(\delta u_d - \delta u_s)\varepsilon/\lambda_v = o(\varepsilon^0)$. Taking the intermediate limits accordingly, we obtain the following conditions:

$$\text{for } \xi_0 \to 0^+, \qquad \delta u_{(out)} \to \delta u_d/(1 + C_{(out)}), \qquad \delta u_{(in)} \to \delta u_s, \tag{B-12a}$$

$$\text{for } \xi_0 \to 0^-, \qquad \delta u_{(out)} \to \delta u_d, \qquad \delta u_{(in)} \to \delta u_d, \tag{B-12b}$$

Therefore,

$$C_{(out)} = (\delta u_d - \delta u_s)/\delta u_s, \tag{B-13}$$

while $C_{(in)}$ is still arbitrary and, can be picked equal to 1.

Combining $\delta u_{(in)}$ and $\delta u_{(out)}$ gives

$$\delta u \approx \delta u_d \left[1 + \frac{\delta u_d - \delta u_s}{\delta u_s} \exp\left(\frac{\gamma+1}{\gamma-1} \frac{\gamma}{2} \frac{\delta u_d}{\lambda_\kappa} \xi_0 \right) \right]^{-1}, \quad 0 < \xi_0 < \infty, \ \varepsilon \to 0, \tag{B-14a}$$

$$\delta u \approx \delta u_s + (\delta u_d - \delta u_s) \left[1 + \exp\left(\frac{\delta u_d - \delta u_s}{\lambda_v} \xi_0 \right) \right]^{-1}, \quad -\infty < \xi_0 \le 0, \ \varepsilon \to 0. \tag{B-14b}$$

These equations can be combined into a single, uniform approximation:

$$\delta u \approx (\delta u_d - \delta u_s) \left[1 + \exp\left(\frac{\delta u_d - \delta u_s}{\lambda_v} \xi_0 \right) \right]^{-1} + \delta u_d \left[1 + \frac{\delta u_d - \delta u_s}{\delta u_s} \exp\left(\frac{\gamma+1}{\gamma-1} \frac{\gamma}{2} \frac{\delta u_d}{\lambda_\kappa} \xi_0 \right) \right]^{-1}, \quad -\infty < \xi_0 < \infty. \tag{B-15}$$

which is the normalized form of Equation (7-8).

Appendix C

Critical-Point Analysis

Autonomous differential equations do not contain explicitly the independent variable . Such an autonomous equation of order n is equivalent to a system of n coupled first-order equations. If the autonomous system is

$$y_i' = f_i(y_1, y_2, \ldots, y_n), \quad i = 1, 2, \ldots, n, \tag{C-1}$$

then the critical points of the system are those points at which all the derivatives vanish simultaneously, i.e., solutions of the algebraic equations

$$y_i' = f_i(y_1, y_2, \ldots, y_n) = 0, \quad i = 1, 2, \ldots, n. \tag{C-2}$$

The approximate behavior of the autonomous system in the neighborhood of a critical point can be predicted by critical-point analysis. A brief study of 1-D and 2-D autonomous systems will be presented below, for further discussion see Bender and Orszag (1978).

Behavior of a 2-D Autonomous System

The two dimensional autonomous system (7-10) can be written as

$$\frac{d\delta u}{d\xi} = R_{UHD}\left[\delta u\left(\delta u - 1 + \frac{1}{\gamma M_1^2}\right) + \delta T\right], \tag{C-3a}$$

$$\frac{d\delta T}{d\xi} = \frac{\gamma - 1}{2}\delta u\left(\delta u + \frac{2}{\gamma M_1^2}\right) - \delta T, \tag{C-3b}$$

the algebraic equations

$$\delta u\,(\delta u - 1 + 1/\gamma M_1^2) + \delta T = 0, \tag{C-4a}$$

$$(\gamma - 1)\delta u\,(\delta u/2 + 1/\gamma M_1^2) - \delta T = 0, \tag{C-4b}$$

give two critical points: **A**. $(\delta u,\ \delta T) = (0, 0)$, and **B**. $(\delta u,\ \delta T) = (\delta u_d,\ \delta T_d)$,corresponding to the upstream and downstream regions, respectively.

Behavior of the System Near Critical Point **A**

Substituting $\delta u = \varepsilon_1$ and $\delta T = \varepsilon_2$ into Equations (C-3) and linearizing them by letting $\varepsilon_1 \to 0$, $\varepsilon_2 \to 0$, we get

$$\frac{d\varepsilon_1}{d\xi} \approx R_{LHD}\left[-\left(1 - \frac{1}{\gamma M_1^2}\right)\varepsilon_1 + \varepsilon_2\right], \tag{C-5a}$$

$$\frac{d\varepsilon_2}{d\xi} \approx \frac{\gamma - 1}{\gamma M_1^2}\varepsilon_1 - \varepsilon_2 . \tag{C-5b}$$

Solution of the linear differential equations (C-5) determines the behavior of the system near the critical point $(\delta u,\ \delta T) = (0, 0)$. That is

$$\varepsilon_1 = C_+ \exp(\kappa_+ \xi) + C_- \exp(\kappa_- \xi), \tag{C-6a}$$

$$\varepsilon_2 = C_+' \exp(\kappa_+ \xi) + C_-' \exp(\kappa_- \xi), \tag{C-6b}$$

where

$$k_\pm = \frac{-1 - R_{LHD}\left(1 - \frac{1}{\gamma M_1^2}\right) \pm \sqrt{\left[1 - R_{LHD}\left(1 - \frac{1}{\gamma M_1^2}\right)\right]^2 + \frac{4R_{LHD}}{\gamma M_1^2}(\gamma - 1)}}{2}$$

$$= \frac{-1 + R_{LHD}\left(1 - \frac{1}{\gamma M_1^2}\right) \pm \sqrt{\left[1 + R_{LHD}\left(1 - \frac{1}{\gamma M_1^2}\right)\right]^2 - 4R_{LHD}\left(1 - \frac{1}{M_1^2}\right)}}{2}, \tag{C-7}$$

and C_+, C_-, C_+', C_-' are the constants of integration.

Since $k_+ < 0$, $k_- < 0$, apparently $\varepsilon_1 \to 0$, $\varepsilon_2 \to 0$ as $\xi \to \infty$, hence the critical point (δu, δT) = (0, 0) is a stable node. In the phase space of (δu, δT), all trajectories of $\delta T(\delta u)$ near the critical point (0, 0) will approach it as $\xi \to \infty$.

Behavior of the System Near Critical Point **B**

In the neighborhood of point **B**, substituting $\delta u = \delta u_d + \varepsilon_1$ and $\delta T = \delta T_d + \varepsilon_2$ into Equation (C-3) and linearizing by letting $\varepsilon_1 \to 0$, $\varepsilon_2 \to 0$, gives

$$\frac{d\varepsilon_1}{d\xi} \approx R_{LHD}\left[\left(2\delta u_d - 1 + \frac{1}{\gamma M_1^2}\right)\varepsilon_1 + \varepsilon_2\right], \tag{C-8a}$$

$$\frac{d\varepsilon_2}{d\xi} \approx (\gamma - 1)\left[\left(\delta u_d + \frac{1}{\gamma M_1^2}\right)\varepsilon_1 - \varepsilon_2\right]. \tag{C-8b}$$

Solution of Equations (C-8) gives

$$\varepsilon_1 \approx C_+ \exp(\omega_+ \xi) + C_- \exp(\omega_- \xi), \tag{C-9a}$$

$$\varepsilon_2 \approx C_+' \exp(\omega_+ \xi) + C_-' \exp(\omega_- \xi), \tag{C-9b}$$

where

$$\omega_\pm = \frac{F_0 \pm \sqrt{F_0^2 + 4R_{LHD}\left(1 - \frac{1}{M_1^2}\right)}}{2}, \tag{C-10}$$

and

$$F_0 = R_{LHD}\left(2\delta u_d - 1 + \frac{1}{\gamma M_1^2}\right) - 1. \tag{C-11}$$

Since $\omega_+ > 0$, $\omega_- < 0$, the critical point **B** is necessarily a saddle point near which the trajectories will approach it in a specific direction and move away from it in the other direction as $\xi \to -\infty$.

Asymptotic Behavior of Trajectories

Equations (C-3) can be transformed into

$$\frac{d\delta T}{d\delta u} = \frac{1}{R_{LHD}} \frac{(\gamma - 1)\,\delta u(\delta u/2 + 1/\gamma M_1^2) - \delta T}{\delta u(\delta u - 1 + 1/\gamma M_1^2) + \delta T} \quad . \tag{C-12}$$

The asymptotic slope of the trajectories approaching the critical points and the infinity is derived as follows:

For $(\delta u, \delta T) \rightarrow (0, 0)$, if $d\delta T/d\delta u \rightarrow W_0$ and W_0 is finite, then by taking the limit in Equation (C-12), we find

$$W_0 = \frac{(\gamma - 1)/\gamma M_1^2 - W_0}{R_{LHD}(W_0 - 1 + 1/\gamma M_1^2)},$$

Since $d\delta T/d\delta u > 0$, the asymptotic slope of the trajectories approaching (0, 0) is

$$W_0 = 1 - \frac{1}{\gamma M_1^2} + \frac{k_+}{R_{LHD}}, \tag{C-13)}$$

For $(\delta u, \delta T) \rightarrow (\delta u_d, \delta T_d)$, we assume $d\delta T/d\delta u \rightarrow W_d$ and get

$$W_d = \frac{(\gamma - 1)(\delta u_d + 1/\gamma M_1^2) - W_d}{R_{LHD}(W_d + 2\delta u_d - 1 + 1/\gamma M_1^2)}.$$

Thus near the saddle point $(\delta u_d, \delta T_d)$, the asymptotic slope of incoming trajectories is

$$W_{d+} = 1 - 1/\gamma M_1^2 - 2\delta u_d + \omega_+/R_{LHD} \tag{C-14a}$$

while the asymptotic slope of outgoing trajectories is

$$W_{d-} = 1 - 1/\gamma M_1^2 - 2\delta u_d + \omega_-/R_{LHD} \tag{C-14b}$$

For $\delta u \rightarrow \infty$, the asymptotic slope of $\delta T(\delta u)$ is

$$d\delta T/d\delta u \rightarrow W_\infty = (\gamma - 1)/2R_{LHD} \tag{C-15}$$

The above results are sketched in Fig. 21.

Equilibrium Criterion (7-17)

Presented here is the derivation of criterion (7-17) by critical-point analysis. We start by normalizing Equation (7-12) into a 1-D autonomous system:

$$[\gamma\eta_g-(\gamma+1)u]\,du/d\xi = u_c R_L(\gamma-1)[\mathcal{Q}(T)/\mathcal{Q}(T_1)-u]/u^2\,. \tag{C-16}$$

If $u = u^*$ satisfies

$$\mathcal{Q}(T)-u\,\mathcal{Q}(T_1)=0, \tag{C-17}$$

and the appropriate physical conditions are applied, then $u = u^*$ represents the solution to the downstream equilibrium. The stability of this solution can be analyzed by examining the behavior of (C-17) near critical point $u = u^*$ through critical-point analysis. The quantity $\mathcal{Q}(T)$ can be written as

$$\mathcal{Q}(T) = \tilde{\chi}(V_0^2/R)^{\alpha}u^{\alpha}(\eta_g-u)^{\alpha} = C_{\chi}u^{\alpha}(\eta_g-u)^{\alpha}, \tag{C-18}$$

so that Equation (C-17) gives

$$u^{*\alpha-1}(\eta_g-u^*)^{\alpha}=\mathcal{Q}(T_1)/C_{\chi}\,, \tag{C-19}$$

Substituting $u = u^* + \varepsilon$ into Equation (C-16) and linearizing it by letting $\varepsilon \to 0$, we get

$$[\gamma\eta_g-(\gamma+1)u^*]\frac{d\varepsilon}{d\xi} \approx u_c R_L\frac{\gamma-1}{u^*}\left(\frac{\alpha-1}{u^*}-\frac{\alpha}{\eta_g-u^*}\right)\varepsilon\,. \tag{C-20}$$

Therefore, when $\varepsilon \approx 0$,

$$\varepsilon \to \exp\left\{\frac{u_c(\gamma-1)R_L}{u^*[\eta_g-(\gamma+1)u^*]}\left(\frac{\alpha-1}{u^*}-\frac{\alpha}{\eta_g-u^*}\right)\xi\right\}. \tag{C-21}$$

The condition $u \to u^*$ as $\xi \to -\infty$ (in the downstream region) requires

$$(\alpha - 1)/u^* - \alpha/(\eta_g - u^*) > 0, \tag{C-22}$$

i. e.,

$$\alpha(\eta_g - u^*) - \alpha u^* > \eta_g - u^*, \tag{C-23}$$

which is equivalent to criterion (7-17), that is

$$\alpha > (\eta_g - u^*)/(\eta_g - 2u^*).$$

Appendix D

Some Notes on the Numerical Method

Runge-Kutta Formula

The numerical solutions in this thesis are computed by the standard Runge-Kutta algorithm. All the problems to be solved numerically are converted to initial-value problems of the first order differential equations, i.e.,

$$y_i' = f_i(\xi, y_1, y_2, \ldots, y_n), \tag{D-1}$$

with initial conditions

$$y_i(\xi = 0) = y_{i0} \quad (i = 1, 2, \ldots, n). \tag{D-2}$$

The numerical integration is then carried out by the fourth-order Runge-Kutta formula, described as follows:

$$y_{i\,m+1} = y_{i\,m} + h(K_{i1} + 2K_{i2} + 2K_{i3} + K_{i4})/6, \tag{D-3}$$

where

$$K_{i1} = f_i(\xi_m, y_{1m}, \ldots, y_{nm}) \tag{D-4a}$$

$$K_{i2} = f_i(\xi_m + h/2, y_{1m} + K_{11}\,h/2, \ldots, y_{nm} + K_{n1}\,h/2) \tag{D-4b}$$

$$K_{i3} = f_i(\xi_m + h/2, y_{1m} + K_{12}\,h/2, \ldots, y_{nm} + K_{n2}\,h/2) \tag{D-4c}$$

$$K_{i4} = f_i(\xi_m + h, y_{1m} + K_{13}\,h, \ldots, y_{nm} + K_{n3}\,h) \tag{D-4d}$$

$$i = 1, 2, \ldots, n; \quad m = 0, 1, 2, \ldots$$

here y_{im} denotes the approximate value of the ith dependent variable y_i at the mth node $\xi_m = mh$, where h is stepsize of the numerical integration.

Iteration Calculation

The critical-point analysis indicates that the solutions satisfying the upstream and downstream equilibrium conditions correspond to two saddle points. The saddle point behavior makes it difficult to solve Equations (8-23) numerically because of the bad convergence properties. Near the saddle point any tiny numerical error drives the numerical result far away from the exact solution. This situation can only be avoided by starting the calculation from the saddle point itself. Therefore, the calculation is carried out in two steps. First, starting the integration from $T = T_1$ and $u = u_2$, two functions $Q_m(T)$ and $Q_m(u)$ are calculated by iterating to obtain the necessary inner boundary conditions. Then, $u(\xi)$ and $T(\xi)$ are calculated subsequently, by starting from the subshock.

Equations (8-23) are transformed into the following new form for a piecewise α with two components: For $\xi > 0$,

$$y_1' = 1,$$

$$y_2' = \begin{cases} -1 + (\gamma - 1)u_c\left[y_1^2/y_1\delta - 1\right] R_L/y_2, & y_1 < y_{1c}, \\ -1 + (\gamma - 1)u_c\left(y_1\delta^{/2}\, y_{10}^{-2}\, y_1^{-1/2} - 1\right) R_L/y_2, & y_1 > y_{1c}, \end{cases} \qquad \text{(D-5)}$$

where

$$y_1 = T,$$

$$y_2 = Q_m = dT/d\xi,$$

with the initial conditions

$$y_1(0) = y_{10} = T_1, \qquad y_1'(0) = 1,$$

$$y_2(0) = Q_{m1}, \qquad y_2'(0) = (dQ_m/dT)\,|_1,$$

where $y_2'(0)$ is given by Equation (8-24*b*), and y_{1c} corresponds to T_c. For $\xi < 0$,

$$y_1' = 1,$$

$$y_2' = \begin{cases} -\gamma\eta_0 + (\gamma+1)y_1 + f\left[\dfrac{y_1(\eta_0 - y_1)^2}{y_{10}\delta(\eta_0 - y_{10})^2} - 1\right], & y_1 < y_{1c}, \\ -\gamma\eta_0 + (\gamma+1)y_1 + f\left\{\dfrac{T_c^2}{T_1^2}\left[\dfrac{y_{1c}(\eta_0 - y_{1c})}{y_1^3(\eta_0 - y_1)}\right]^{1/2} - 1\right\}, & y_1 > y_{1c}, \end{cases} \tag{D-6}$$

where

$$y_1 = u,$$

$$y_2 = Q_m = (\eta_0 - 2y_1)dy_1/d\xi,$$

$$f = (\gamma - 1)\, R_L\, u_c\, (\eta_0/y_1 - 2)/y_2,$$

with the initial conditions

$$y_1(0) = y_{10} = u_2, \qquad y_1'(0) = 1,$$

$$y_2(0) = Q_{m2}, \qquad y_2'(0) = (dQ_m/du)|_2.$$

Picking $T_d^{(0)} > T_1$ as the starting point, the iteration runs as follows: First, integrate Equations (D-5) from T_1 to $T_d^{(0)}$ to get $R_{cu}^{(1)}$, the first estimate of R_{cu}. Next, integrate Equations (D-6) from u_2 to $u_d^{(0)}$, where $u_d^{(0)}$ is calculated from the equation of state $T_d = u_d(\eta_0 - u_d)$ to get $Q_{md}^{(1)}$, the first estimate of Q_{md}. Then $u_d^{(1)}$, the first estimate of $u_d = 1/X$, can be obtained by substituting $R_{cu}^{(1)}$ and $Q_{md}^{(1)}$ into Equation (8-24*c*) and solving it. Finally, $T_d^{(1)}$ can be solved from this equation. Accordingly $T_d^{(2)} \ldots T_d^{(n)}$ are calculated by iterations until $|T_d^{(n)} - T_d^{(n+1)}| < \varepsilon$ or $n > N$, where ε and N are the predetermined error and iteration time, respectively.

References

Aly, J. J.: 1984, *Astrophys. J.*, **283**, 349.

Aly, J. J.: 1985, *Astron. Astrophys.*, **143**, 19.

Aly, J. J.: 1990, *Computer Phys. Comm.*, **59**, 13.

Aly, J. J.: 1984, *Astrophys. J.*, **375**, L61.

Amari, T. and Aly, J. J.: 1989, *Astron. Astrophys.*, **208**, 261.

Anzer, U.: 1978, *Sol. Phys.*, **57**, 111.

Anzer, U. and Ballester, J. J.: 1990, *Astron. Astrophys.*, **238**, 365.

Athay, R. G.: 1976, *The Solar Chromosphere and Corona: Quiet Sun*, D. Reidel, Dordrecht, Holland.

Bel, N. and Laury-Micoulaut, C.: 1973, *J. Plasma Phys.*, **10**, 301.

Bender, C. M. and Orszag, S. A.: 1978, *Advanced Mathematical Methods for Scientists and Engineers*, Ch. 9, McGraw-Hill Book Co., New York.

Bhattacharjee, A. and Wang, X.: 1991, *Astrophys. J.*, **372**, 321.

Birn, J. and Schindler, K.: 1981, in E. R. Priest (ed.), *Solar Flare MHD*, Gordon and Breach, New York, p. 337.

Biskamp, D. and Welter, H.: 1989, *Sol. Phys.*, **120**, 49.

Browning, P. K. and Priest, E. R.: 1986, *Sol. Phys.*, **106**, 335.

Canfield, R. D., et al.: 1980, in P. A. Sturrock (ed.), *Solar Flares*, Colorado Assoc. Univ. Press, Boulder, p. 451.

Cargill P. J. and Priest, E. R.: 1982, *Solar Phys.*, **76**, 357.

Chevalier, R. A.: 1974, *Astrophys. J.*, **188**, 501.

Chevalier, R. A. and Theys, J. C.: 1975, *Astrophys. J.*, **195**, 53.

Coroniti, F. V.: 1970, *J. Plasma Phys.*, **4**, 265.

Cox, D. P.: 1972a, *Astrophys. J.*, **178**, 143.

Cox, D. P.: 1972b, *Astrophys. J.*, **178**, 159.

Cox, D. P. and Tucker, W. H.: 1969, *Astrophys. J.*, **157**, 1157.

Démoulin, P. and Priest, E. R.: 1988, *Astron. Astrophys.*, **206**, 336.

Dodson-Prince, H. W. and Hedeman, E. R.: 1970, *Sol. Phys.*, **13**, 401.

Edmiston, J. P. and Kennel, C. F.: 1986, *J. Geophys. Res.*, **91**, 1361.

Feldman, W. C., Schwartz, S. J., Bame, S. J., *et al.*: 1984, *Geophys. Res. Lett.*, **11**, 599.

Feldman, W. C., *et al.*: 1985, *J. Geophys. Res.*, **90**. 233.

Feldman, W. C., Tokar, R. L., Birn, J., Hones, E. W., Jr., Bame, S. J. and Russell, C. T.: 1987, *J. Geophys. Res.*, **92**, 531.

Ferraro, V. C. A. and Plumpton, C.: 1966, *An Introduction to Magneto-Fluid Dynamics*, Clarendon, Oxford.

Finn, J. M. and Chen, J.: 1990, *Astrophys. J.*, **349**, 345.

Forbes, T. G.: 1986, *Astrophys. J.*, **305**, 553.

Forbes, T. G.: 1988, *Sol. Phys.*, **117**, 97.

Forbes, T. G.: 1990, *J. Geophys. Res.*, **95**, 11919.

Forbes, T. G.: 1991, *Geophys. Astrophys. Fluid Dynamics*, **62**, 15.

Forbes, T. G. and Malherbe, J. M.: 1986a, *Astrophys. J.*, **302**, L67.

Forbes, T. G. and Malherbe, J. M.: 1986b, in D. F. Neidig(ed.), *The Lower Atmosphere of Solar Flares* , National Solar Observatories, Sacramento Peak, NM, NSO, p. 443.

Forbes, T. G. and Malherbe, J. M.: 1991, *Sol. Phys.*, **135**, 361.

Forbes, T. G., Malherbe, J. M. and Priest, E. R.: 1989, *Solar Phys.*, **120**, 258.

Forbes, T. G. and Priest, E. R.: 1983, *Sol. Phys.*, **88**, 211.

Forbes, T. G. and Priest, E. R.: 1987, *Rev. Geophys.*, **25**, 1583.

Forbes, T. G. and Isenberg, P. A.: 1991, *Astrophys. J.*, **373**, 294.

Foukal, P.: 1990, *Solar Astrophysics*, John Wiley & Sons, Inc., New York.

Giovanelli, R. G.: 1947, *Mon. Notices Roy. Astron. Soc.*, **107**, 338.

Gold, T.: 1964, in W. N. Hess (ed.), *Physics of Solar Flares*, NASA SP-50, Washington, DC, p.389.

Gosling, J. T., Hildner, E., Macqueen, R. M., Munro, R. H., Poland, A. I. and Ross, C. L.: 1974, *J. Geophys. Res.*, **79**, 4581.

Hada, T. and Kennel, C. F.: 1985, *J. Geophys. Res.*, **90**, 531.

Heinzel, P. and Karlick'y, M.: 1987, *Solar Phys.*, **110**, 343.

Heyvaerts, J. and Priest, E. R.: 1976, *Sol. Phys.*, **47**, 223.

Hirayama, T.: 1974, *Solar Phys.*, **34**, 323.

Hones, E. W., Jr.: 1979, *Space Sci. Rev.*, **23**, 393.

Hood, A. W. and Priest, E. R.: 1979, *Sol. Phys.*, **64**, 303.

Hood, A. W. and Priest, E. R.: 1980, *Sol. Phys.*, **66**, 113.

Hundhausen, A. J.: 1988, in V. J. Pizzo, T. E. Holzer and D. G. Sime (eds.), *Tech. Note 306 +Proc.*, Proceedings of the Sixth International Solar Wind Conference, Natl. Cent. For Atmos. Res., Boulder, Colo., p. 181.

Isenberg, P. A., Forbes, T. G., and Démoulin, P.: 1992, *Astrophys. J.*, submitted.

Jackers, K.: 1978, *Sol. Phys.*, **56**, 37.

Kaastra, J. J.: 1985, Ph.D. thesis, Rijksuniv., Utrecht, The Netherlands.

Kahler, S.: 1987, *Rev. Geophys.*, **25**, 663.

Kantrowitz, A. R. and Petschek, H. E.: 1966, in W. B. Kunkel(ed.), *Plasma Physics in Theory and Application* , MaGraw-Hill, New York, p. 147.

Kennel, C. F.: 1987, *J. Geophys. Res.*, **92**, 13427.

Kennel, C. F.: 1988, *J. Geophys. Res.*, **93**, 8545.

Kleczek, J.: 1964, in W. H. Hess(ed.), *AAS-NASA Symposium on the Physics of Solar Flares* , NASA SP-50, p. 77.

Klimchuk, J. A.: 1990, *Astrophys. J.*, **354**, 745.

Klimchuk, J. A. and Sturrock, P. A.: 1989, *Astrophys. J.*, **345**, 1034.

Klimchuk, J. A. and Sturrock, P. A.: 1992, *Astrophys. J.*, in press.

Kopp, R. A. and Pneuman, G. W.: 1976, *Solar phys.*, **50**, 85.

Krall, N. A. and Trivelpiece, A. W.: 1973, *Principles of Plasma Physics*, MaGraw-Hill, New York.

Kundu, M. R., Woodgate, B. and Schmahl, E. J.: 1989, *Energetic Phenomena on the Sun*, Kluwer Academic Publ., Dordrecht, The Netherlands.

Lin, H. -A., Lin R. P. and Kane S. R.: 1985, *Solar Phys.*, **99**, 263.

Linker, J. A., Van Hoven, G. and Schnack, D. D.: 1990, *J. Geophys. Res.*, **95**, 4229.

Lisa, J. P., Klimchuk, J. A., and Sturrock, P. A.: 1992, *Astrophys. J.*, in press.

Low, B. C.: 1977, *Astrophys. J.*, **212**, 234.

Low, B. C.: 1981, *Astrophys. J.*, **251**, 352.

Low, B. C.: 1982, *Rev. Geophys. Space Phys.*, **20**, 145.

Low, B. C.: 1984, *Astrophys. J.*, **281**, 392.

Low, B. C.: 1986, *Astrophys. J.*, **307**, 205.

Low, B. C.: 1990, *Ann. Rev. Astron. Astrophys.*, **28**, 491.

Low, B. C. and Wolfson R.: 1988, *Astrophys. J.*, **324**, 574.

MacCombie, W. J. and Rust, D M: 1979, *Sol. Phys.*, **61**, 69.

Malherbe, J. M., Forbes, T. G. and Priest, E. R.: 1984, in *The Hydromagnetics of the Sun* (Paris: ESA) (ESA SP-220), p. 119.

Marshak R. E.: 1958, *Phys. Fluids*, **1**, 24.

Martens, P. C. H. and Kuin, N. P. M.: 1989, *Sol. Phys.*, **122**, 263.

Micik, Z., Barnes, D. C. and Schnack, D. D.: 1988, *Astrophys. J.*, **328**, 830.

Molodenskii, M. M. and Filippov, B. P.: 1987, *Soviet Astro.* (English Transl.), **31**, 564.

Moore, R. L.: 1988, *Astrophys. J.*, **324**, 1132.

Mouschovias, T. C. and Poland, A. I.: 1978, *Astrophys. J.*, **220**, 675.

Muskhelishvili, N. I.:1953 (English Transl.), *Singular Integral Equation*, Groningen, Holland.

Ohki, K.: 1975, *Solar Phys.*, **45**, 435.

Parker, E. N.: 1963, *Astrophys. J. Suppl.*, **8**, 177.

Parker, E. N.: 1984, in E. W. Hones, Jr. (ed.), *Magnetic Reconnection in Space and Laboratory Plasmas* , AGU, Washington, D. C., p. 32.

Peres, G., Rosner, R., Serio,S. and Vaiana, G. S.: 1982, *Astrophys. J.*, **252**, 791.

Petschek, H. E.: 1964, in W. H. Hess(ed.), *AAS-NASA Symposium on the Physics of Solar Flares* , NASA SP-50, p. 425.

Pneuman, G. W.: 1984., *Sol. Phys.*, **94**, 387.

Priest, E. R.: 1981, *Solar Flare MHD*, Gordon and Breach, London.

Priest, E. R.: 1982a, *Solar MHD*, D. Reidel Publ. Co., Dordrecht, Holland.

Priest, E. R.: 1982b, *Solar Phys.*, **86**, 33.

Priest, E. R.: 1984, in E. W. Hones, Jr. (ed.), *Magnetic Reconnection in Space and Laboratory Plasmas* , AGU, Washington, D. C., p. 63.

Priest, E. R.: 1985a, *Rep. Prog. Phys.*, **48**, 955.

Priest, E. R.: 1985b, paper presented at Meeting on SOHO and Cluster Missions, Eur. Space Agency, Garmish, Germany.

Priest, E. R.: 1986, in P. Gondhaleker (ed.), *Proc. RAL Workshop on Solar and Stellar Flares*, p. 140.

Priest, E. R. and Forbes T. G.: 1986, *J. Geophys. Res.*, **91**, 5579.

Priest, E. R. and Forbes, T. G.: 1990, *Sol. Phys.*, **126**, 319.

Richter, A. K.: 1988, in V. J. Pizzo, T. E. Holzer and D. G. Sime(eds.), *Proceedings of the Sixth International Solar Wind Conference*, p. 411.

Roberts, P. H.: 1967, *An Introduction to Magnetohydrodynamics*, Elsevier Pub. Co, New York.

Robertson, J. A. and Priest, E. R.: 1987, *Sol. Phys.*, **114**, 311.

Rosenau, P. and Frankenthal, S.: 1978, *Phys. Fluids*, **21**(4), April, 559.

Schmieder, B., Forbes, T. G., Malherbe, J. M. and Machado, M. E.: 1987, *Astrophys. J.*, **317**, 956.

Shibata, K., Tajima, T., Steinolfson, R. S. and Matsumoto, R.: 1989, *Astrophys. J.*, **345**, 584.

Simnett, G. M. and Harrison, R. A.: 1985, *Sol. Phys.*, **99**, 291.

Sonnerup, B. U. Ö.: 1979, in L. Lanazerotti, C. Kennel and E. N. Parker(eds.), *Solar System Plasma Physics*, Vol. III, chap.3, sect. 1, 2, North Holland, Amsterdam.

Sonnerup, B. U. Ö.: 1984, in D. M. Butler and K. Papadopoulos(eds.), *Solar Terrestrial Physics: Present and Future* , ch. 1, NASA Ref. Publ., RP-1120.

Steele, C. P. C. and Priest, E. R.: 1989, *Sol. Phys.*, **119**, 157.

Steele, C. P. C. and Priest, E. R.: 1990, *Sol. Phys.*, **125**, 295.

Steinolfson, R. S.: 1988, *J. Geophys. Res.*, **93**, 14,269.

Steinolfson, R. S.: 1989, in J. H. Waite, J. L. Burch and R. L. Moore (eds.), *Solar System Plasma Physics, Geophys. Monogr. Ser.*, vol. 54, AGU, Washington, D. C., p. 269.

Steinolfson, R. S. and Hundhausen, A. J.: 1989, *J. Geophys. Res.*, **94**, 1222.

Steinolfson, R. S., Wu, S T., Dryer, M. and Tandberg-Hanssen, E.: 1978, *Astrophys. J.*, **225**, 259.

Stix, M.: 1989, *The Sun*, Springer-Verlag Berlin Heidelberg.

Sturrock, P. A.: 1972, in R. Ramaty and R. G. Stone(eds.), *High Energy Phenomena on the Sun* , NASA, p. 3.

Sturrock, P. A.: 1980, *Solar Flares*, Colorado Assoc. Univ. Press, Boulder, Colorado.

Sturrock, P. A.: 1987, *Sol. Phys.*, **113**, 13.

Sturrock, P. A.: 1989, *Sol. Phys.*, **121**, 387.

Švestka, Z.: 1986, in D. F. Neidig (ed.), *The Lower Atmosphere of Solar flares*, Sacramento Peak Observatory, New Mexico, p. 332.

Sweet, P. A.: 1958, in B. Lehnert(ed.), *Electromagnetic Phenomena in Cosmical Physics* , Cambridge University Press, London, p. 123.

Swift, D. W.: 1983, *J. Geophys. Res.*, **88**, 5685.

Tanaka, K.: 1983, in P. B. Byrne and M. Rodono (eds.), *Proc. IAU Colloquium 71*, Reidel, Dordrecht, p. 307.

Tandberg-Hanssen, E. and Emslie, A. G.: 1988, *The physics of solar flares*, Cambridge Univ. Press, Cambridge.

Tousey, R.: 1973, in M. J. Rycroft and S. K. Runcorn (eds.), *Space Research XIII*, Akademie, Birlin, p. 713.

van Ballegooijen, A. A. and Martens, P. C. H.: 1989, *Astrophys. J.*, **343**, 971.

Van Hoven, G.: 1981, in E. R. Priest (ed.), *Solar Flare MHD*, Gordon and Breach, New York, p. 217.

Van Tend, W.: 1979, *Sol. Phys.*, **61**, 89.

Van Tend, W. and Kuperus, M.: 1978, *Sol. Phys.*, **59**, 115.

Wagner, W. J.: 1982, *Adv. Space Res.*, **2**, 203.

Wagner, W. J., Hildner, E., House, L. L., Sawyer, C., Sheridan, K. V. and Dulk, G. A.: 1981, *Astrophys. J.*, **244**, L123.

Webb, D. F., et al.: 1980, in P. A. Sturrock (ed.), Solar Flares, Colorado Assoc. Univ. Press, Boulder, p. 471.

Whitham, G. B.: 1974, *Linear and Nonlinear Waves*, Wiley & Sons, New York, p. 96.

Winske, D., Storer, E. K. and Gray, S. P.: 1985, *Geophys. Res. Lett.* **12**, 295.

Withbroe, G. L.: 1978, *Astrophys. J.*, **225**, 641.

Wolfson, R.: 1982, *Astrophys. J.*, **255**, 774.

Wolfson, R. and Low, B. C.: 1992, *Astrophys. J.*, submitted.

Wolfson, R. and Gould, S. A.: 1985, *Astrophys. J.*, **296**, 287.

Wu, S. T. and Wang, J. F.: 1987, *Comput. Methods Appl. Mech. Eng.*, **64**, 267.

Yang, W. H., Sturrock, P. A., and Antiochos, S. K.: 1986, *Astrophys. J.*, **309**, 383.

Yeh, T.: 1982, *Sol. Phys.*, **78**, 287.

Yeh, T.: 1985, *Sol. Phys.*, **95**, 83.

Yeh, T. and Axford, A. I.: 1970, *J. Plasma Phys.*, **4**, 207.

Yeh, T. and Dryer, M.: 1981, *Astrophys. J.*, **245**, 704.

Zirin, H.: 1986, in D. F. Neidig(ed.), *The Lower Atmosphere of Solar Flares* , National Solar Observatories, Sacramento Peak, NM, p. 78.

Zirin, H.: 1988, *Astrophysics of the Sun*, Cambridge Univ. Press, Cambridge.

Zwingmann, W.: 1985, Ph.D. Thesis, Bochum University.

Zwingmann, W.: 1987, *Sol. Phys.*, **111**, 309.